Spring 5-15-2020

# Phantoms to Placentas: MR Methods for Oxygen Quantification

Kelsey Meinerz
*Washington University in St. Louis*

## Recommended Citation

Meinerz, Kelsey, "Phantoms to Placentas: MR Methods for Oxygen Quantification" (2020). *Arts & Sciences Electronic Theses and Dissertations*. 2221.
https://openscholarship.wustl.edu/art_sci_etds/2221

WASHINGTON UNIVERSITY IN ST. LOUIS

Department of Physics

Dissertation Examination Committee:
Anders E Carlsson, Chair
Joseph JH Ackerman, Co-Chair
Joel R Garbow, Co-Chair
Shankar Mukherji
Jeffrey J Neil
Ryan C Ogliore

# Phantoms to Placentas: MR Methods for Oxygen Quantification

by
Kelsey Viola Meinerz

A dissertation presented to
The Graduate School
of Washington University in
partial fulfillment of the
requirements for the degree
of Doctor of Philosophy

May 2020
St. Louis, Missouri

# Table of Contents

# List of Figures

# List of Tables

# Acknowledgments

If you had asked me at the beginning of grad school what the next few years of my life would be like, I probably would have said that I knew it wasn't going to be easy. We all know, going into it, that pursuing a graduate degree is a real challenge; but that level of difficulty is something you only fully appreciate once you experience it for yourself. If you had also asked me what my life outside of graduate school over those few years would look like, I definitely would have predicted a different outcome than what came to pass. Life has a way of throwing you curveballs or surprises which can sometimes be very challenging to manage. I'm very grateful for the love and support that I've received from my family and friends, both new and old; without that, I never could have made it this far. My parents have supported me in innumerable ways, for which I will never be able to satisfactorily thank them. My siblings and all their wonderful significant others have been the greatest cheerleaders I could have ever asked for while I've strived to achieve my final, nerdy form. My friends have been there to listen when I needed to vent and always managed to make me laugh when I didn't realize how badly I needed a giggle. And on top of all that I need to recognize my dog, Ginger, who, despite being an absolutely terrible troublemaker at times, gave me a warm welcome home every day and has been my little shadow and sidekick through good times and bad.

Kelsey Meinerz

*Washington University in St. Louis*

*May 2020*

# ABSTRACT OF THE DISSERTATION

Phantoms to Placentas: MR Methods for Oxygen Quantification

by

Kelsey Viola Meinerz

Doctor of Philosophy in Physics

Washington University in St. Louis, 2020

Professor Anders E Carlsson, Chair

Professor Joseph JH Ackerman, Co-Chair

Professor Joel R Garbow, Co-Chair

Molecular oxygen ($O_2$) is vital for efficient energy production and improper oxygenation is a hallmark of disease or metabolic dysfunction. In many pathologies, knowledge of tissue oxygen levels ($pO_2$) could aid in diagnosis and treatment planning. The gold standard for $pO_2$ measures in tissue are implantable probes, which are invasive, require surgery for placement, and are inaccessible to certain regions of the body. Methods for determining $pO_2$ both non-invasively and quantitatively are lacking.

The slight paramagnetic nature of $O_2$ provides opportunities to non-invasively characterize $pO_2$ in tissue via magnetic resonance (MR) techniques. As such, $O_2$ can be treated as a weak endogenous contrast agent for longitudinal relaxation and, therefore, the measured longitudinal relaxation rate constant ($R_1$) is directly proportional to $pO_2$. Precise characterization of $R_1$ in the absence of oxygen ($R_{1,0}$) and the relaxivity of $O_2$ ($r_1$) would allow for an $R_1$-based $pO_2$ measurement.

Additionally, the effective transverse relaxation rate constant ($R_2$*) in tissue is strongly affected by the magnetic susceptibility effects of deoxyhemoglobin within the vasculature. Many forms of placental dysfunction, e.g., pre-eclampsia and intrauterine growth restriction, are proposed to be caused by altered vasculature development within the placenta, potentially leading to adverse outcomes for both mother and fetus. Improved biomarkers of placental function would aide in optimal timing for early delivery once the placenta can no longer support fetal development.

The objectives of this dissertation were to: 1) investigate the efficacy of an $R_1$-based method of $pO_2$ quantification in a tissue surrogate; and 2) apply MR methods of monitoring $pO_2$ in tissue and $O_2$ within the vasculature in mouse models of disease and insufficiency to assess placental development and function. For the first goal, Bayesian probability theory-based model selection was used to evaluate potential models of longitudinal relaxation in *in vivo* tissue and an *in vitro* tissue surrogate, crosslinked bovine serum albumin (xBSA). xBSA was then used to investigate physiologic confounds to an $R_1$-based method of $pO_2$ quantification, including temperature, pH, and protein concentration, and $R_{1,0}$ and $r_1$ were determined. For the second goal, mouse models of both placental insufficiency and Zika virus infection during pregnancy were monitored in late gestation for changes in volume, $R_1$, and $R_2$* at baseline and with a gas challenge to assess the placental response to an altered environment.

It was found that 1) both *in vivo* and xBSA relaxation data are best fit with a biexponential model and, therefore, xBSA is a good surrogate for tissue, in terms of longitudinal relaxation; 2) physiologic confounds to an $R_1$-based method of $pO_2$ quantification exert considerable affects upon measured $R_1$ and must, therefore, be precisely controlled or accounted for; 3) placental volume, $R_2^*$, and change in $R_2^*$ due to a breathing gas challenge hold promise as biomarkers of placental development and dysfunction.

These findings suggest that an $R_1$-based method for $pO_2$ quantification *in vivo* is likely not feasible on a routine basis due to the small water relaxivity of $pO_2$ and confounds to the analysis due to relaxation effects of tissue pH, temperature, and protein concentration, but MR methods could provide much needed information regarding placental function in high risk pregnancies and warrants further investigation.

# Chapter 1: Introduction

## 1.1 Motivation:

Improper oxygenation is a hallmark of many diseases or dysfunctions and knowledge of molecular oxygen ($O_2$) levels within the body ($pO_2$) could aid in diagnosis and treatment planning. Tumors characterized by hypoxia are known to have increased angiogenesis and propensity for metastasis[1], as well as increased resistance to chemotherapy[2] and radiation therapy[3] treatments. Hypoxia in adipose tissue has been proposed to drive insulin resistance, leading to type II diabetes[4]. Exchange of respiratory gases is a major role of the placenta, with insufficient exchange of $O_2$ potentially inducing long-term adverse effects for both mother and fetus[5, 6].

Implantable probes are considered the gold standard for measuring tissue $pO_2$[7] but are invasive in nature, requiring surgery for placement. Methods of determining tissue $pO_2$ non-invasively and quantitatively are lacking. Optical imaging techniques are sensitive to levels of oxy- and deoxyhemoglobin[8], which can be modeled to yield information about oxygen saturation[9-11] and metabolic rate of oxygen consumption[12]. While non-invasive, these techniques are limited to a depth of penetration on the order of a few millimeters to a centimeter. Positron emission tomography (PET) can detect even low levels of hypoxic tumor cells[13] but is limited by spatial resolution of a millimeter or more and requires exposure to radioactive materials. Magnetic resonance (MR) techniques can non-invasively probe the entirety of the body with sub-millimeter spatial resolution. Blood-oxygen-level dependent (BOLD) MR imaging (MRI) utilizes the magnetic susceptibility differences in the vasculature due to oxy- and deoxyhemoglobin levels[14]. However, quantitative BOLD experiments are quite challenging[15] and therefore results are often expressed as relative changes with respect to baseline measurements. $O_2$ is slightly paramagnetic and can therefore be regarded as a weak, endogenous longitudinal relaxation rate constant ($R_1$) contrast agent for MR. Therefore, measured $R_1$ is in principle directly proportional to tissue $pO_2$.

The goal of this dissertation is twofold: 1) investigate efficacy of $R_1$-based $pO_2$ quantification and 2) use MRI with a breathing gas challenge to investigate non-invasive biomarkers of placental development and function in mouse models of insufficiency or disease.

## 1.2 State of Research:

### 1.2.1 Basics of Nuclear Magnetic Resonance

Classically, a rotating object possesses the property of angular momentum which can be visualized as a vector pointing along the axis of rotation. The quantum mechanical counterpart to this property is quantized and inherent to elementary particles, *i.e.* protons, neutrons, electrons, as well as composite particles and whole nuclei. Nuclear spin angular momentum describes the spin state of the superposition of protons and neutrons within the atomic nucleus, which can be described by a magnitude $L$ of the form:

$$L = \frac{h}{2\pi}[I(I+1)]^{1/2}$$

where *h* is Planck's constant and *I* is the nuclear spin quantum number, which takes the form N/2, with N any non-negative integer. Nuclei with spin *I* are (2*I*+1)-fold degenerate, with sublevels described by the quantity *m* which is of the form:

$$m = -I, I+1, \dots, 0, \dots, I-1, I$$

The projection of this angular momentum upon an arbitrary axis (choose z-axis) is then given by $m\, h/2\pi$. If a magnetic field **B** is applied, this degeneracy is broken due to nuclear Zeeman splitting. The most common nuclide for nuclear magnetic resonance (NMR) is $_{1}$H which has a nuclear spin quantum number of 1/2 and subsequently two levels: m = +1/2 or -1/2. In the case where **B** is aligned with the z-axis, the energy gap resulting from this Zeeman splitting is

$$\Delta E = \frac{\gamma h B}{2\pi}$$

where $\gamma$ is the gyromagnetic ratio, which is 42.58 MHz/T for $_{1}$H. Most nuclei have a positive gyromagnetic ratio ($\gamma > 0$) while electrons and a few nuclei (e.g., $_{15}$N) have a negative gyromagnetic ratio ($\gamma < 0$). A depiction of this splitting is shown in figure 1.1 for both $_{1}$H and $_{15}$N, which are both spin 1/2 nuclei, though the gyromagnetic ratio of $_{1}$H is ~10x greater than that of $_{15}$N.

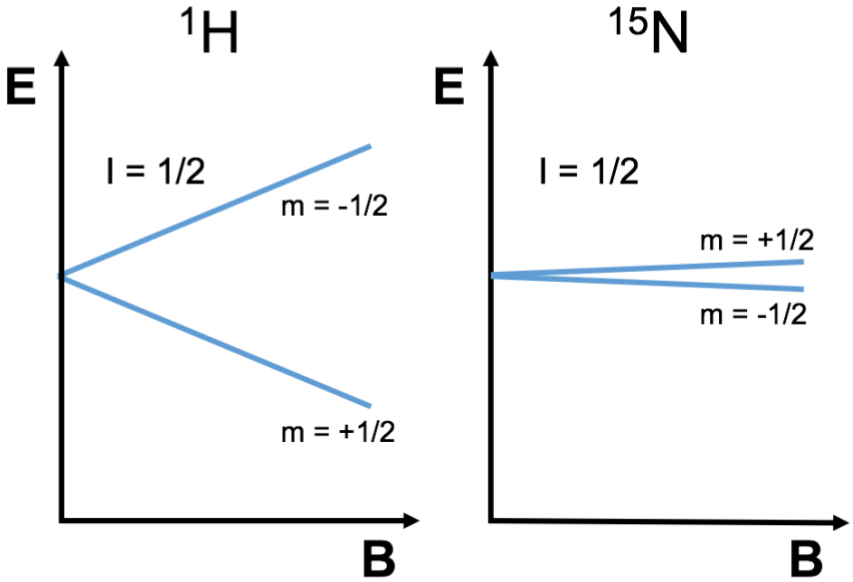

**Figure 1.1.** Zeeman splitting for two example nuclei. The gyromagnetic ratio of $_1$H is ~10x greater than that of $_{15}$N, resulting is ~10x splitting in energy for the same magnetic field strength.

For a system at thermal equilibrium with $\gamma > 0$, the relative populations for the high and low energy conformations can be described by the ratio

$$\frac{N_{aligned}}{N_{anti-aligned}} = e^{\Delta E / kT}$$

where $N_{\text{aligned}}$ and $N_{\text{anti-aligned}}$ refer to the populations of spins in each state, *k* is the Boltzmann constant, and T is the absolute temperature. There are more spins in the lower energy state (aligned) than in the higher energy state (anti-aligned) and this population difference results in a net magnetization that is parallel to the applied magnetic field. This is the source of MR signal and is extremely small (on the order of ppm) at biologically relevant temperatures and currently accessible magnetic field strengths.

The resonance energy can also be expressed as a function of frequency of precession

$$E = 2\pi h\omega_0$$

where $\omega_0$ is the Larmor frequency, which is then proportional to the magnetic field by the relationship $\omega_0$ =- $\gamma B_0$. If a radiofrequency (RF) pulse is applied at the Larmor frequency for an appropriate length of time, oriented perpendicular to the applied magnetic field ($B_0$), the net magnetization will nutate into the transverse plane, as shown in figure 1.2 A. Once the RF pulse is turned off, the ensemble of spins representing the net magnetization will then precess in the transverse plane. However, microscopic fluctuations in the local magnetic fields will result in the ensemble of precessing spins gradually losing their phase coherence such that the net transverse magnetization will decay. If a detector or receiver coil is placed in the transverse plane, the precessing magnetization will induce a voltage in this coil of the form shown in figure 1.2 B. This time-domain oscillating voltage signal, known as the free induction decay (FID), is then digitized and Fourier transformed to obtain the MR signal.

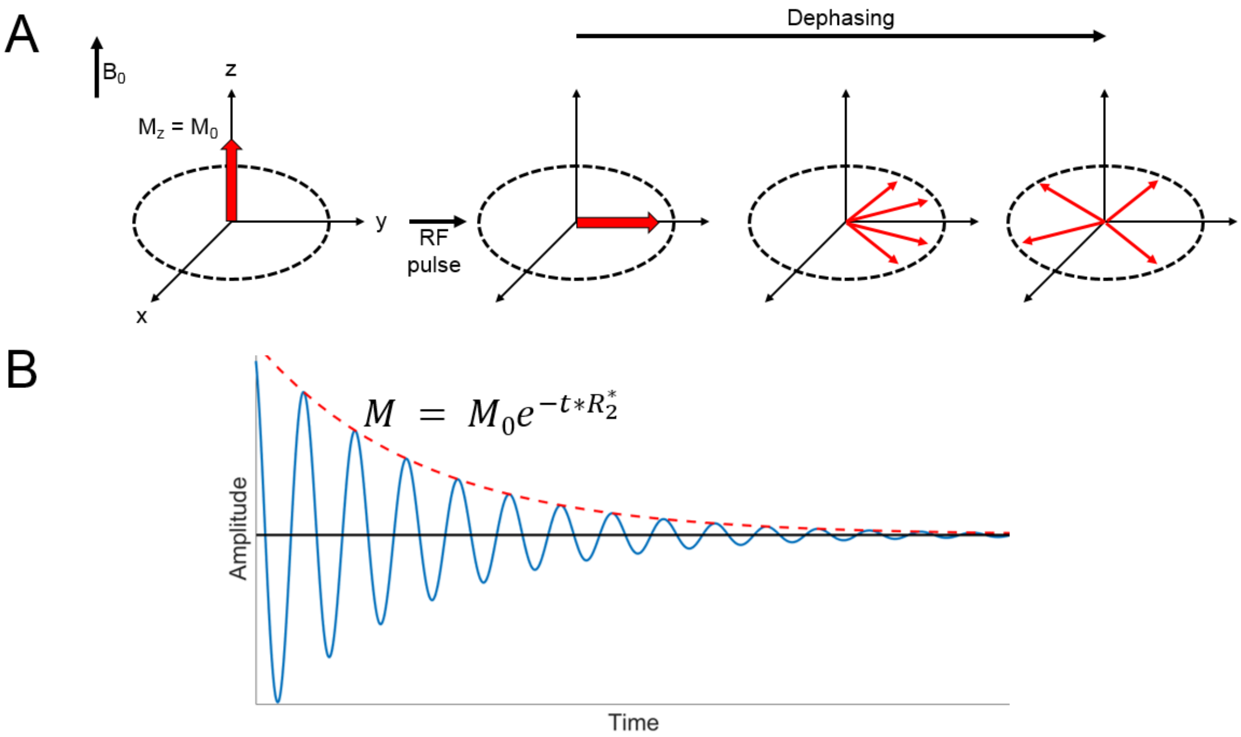

**Figure 1.2.** Illustration of free induction decay. Effective transverse relaxation can be characterized by **A)** nutating the equilibrium net magnetization into the xy-plane wherein the spins precess about the applied magnetic field ($B_0$) and dephase. Placement of a receiver coil in the xy-plane generates an MR signal of the form in **B)** which is characterized by the effective transverse relaxation rate constant, $R_2$*.

The signal decay of the FID can be characterized by the effective transverse relaxation rate constant ($R_2$*) which is the superposition of two mechanisms, homogeneous and inhomogeneous broadening. Homogeneous broadening is due to high frequency microscopic fluctuations within the magnetic field and is characterized by the transverse relaxation rate constant ($R_2$), whereas inhomogeneous broadening is due to low frequency macroscopic variations in the magnetic field due to magnetic susceptibility effects or inhomogeneity in the static magnetic field.

Longitudinal relaxation describes the process by which the perturbed net magnetization will return to thermal equilibrium via stochastic spin flips (-1/2 ↔ +1/2) due to thermal-energy-driven molecular motion. The applied magnetic field, $B_0$, biases these otherwise random fluctuations so that over time the net magnetization returns to the equilibrium condition where it is aligned with the applied field. To visualize this relaxation process, we can iteratively invert the net magnetization with an RF pulse, wait some delay period t, and then rotate the net magnetization into the transverse plane with another RF pulse to generate an MR signal. Before the next iteration, an additional delay follows signal collection to allow the sample to return to thermal equilibrium. This iterative process is known as the Inversion Recovery (IR) experiment and is shown in figure 1.3 A. Plotting the collected MR signal amplitude against the delay time between RF pulses yields a recovery curve, shown in figure 1.3 B, which is characterized by the longitudinal relaxation rate constant ($R_1$).

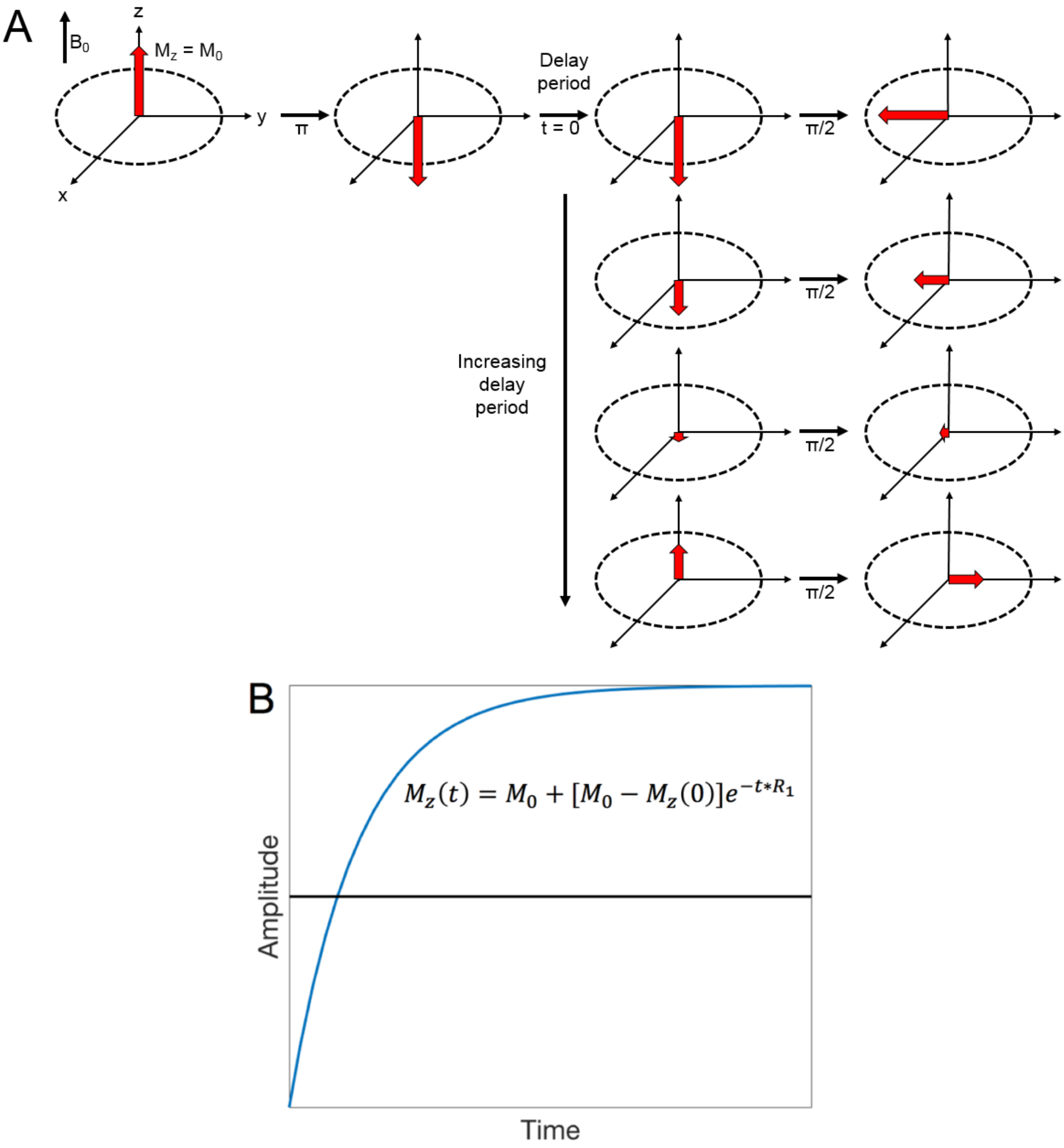

**Figure 1.3.** Illustration of longitudinal relaxation. Longitudinal relaxation can be characterized by **A)** perturbing the equilibrium net magnetization and measuring the amplitude of the net magnetization after a delay period (t). The inversion recovery experiment, shown here, is one method for characterizing longitudinal relaxation, which generates an MR signal of the form shown in **B)** which is characterized by the longitudinal relaxation rate constant, $R_1$.

### 1.2.2 Oxygen MR Effects

The measured $R_1$ of a sample can be affected by contrast agents, both endogenous and exogenous. Exogenous MR contrasts are usually gadolinium-based complexes in which the strongly paramagnetic gadolinium atom, with its 7 unpaired electrons, interacts with nearby water molecules via dipole-dipole interactions, enhancing the longitudinal relaxation (increased $R_1$) of the protons. Similarly, $O_2$ is an endogenous contrast agent, though a much weaker agent due to its being only slightly paramagnetic. A heavily exaggerated illustration of the relaxation enhancement effect due to the presence of $O_2$ upon longitudinal relaxation is shown in figure 1.4. This relaxation enhancement effect upon the measured $R_1$ can then be expressed with the following relationship

$$R_1=R_{1,0}+r_1*pO_2$$

in which $R_{1,0}$ is the longitudinal relaxation rate constant in the absence of $O_2$, $r_1$ is the longitudinal relaxivity of $O_2$, and $pO_2$ is the partial pressure of oxygen. The relaxivity of any contrast agent is a complex factor, dependent upon dipolar and scalar interactions (which, in turn, are magnetic field strength dependent) and correlation times (dependent upon motion factors, e.g., rotation and exchange rates)[16, 17]. Precise determination of $R_{1,0}$ and $r_1$ would enable $pO_2$ to be directly quantified from $R_1$ measurements.

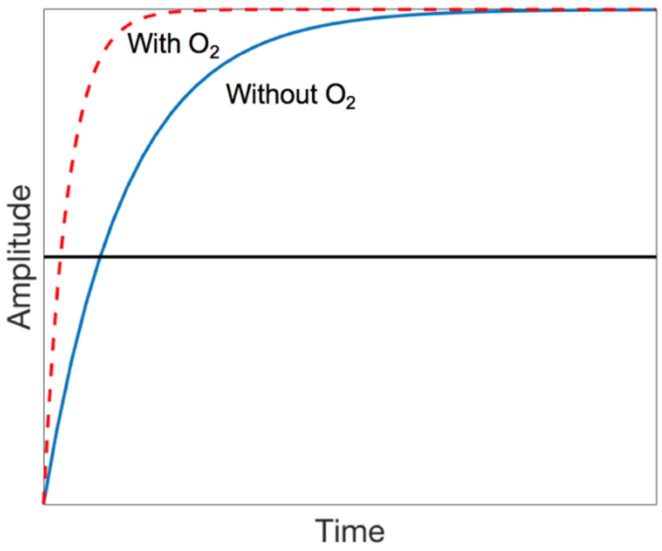

**Figure 1.4.** Illustration of $_1$H longitudinal relaxation of water without oxygen (solid blue) and with oxygen (dashed red). The relaxation enhancement due to $O_2$ is heavily exaggerated in this example.

Even without precise knowledge of these constants *in vivo*, $R_1$-based methods can be used in conjunction with inhaled breathing gases having variable $O_2$ content to drive tissue $pO_2$ changes[18, 19]. Variations in measured $R_1$ are then interpreted as changes in tissue $pO_2$.

As stated previously, BOLD MRI derives contrast from changing concentrations of oxy- and deoxyhemoglobin within the vasculature[14, 20]. Oxyhemoglobin has no unpaired electrons and is weakly diamagnetic whereas deoxyhemoglobin has 4 unpaired electrons and is paramagnetic[21]. The presence of deoxyhemoglobin therefore induces local magnetic field distortions, creating magnetic susceptibility differences between the vasculature and the surrounding tissue. These local field distortions induce more rapid dephasing of spins in the transverse plane, thereby increasing $R_2$* (and also $R_2$) in the surrounding region. BOLD MRI, therefore, is another method for mapping variations of *in* *vivo* oxygenation, with changes in $R_2$* directly proportional to changes in deoxyhemoglobin.

### 1.2.3 Placenta

The placenta, despite playing an extremely vital role in maintaining the health of both mother[22, 23] and fetus[24-26], remains a poorly characterized organ. This is, in part, due to the temporary nature of the placenta and ethical barriers to studying pregnant women. Murine placenta is a good model for the human placenta, with an analogous layered structure and method for exchange of constituents between maternal and fetal blood supplies[27, 28].

The placenta is responsible for maintaining fetal homeostasis through functions such as facilitating exchange of nutrients, respiratory gases, and wastes; creation and distribution of numerous hormones; and providing an immunological barrier between mother and fetus. Placental dysfunction can manifest in many forms including pre-eclampsia (PE)[29, 30], intrauterine growth restriction (IUGR)[31], and infection with TORCH pathogens[32] - which are characterized by the ability to cross and infect the placenta. In general, the best place for a developing fetus to be is *in utero*. However, in cases of placental dysfunction, wherein the most common form of treatment is early delivery, information regarding the level of placental function could help to determine optimal timing. MR methods could potentially provide non-invasive and reliable biomarkers of placental function towards this end.

## 1.3 Dissertation Overview

In this dissertation, Chapters 2 – 3 focus on quantitative longitudinal relaxation methods, using both preclinical *in vivo* and *in vitro* data to investigate the optimal signal model and probe physiologic confounds to an $R_1$-based tool for $pO_2$ quantification.

Chapter 2 focuses on the problem of proper signal model selection and the use of Bayesian probability theory-based methods to determine the optimal choice for quantitative measurements. Longitudinal relaxation measurements collected in both *in vivo* rat brain and *in vitro* crosslinked bovine serum albumin (xBSA) samples were used to determine the most probable model from a pool of five potential signal models.

Chapter 3 deals with physiologic confounds to an $R_1$-based $pO_2$ quantification method using xBSA as a tissue surrogate. Sample temperature, pH, and protein concentration were varied to determine their affects upon $R_1$ and the direct relationship between $pO_2$ and $R_1$ is quantified.

Chapters 4 – 5 then focus on investigating placental development and function in mouse models of insufficiency and infection with MRI. Placental volume, $R_1$, and $R_2$* were measured at two time points in late gestation to assess placental growth and function. Furthermore, a gas challenge was employed at each time point to assess the placental response to environmental changes.

Chapter 4 employs two established mouse models of common placental disorders in human pregnancy, PE and IUGR, to investigate how these disorders affect placental development and function in late gestation, with respect to healthy controls.

Chapter 5 investigates the effects of Zika virus (ZIKV) infection and hydroxychloroquine (HCQ) treatment upon murine placental development and function in late gestation. This work was performed in collaboration with Dr Indira U Mysorekar and Brooke Liang at Washington University in St Louis School of Medicine.

Finally, chapter 6 closes the dissertation with a summary of the specific accomplishments of these studies and a brief discussion of future studies which are beyond the scope of this work.

## 1.4 References

**[1]**. Hockel M, Vaupel P. Biological consequences of tumor hypoxia. *Semin Oncol.* 2001;28(2):36-41.10.1016/S0093-7754(01)90211-8.

**[2]**. Tan EY, Yan M, Campo L, et al. The key hypoxia regulated gene CAIX is upregulated in basal-like breast tumours and is associated with resistance to chemotherapy. *Brit J Cancer.* 2009;100(2):405-411.10.1038/sj.bjc.6604844.

**[3]**. Gray LH, Conger AD, Ebert M, Hornsey S, Scott OCA. The Concentration of Oxygen Dissolved in Tissues at the Time of Irradiation as a Factor in Radiotherapy. *Brit J Radiol.* 1953;26(312):638-648.Doi 10.1259/0007-1285-26-312-638.

**[4]**. Ye J. Emerging role of adipose tissue hypoxia in obesity and insulin resistance. *Int J Obesity.* 2009;33(1):54-66.10.1038/ijo.2008.229.

**[5]**. Burton GJ. Oxygen, the Janus gas; its effects on human placental development and function. *J Anat.* 2009;215(1):27-35.10.1111/j.1469-7580.2008.00978.x.

**[6]**. Goplerud JM, Delivoria-Papadopoulos M. Physiology of the placenta--gas exchange. *Ann Clin Lab Sci.* 1985;15(4):270-278

**[7]**. Kabon B, Rozum R, Marschalek C, et al. Supplemental postoperative oxygen and tissue oxygen tension in morbidly obese patients. *Obes Surg.* 2010;20(7):885-894.10.1007/s11695-010-0168-1.

**[8]**. Intes X, Chance B. Non-PET functional imaging techniques: optical. *Radiol Clin North Am.* 2005;43(1):221-234, xii.10.1016/j.rcl.2004.07.002.

**[9]**. Saito T, Yamaguchi H. Optical imaging of hemoglobin oxygen saturation using a small number of spectral images for endoscopic application. *J Biomed Opt.* 2015;20(12):126011.10.1117/1.JBO.20.12.126011.

**[10]**. Li Q, Lin J, Clancy NT, Elson DS. Estimation of tissue oxygen saturation from RGB images and sparse hyperspectral signals based on conditional generative adversarial network. *Int J Comput Assist Radiol Surg.* 2019;14(6):987-995.10.1007/s11548-019-01940-2.

**[11]**. Tzoumas S, Nunes A, Olefir I, et al. Eigenspectra optoacoustic tomography achieves quantitative blood oxygenation imaging deep in tissues. *Nat Commun.* 2016;7:12121.10.1038/ncomms12121.

**[12]**. Ghijsen M, Lentsch GR, Gioux S, et al. Quantitative real-time optical imaging of the tissue metabolic rate of oxygen consumption. *J Biomed Opt.* 2018;23(3):1-12.10.1117/1.JBO.23.3.036013.

**[13]**. Lopci E, Grassi I, Chiti A, et al. PET radiopharmaceuticals for imaging of tumor hypoxia: a review of the evidence. *Am J Nucl Med Mol Imaging.* 2014;4(4):365-384

**[14]**. Ogawa S, Lee TM, Nayak AS, Glynn P. Oxygenation-sensitive contrast in magnetic resonance image of rodent brain at high magnetic fields. *Magn Reson Med.* 1990;14(1):68-78.10.1002/mrm.1910140108.

**[15]**. He X, Yablonskiy DA. Quantitative BOLD: mapping of human cerebral deoxygenated blood volume and oxygen extraction fraction: default state. *Magn Reson Med.* 2007;57(1):115-126.10.1002/mrm.21108.

**[16]**. Lauffer RB. Paramagnetic Metal-Complexes as Water Proton Relaxation Agents for Nmr Imaging - Theory and Design. *Chemical Reviews.* 1987;87(5):901-927.DOI 10.1021/cr00081a003.

**[17]**. Rohrer M, Bauer H, Mintorovitch J, Requardt M, Weinmann HJ. Comparison of magnetic properties of MRI contrast media solutions at different magnetic field strengths. *Invest Radiol.* 2005;40(11):715-724.DOI 10.1097/01.rli.0000184756.66360.d3.

**[18]**. Ding Y, Mason RP, McColl RW, et al. Simultaneous measurement of tissue oxygen level-dependent (TOLD) and blood oxygenation level-dependent (BOLD) effects in abdominal tissue oxygenation level studies. *J Magn Reson Imaging.* 2013;38(5):1230-1236.10.1002/jmri.24006.

**[19]**. O'Connor JP, Naish JH, Parker GJ, et al. Preliminary study of oxygen-enhanced longitudinal relaxation in MRI: a potential novel biomarker of oxygenation changes in solid tumors. *Int J Radiat Oncol Biol Phys.* 2009;75(4):1209-1215.10.1016/j.ijrobp.2008.12.040.

**[20]**. Ogawa S, Lee TM, Kay AR, Tank DW. Brain magnetic resonance imaging with contrast dependent on blood oxygenation. *Proc Natl Acad Sci U S A.* 1990;87(24):9868-9872.10.1073/pnas.87.24.9868.

**[21]**. Pauling L, Coryell CD. The Magnetic Properties and Structure of Hemoglobin, Oxyhemoglobin and Carbonmonoxyhemoglobin. *Proc Natl Acad Sci U S A.* 1936;22(4):210-216.10.1073/pnas.22.4.210.

**[22]**. Crane JM, Van den Hof MC, Dodds L, Armson BA, Liston R. Maternal complications with placenta previa. *Am J Perinatol.* 2000;17(2):101-105.10.1055/s-2000-9269.

**[23]**. Alfirevic Z, Roberts D, Martlew V. How strong is the association between maternal thrombophilia and adverse pregnancy outcome? A systematic review. *Eur J Obstet Gynecol Reprod Biol.* 2002;101(1):6-14.10.1016/s0301-2115(01)00496-1.

**[24]**. Burton GJ, Fowden AL, Thornburg KL. Placental Origins of Chronic Disease. *Physiol Rev.* 2016;96(4):1509-1565.10.1152/physrev.00029.2015.

**[25]**. Thornburg KL, O'Tierney PF, Louey S. Review: The placenta is a programming agent for cardiovascular disease. *Placenta.* 2010;31 Suppl:S54-59.10.1016/j.placenta.2010.01.002.

**[26]**. Thornburg KL, Shannon J, Thuillier P, Turker MS. In utero life and epigenetic predisposition for disease. *Adv Genet.* 2010;71:57-78.10.1016/B978-0-12-380864-6.00003-1.

**[27]**. Georgiades P, Ferguson-Smith AC, Burton GJ. Comparative developmental anatomy of the murine and human definitive placentae. *Placenta.* 2002;23(1):3-19.10.1053/plac.2001.0738.

**[28]**. Rai A, Cross JC. Development of the hemochorial maternal vascular spaces in the placenta through endothelial and vasculogenic mimicry. *Dev Biol.* 2014;387(2):131-141.10.1016/j.ydbio.2014.01.015.

**[29]**. Duley L. The global impact of pre-eclampsia and eclampsia. *Semin Perinatol.* 2009;33(3):130-137.10.1053/j.semperi.2009.02.010.

**[30]**. Duley L. Pre-eclampsia, eclampsia, and hypertension. *BMJ Clin Evid.* 2011;2011

**[31]**. Romo A, Carceller R, Tobajas J. Intrauterine growth retardation (IUGR): epidemiology and etiology. *Pediatr Endocrinol Rev.* 2009;6 Suppl 3:332-336

**[32]**. Heerema-McKenney A. Defense and infection of the human placenta. *APMIS.* 2018;126(7):570-588.10.1111/apm.12847.

# Chapter 2: Bayesian Modeling of MR Data Determines the Most Probable Model[1]

## 2.1 Introduction

Essentially all data analysis employs a data model (or data representation), either explicitly or implicitly. Generally, the data are considered to be the sum of the signal plus noise and it is the estimated signal model parameters that are of primary interest. In the ideal case, the underlying principles governing the measurement protocol and the signal response are known and form the basis of the signal model. Often, however, this is not the case and there exists a cohort of competing signal models from which to choose. This may be because the underlying principles are not fully known or because the underlying principles dictate a signal model that is too complex for meaningful comparison to data that are insufficiently informative and, thus, simplified models based on the full complex model must be considered. In either case, the analyst is faced with the model selection problem, specifically, choosing which of a cohort of competing signal models best represents the data, without "over fitting" (i.e., fitting the noise).

Bayesian probability theory based model selection provides the optimal answer to this challenge. Bayesian analysis is "optimal" in the sense that other methods can approach, but not surpass, the Bayesian result. To determine the optimal model amongst a cohort

---

[1] All contents in this chapter have been published in Meinerz K, Beeman SC, Duan C, Bretthorst GL, Garbow JR, Ackerman JJH. Bayesian Modeling of NMR Data: Quantifying Longitudinal Relaxation in Vivo, and in Vitro with a Tissue-Water-Relaxation Mimic (Crosslinked Bovine Serum Albumin). *Appl Magn Reson*. 49(1):3-24. (2018). doi: https://doi.org/10.1007/s00723-017-0964-z

of competing models, it is necessary to balance the degree of accuracy to which the model recapitulates the data (the goodness of fit, characterized by the residuals) against the number of free parameters in each model (the complexity). Conceptually, the law of parsimony, or Occam's razor, achieves such balance, to wit, "Plurality must not be posited without necessity", i.e., amongst competing hypotheses, the simplest is best. Occam's razor is implicit in Bayesian probability theory. Indeed, Cox's theorem [1] and its further elaboration by Jaynes [2, 3] states that Bayesian probability theory is the optimal method for making quantitative inference about data (i.e., optimally balancing model goodness of fit against model complexity).

In brief, Bayesian probability theory quantifies the probability for a model/hypothesis, described by a posterior probability distribution, given the evidence (data) and all prior information about the system. In a qualitative sense, the posterior probability for a model is inversely related to the aggregate calculated uncertainty over all parameter estimates in a given model. (A more quantitative description of posterior probabilities is provided in Methods.) This qualitative description is useful, in that it highlights the intrinsic penalties associated with: (i) the evidence – uncertainty in the evidence, in the form of noisy and/or sparse data, propagates into calculated posterior probability distributions, and (ii) the model/hypothesis – increased parameterization/complexity must result in substantially reduced aggregate uncertainty for a more complex model to be favored (satisfaction of Occam's razor).

MRI pulse sequences that leverage relaxation properties (e.g., $T_1$, $T_2$, $T_2$*) of the tissue water $_1$H magnetization, i.e., that yield a relaxation-dependent signal-intensity (relaxation-dependent "contrast"), form the foundation of a wide range of important research and clinical MRI protocols. Recently, a number of MRI protocols have been reported that seek to exploit the effect of dissolved oxygen ($O_2$, paramagnetic) on the longitudinal relaxation of tissue water, thereby providing image contrast related to tissue oxygen content [4-7]. However, water relaxation in tissue is complicated by competing mechanisms (e.g., magnetization transfer) [8-11] and confounds (e.g., blood flow) [4] and, while the MRI literature is dominated by monoexponential relaxation modeling, such an approach is oversimplified.

Our interest in quantifying tissue water longitudinal relaxation stems from the possibility of creating images in which voxel intensities reflect the dissolved $O_2$ content. Molecular oxygen, $O_2$, is slightly paramagnetic and, thus, acts as a relaxation agent, albeit with a small relaxivity ($mM_{-1}sec_{-1}$). The underlying question is then, “Can we make tissue water longitudinal relaxation measurements of sufficient accuracy and precision so as to quantify the content of dissolved $O_2$”? The two principal tissue water relaxation mechanisms that compete with dissolved paramagnetic $O_2$ are: (i) magnetization transfer (through-space and chemical exchange) with the tissue’s “macromolecular matrix” and (ii) blood flow, which can bring equilibrium magnetization into the selected image slice. The “apparent” relaxation effects of blood flow can be largely mitigated by appropriate choice of pulse-sequence and are not dealt with here. However, to explore the effects of magnetization transfer on tissue water relaxation data and modeling thereof, we have employed cross-linked BSA (x-BSA) as a tissue mimic, one that exhibits strong magnetization transfer effects but, of course, none of the confounds introduced by blood flow. Given this tissue mimic, the question is then how to best model the relaxation data, the model selection challenge.

Biophysical modeling of tissue water longitudinal relaxation has been a topic of investigation for decades. A monoexponential function is the simplest and most commonly used relaxation model [4, 12, 13]. Use of this model assumes that there effectively exists a single, uniform population of water molecules (extreme narrowing) that can be characterized by a single longitudinal relaxation rate constant. Some have modeled tissue water longitudinal relaxation as a biexponential function, with two distinct ("slow" and "fast") relaxation populations [8, 10]. However, the assumption of two relaxation populations is undoubtedly a simplification and the heterogeneity of tissue microstructure has led others to model relaxation based on a pseudo-continuous distribution of relaxation populations, each with a unique relaxation rate constant [14]. The stretched exponential characterizes such a system with a single relaxation rate constant and a "stretching" parameter, $\alpha$, which describes, empirically, the unknown distribution of relaxation populations. Alternatively, the distribution can be explicitly assumed in the model, with Gaussian [15] and gamma [15] functions serving as the most common distributions.

Bayesian model selection is broadly applicable to a wide range of NMR data-analysis problems when a selection from amongst a cohort of competing signal models must be made. In the present paper, we illustrate the use of Bayesian probability theory for data-driven model selection using longitudinal relaxation data obtained *in vivo* (mouse brain white matter) and *in vitro* with a tissue surrogate (xBSA). Water $_1$H magnetization relaxation data were acquired with a high signal-to-noise ratio (SNR) and high sampling density (regarding post inversion delay times, TIs) to compare amongst a cohort of competing, semi-empirical relaxation models under near ideal circumstances. SNR and sampling density were degraded in these same datasets to examine the impact of data quality on “optimal” (most probable) relaxation model selection and derived parameter estimates. As the data quality decreases, becoming less informative, complex models become less probable and simpler models are preferred, a quantitative, statistical (probabilistic) manifestation of Occam’s razor.

## 2.2 Methods

### 2.2.1 Phantom Preparation and Data Acquisition

Samples of cross-linked 15% (by weight) bovine serum albumin (xBSA) were prepared by diluting a 30% BSA solution (Sigma Aldrich, St. Louis, MO, USA) using phosphate buffered saline (PBS, pH 7.4). Samples were cross-linked using a 2.5% (by volume) solution of 50% glutaraldehyde (Electron Microscopy Sciences, Hatfield, PA, USA). Samples were stirred with a spatula for one minute and then placed in the refrigerator (~$4_{o}$C) for two days. Four cylindrical pieces of xBSA were then extruded and each was placed into a 5 mm, susceptibility-matched, symmetrical NMR microtube (Shigemi Inc, Allison Park, PA, USA) and maintained at 37°C for ~24 hours prior to data acquisition.

$_{1}$H NMR relaxation experiments were performed on a 500-MHz (11.74 T) Agilent/Varian high-resolution NMR spectrometer. Most longitudinal relaxation data were collected using a Modified Fast Inversion Recovery (MFIR) pulse sequence [16], as shown in Figure 2.1A. Acquisition parameters were: 10,000 Hz bandwidth, 2,500 complex data points, water $_{1}$H linewidth ~60 Hz, 96 exponentially spaced inversion delay times (TI) ranging from 5 ms to 7.5 s, and 96 exponentially spaced wait times (W) ranging from 8.495 s to 1 s. Values of TI and W were chosen such that the total repetition time (TR = W + TI) was a constant value of 8.5 s. Four phase-cycled transients were collected for each TI; short, square, RF pulses were employed for inversion ($\theta_1$ ~22 μs; 180 degrees) and readout ($\theta_2$ ~1.5 μs; 10 degrees); and two steady-state (‘dummy scan’) acquisitions were utilized. A 1-ms crusher gradient was applied following the inversion pulse to suppress any residual transverse magnetization arising from imperfect inversion. Relaxation data for each of the four samples were acquired in triplicate, resulting in twelve total datasets.

A separate set of experiments was performed to compare data acquired with the MFIR pulse sequence to data acquired with the standard Inversion Recovery (IR) pulse sequence under two different conditions. Acquisition parameters for the MFIR experiment were: 10,000 Hz bandwidth, 2,500 complex data points, water $_1$H linewidth ~150 Hz, 64 exponentially spaced inversion delay times (TI) ranging from 5 ms to 7.5 s, and 64 exponentially spaced wait times (W) ranging from 8.495 s to 1 s. Values of TI and W were chosen such that the total repetition time (TR = W + TI) was a constant value of 8.5 s. Four phase-cycled transients were collected for each TI; square, RF pulses were employed for inversion and readout; and five steady-state (‘dummy scan’) acquisitions were utilized. Acquisition parameters for the IR experiment were: 64 exponentially spaced inversion delay times (TI) ranging from 5 ms to 7.5 s, and a relaxation delay time (time following the $\theta_2$ readout pulse) of 10 s. All other parameters were the same as the MFIR experiment.

For these comparative experiments, two sets of square, RF pulse widths were utilized, designated as either “short” (broad excitation bandwidth) or “long” (narrow excitation bandwidth). For the short pulse width condition, the inversion pulse $\theta_1$ ~22 μs (180 degrees) and the observation pulse $\theta_2$ ~11 μs (90 degrees). For the long pulse width condition, the inversion pulse $\theta_1$ ~1.3 ms (180 degrees) and the observation pulse $\theta_2$ ~650 μs (90 degrees). All relaxation data (MFIR vs. IR; short vs. long pulses) were acquired in interleaved fashion in triplicate on a single sample, resulting in three replicate datasets for each of the four protocols.

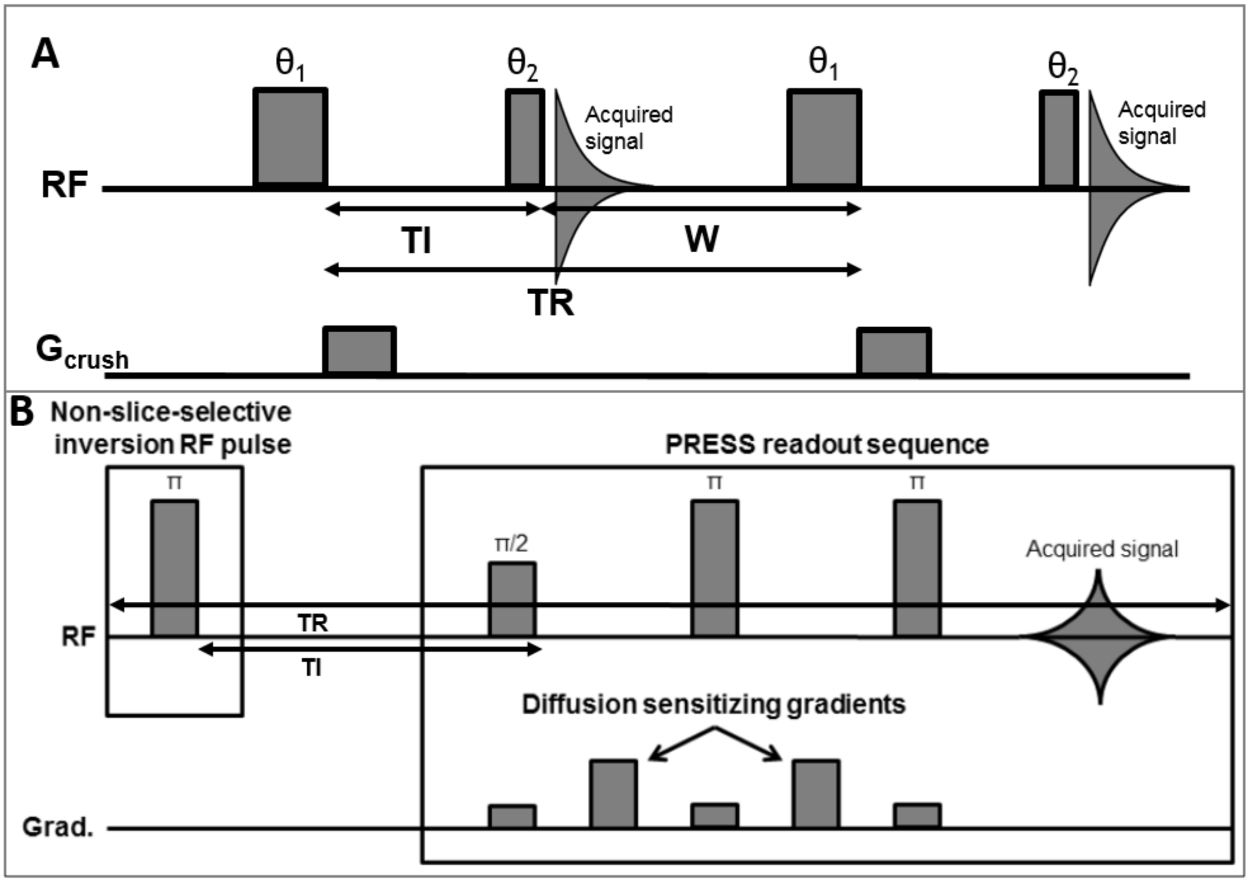

**Figure 2.1. A)** Schematic illustration of the Modified Fast Inversion Recovery (MFIR) pulse sequence [16]. RF refers to the radio frequency output and signal acquisition: $\theta_1$ is a 180 degree (π) inversion pulse, $\theta_2$ is a 10 degree magnetization sampling pulse. $G_{crush}$ represents the magnetic field gradient pulse applied to destroy (crush) any transverse magnetization coherence produced following a non-ideal $\theta_1$ inversion pulse. TI is the variable time from the inversion pulse to the magnetization sampling pulse, W is the waiting time, and TR is the time to repetition. TR is the sum of TI and W and is a constant value. **B)** Schematic illustration of the Inversion Recovery Point Resolved Spectroscopy (IR-PRESS) pulse sequence. A non-slice-selective inversion pulse is followed by a PRESS readout sequence, employing weak diffusion sensitizing gradients to destroy

transverse magnetization coherence within the vasculature (i.e., to suppress signal from flowing blood).

### 2.2.2 In Vivo Subject Preparation and Data Acquisition

All animal experiments were approved by the Washington University Institutional Animal Care and Use Committee. *In vivo* $^1$H relaxation data were collected on a 4.7-T small-animal MRI system (Agilent Technologies, Santa Clara, CA, USA) using a laboratory-built, actively decoupled, volume-transmit/surface-receive coil pair. One 200 g female Sprague Dawley Rat was anesthetized with 1% isoflurane in 100% $O_2$, and body temperature was monitored with a rectal thermometer and maintained at 37$^o$C *via* the combination of circulating warm water and warm air. An Inversion Recovery Point RESolved Spectroscopy (IR-PRESS) sequence selecting a 1.6 x 1.6 x 1.6 mm$^3$ voxel was modified to minimize apparent relaxation contributions from blood flow, as shown in Figure 2.1B. Specifically, the sequence employed: (i) a non-slice-selective inversion pulse, followed by 8-gauss/cm crusher gradients applied along all three axes to destroy any transverse magnetization created by an imperfect inversion pulse, and (ii) weak, diffusion-sensitizing gradients applied along all three axes (total b = 100 s/mm$^2$) to destroy any transverse coherence of blood-water $^1$H magnetization flowing into the PRESS voxel *via* the vasculature. Acquisition parameters were: 4006 Hz bandwidth, 2048 complex data points, water $^1$H linewidth ~11 Hz, 128 exponentially spaced inversion delay times (TI), ranging from 0.0075 sec to 4.25 sec, effective echo time (TE) of 20 ms and a repetition time (TR) of 5 sec. Relaxation data were collected in triplicate from the corpus callosum (white matter).

## 2.3 Mathematical Models

The monoexponential relaxation model is given by:

$$M_z\,(t) = \; A * \exp(-t * R_1) + C, \qquad [2.1]$$

in which $M_z(t)$ is the net longitudinal magnetization, A is a constant amplitude, t is time (corresponding to the inversion delay time, TI, in our experiments), $R_1$ is the longitudinal relaxation decay rate constant, and C is a constant offset. Similarly, the biexponential model can be written as:

$$M_z(t) = A * \left[F * \exp\left(-t * R_{1,fast}\right) + (1 - F) * \exp\left(-t * R_{1,slow}\right)\right] + C, \qquad [2.2]$$

in which F is the fraction of the total amplitude of the “fast” relaxation component and (1-F) is the fraction of the “slow” relaxation component. The stretched monoexponential relaxation model is described by inserting a fractional power law into the monoexponential function:

$$M_z(t) = \; A * \exp(-t^{\alpha} * R_1) + C, \qquad [2.3]$$

in which $\alpha$ is the stretching exponent.

Two additional models were considered: A Gaussian-type (normal) distribution function for $R_1$ [15] and an $R_1$ distribution function based on the gamma distribution [15]. The Gaussian-type function is given by:

$$P(R_1) = \begin{cases} A * \exp\left(-\frac{\left(R_1 - R_{1,max}\right)^2}{2\sigma^2}\right) + C, \; R_1 > 0 \\ 0, \; R_1 < 0 \end{cases}, \qquad [2.4]$$

in which A is a normalization constant:

$$A^{-1} = \sigma\sqrt{\frac{\pi}{2}}\left[1 + \Phi\left(\frac{R_{1,max}}{\sigma\sqrt{2}}\right)\right]. \qquad [2.5]$$

$R_{1,max}$ corresponds to the peak of the distribution, σ is the standard deviation of the distribution ($\sigma_2$ is the variance), $\Phi$ is the error function, and C is constant offset. The modified gamma-type distribution is of the form:

$$M_z(t) = M_z(t = 0) * \left(\frac{a}{a+t*R_{1,max}}\right)^{(a+1)} + C, \qquad [2.6]$$

in which $M_z(t=0)$ is the initial net longitudinal magnetization, a is a shape parameter, and C is a constant offset.

### 2.2.4 Bayesian-Based Model Selection

The posterior probability for each of the relaxation models was calculated using Bayes' theorem [2, 3]:

$$P(M|DI) = \frac{P(M|I)P(D|MI)}{P(D|I)}, \qquad [2.7]$$

in which *P(M|DI)* is the posterior probability for a model M, given data D, and prior information I; *P(M|I)* is the prior probability for a model given the prior information; *P(D|MI)* is the probability for the data, given the model and the prior information; and *P(D|I)* is the direct probability for the data, given the prior information. To calculate the posterior probability for a model given the data and the prior information, the direct probability for the data, given the model and the prior information, must first be calculated. As an example, the stretched exponential model has two calculated parameters, $\alpha$ and $R_1$, such that the expansion of $P(D|MI)$ is of the form:

$$P(D|MI) = \int d\alpha dR_1 P(\alpha R_1|MI) P(D|\alpha R_1 MI), \qquad [2.8]$$

in which $P(\alpha R_1|MI)$ is the joint prior probability for $\alpha$ and $R_1$, given the model and the prior information, and $P(D|\alpha R_1 MI)$ is the direct probability, given the parameters, model, and prior information.

In Bayesian probability theory, the entire multidimensional integral or “hypervolume” covering the full range of possible parameter values must be computed and contributes directly to $P(M|DI)$. Every hypervolume is computed by integrating the joint prior probability for the parameters weighted by the direct probability of the data, given the parameters. Using in-house developed Bayesian analysis software (available for free download at bayes.wustl.edu) that utilizes Markov-chain Monte Carlo simulations to approximate the high-dimensional integrals, the posterior probabilities for each of the models, and their associated parameters, were calculated.

In each case, the results shown are from the joint analysis of either three (*in vivo*) or twelve (xBSA) replicate datasets. Generally, in a joint analysis, some of the model parameters are assigned as common (common valued) to all members of the full set of replicate datasets and some are assigned as unique (uniquely valued) to each member of the full set of replicate datasets. In the joint analysis employed herein, the reported model parameters (e.g., relaxation rate constants) were taken as common to all members of the full set of replicate datasets. The values of each of the model’s common parameters that best represented the full set of replicate datasets were taken as optimal (most probable). We note that Bayesian joint analysis is distinct from averaging either the datasets or the parameters estimated from each dataset. In Bayesian joint analysis, the probability distributions weight the parameter estimates toward those favored by the more informative (e.g., higher signal-to-noise, fewer artifacts) members of the full set of replicate datasets. Herein, data quality was relatively uniform (equally informative) across all replicate datasets.

Within the Markov-chain Monte Carlo simulation, 50 parallel simulations were performed to sample the posterior probabilities for the model and its parameters. Simulated annealing brought the 50 simulations into steady-state equilibrium, at which time 50 samples from each of the 50 simulations were drawn. Thus, in total, 2,500 parameter samples were used to characterize the posterior probability density distributions for the models and their parameters.

Herein, the peak (maximum) of the relevant posterior probability density distributions are taken as the optimal (most probable) parameter estimates. Alternatively, one could choose the mean of the distribution. For symmetrical distributions, these choices are, obviously, equivalent. Uncertainty in a given parameter estimate is taken as ± the standard deviation (square root of the variance) of the distribution. More precise parameter estimates are characterized by narrower posterior probability density distributions.

### 2.2.5 Data Truncation, Sampling Density Reduction, and Noise Addition

As will be described, Bayesian model selection heavily favored the biexponential model for the xBSA longitudinal relaxation data (*vide infra*). In this case, the fast relaxation component is characterized by a rate constant that is two orders of magnitude greater than that of the slow relaxation component, but has an amplitude that is only 2% that of the slow component. As a consequence, the available dynamic range and sampling density is limited, until the slow component dominates the signal. In practice, accurate characterization of this small-amplitude fast component will often be impractical due to time constraints and/or insufficient SNR and further, might be uninteresting for some experiments (e.g., contrast agent quantification, when it is expected that the relaxation modulating effects of the agent will only be observable on the slow rate constant). To simulate a potential time saving inversion recovery experiment, we truncated our datasets to include only data points associated with the slow component. Based on estimation of the relaxation rate constant for the fast relaxation component ($R_{1,fast} = 1/T_{1,fast}$) from the joint analysis of twelve full, 96-TI-value datasets, the first 45 TIs were removed, obviating information on relaxation occurring during the period of 5 x $T_{1,fast}$, and the smallest TI was then approximately 160 ms.

To more accurately mimic the *in vivo* case, in which both acquisition time and SNR may be limited, these twelve truncated xBSA relaxation datasets (i.e., minimum TI ~160 ms, data reflecting only the slow relaxation component) were further modified. (i) To simulate the acquisition-time-limited case, the sampling density was made increasingly sparse by iteratively removing every other data point, until only seven TIs remained. Bayesian joint analysis was then performed on the full datasets (51 TIs), intermediate-size datasets (26 TIs), and small-size datasets (7 TIs). (ii) To explore the effect of limited SNR, Gaussian-distributed noise (zero mean, standard deviation of one) was added to each of the twelve full (51 TI values) datasets. Prior to the addition of noise, these *in vitro* xBSA samples exhibit very high SNR (SNR = 600), defined throughout as the signal amplitude at the longest TI value divided by the root mean square noise value. Added Gaussian-distributed noise reduced the SNR to an intermediate value (SNR = 100) and a lower value (SNR = 25) typical of *in vivo* relaxation datasets. Bayesian joint analysis was then performed on the full datasets (51 TIs) at each of the three SNRs. (iii) To determine the combined effects of limited data sampling density and limited SNR on parameter estimation, Gaussian-distributed noise was added to reduce the SNR to an intermediate value (SNR = 100) followed by the reduction of the sampling density to achieve the full datasets (51 TIs), intermediate-size datasets (26 TIs), and small-size datasets (7 TIs). Bayesian joint analysis was then performed on the twelve, intermediate SNR valued datasets at each of the three sampling densities.

## 2.3 Results

As shown in Figure 2.2, Bayesian joint analysis of the twelve full (96 TIs) relaxation datasets, collected using the xBSA sample, selected the biexponential as the heavily favored model. However, residuals from both biexponential and monoexponential models display clear, smooth oscillations, characteristic of under-parameterization, suggesting that the biexponential model does not fully represent xBSA relaxation data characterized by both high signal-to-noise, SNR = 600, and high sampling density, 96 TIs (Figure 2.2B). The root mean squared (RMS) of the residuals of the biexponential model (0.002) was substantially less than that of the monoexponential model (0.011). The resulting parameter estimates from this model are $R_{1,slow} = 0.4164 \pm 0.0003\ s^{-1}$ and $R_{1,fast} = 33.6 \pm 1.1\ s^{-1}$ (Figure 2.2C). The fractions of the total amplitude corresponding to the slow and fast relaxation components are 0.9801 ± 0.0003 and 0.0199 ± 0.0003, respectively. (Note, the amplitude and the rate constant of the fast relaxation component will depend upon the extent of magnetization transfer produced by the relaxation measurement protocol (*vide infra*).) When the monoexponential model is used, $R_1$ is calculated to be 0.4290 ± 0.0008 $s^{-1}$. For comparison, parameter estimates from both the favored biexponential model and the monoexponential model can be found in Table 2.1.

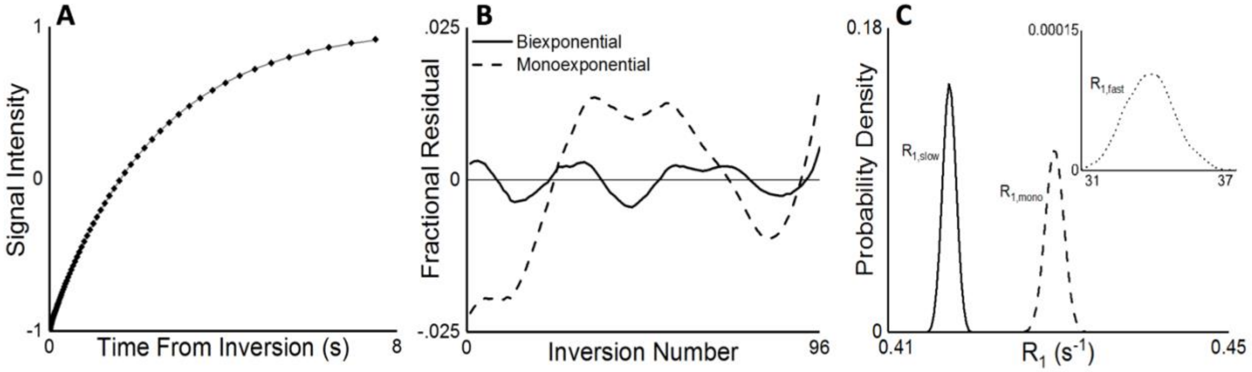

**Figure 2.2. A)** Representative full, 96 TI relaxation dataset (black diamonds: signal intensity *vs.* TI) from the xBSA phantom, fit with the heavily favored biexponential model (gray line). **B)** The resulting residuals from both the biexponential model (solid black line) and the monoexponential model (dashed black line) are plotted against the “inversion number” (i.e., the 96 TI increments arranged linearly by increment number). The biexponential fit has a resulting root mean square (RMS) residual of 0.002, whereas the monoexponential fit has an RMS residual of 0.011. **C)** Bayesian-estimated posterior probability densities from joint analysis of all twelve xBSA relaxation datasets for (i) the rate constant for the slow component from the biexponential fit (solid black line), peaking at $R_{1,slow} = 0.4164 \pm 0.0003$ $s^{-1}$ and (ii) the rate constant from the monoexponential fit (dashed black line), peaking at $R_{1,mono} = 0.4290 \pm 0.0008$ $s^{-1}$; inlaid is the rate constant for the fast component from the biexponential fit (dotted black line), peaking at $R_{1,fast} =$ $33.6 \pm 1.1$ $s^{-1}$.

The biexponential model was also heavily favored by Bayesian joint analysis of three full (128 TIs) *in vivo* datasets collected within the corpus callosum (white matter) of rat brain. The residuals from both the favored biexponential fit and the monoexponential fit show oscillations (Figure 2.3B) that are similar to those seen with the xBSA sample. Similar to the xBSA sample, the RMS of the residuals of the biexponential model (0.007) was less than that of the monoexponential model (0.008), a difference of ~15%, and the resulting parameter estimates for the favored model are $R_{1,slow}$ = 0.681 ± 0.003 s$_{-1}$ and $R_{1,fast}$ = 28.5 ± 2.9 s$_{-1}$ (Figure 2.3C). The fractions of the total amplitude associated with the slow and fast relaxation components are 0.973 ± 0.001 and 0.027 ± 0.001, respectively. By comparison, when the monoexponential model is used, the derived rate constant is $R_1$ = 0.708 ± 0.003 s$_{-1}$. Parameter estimates from both models can be found in Table 2.1.

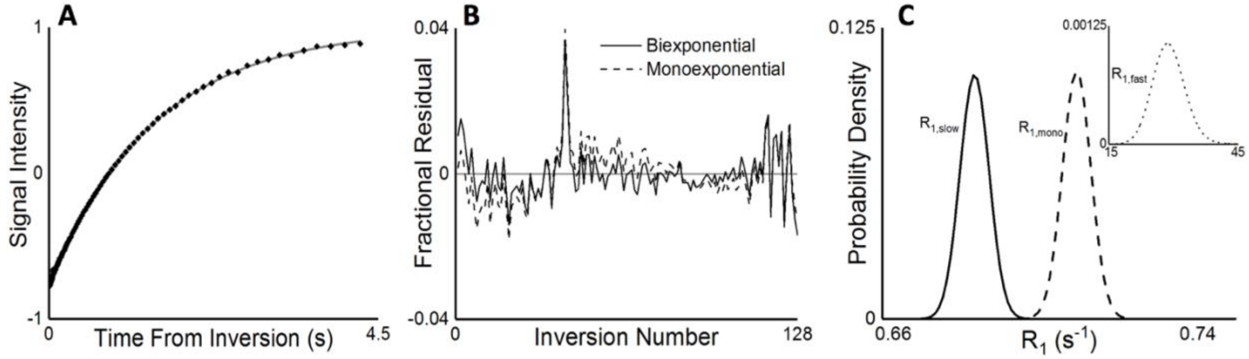

**Figure 2.3. A)** Representative full, 128 TI dataset (black diamonds) from *in vivo* corpus callosum in rat brain, fit with the heavily favored biexponential model (gray line), plotted against the time from the inversion pulse. **B)** Resulting residuals from the favored biexponential fit (solid black line) and the monoexponential model (dashed black line) are plotted against the “inversion number” (i.e., the 128 TI increments arranged linearly by increment number). The biexponential fit achieves an RMS residual value of 0.007, whereas the monoexponential fit achieves a value of 0.008. **C)** Bayesian-estimated posterior probability densities from joint analysis of all three *in vivo* corpus callosum relaxation datasets for (i) the rate constant corresponding to the “slow” relaxation component from the favored biexponential fit (solid black line), peaking at $R_{1,slow}$ = 0.681 ± 0.003 s$_{-1}$ and (ii) the rate constant from the monoexponential model (dashed black line), peaking a $R_{1,mono}$ = 0.708 ± 0.003 s$_{-1}$; inlaid is the rate constant corresponding to the “fast” component from the favored biexponential model (dotted black line), peaking at $R_{1,fast}$ = 28.5 ± 3.0 s$_{-1}$.

**Table 2.1:** Rate Constants and RMS Residuals from xBSA Phantom and *in Vivo* Joint Analyses

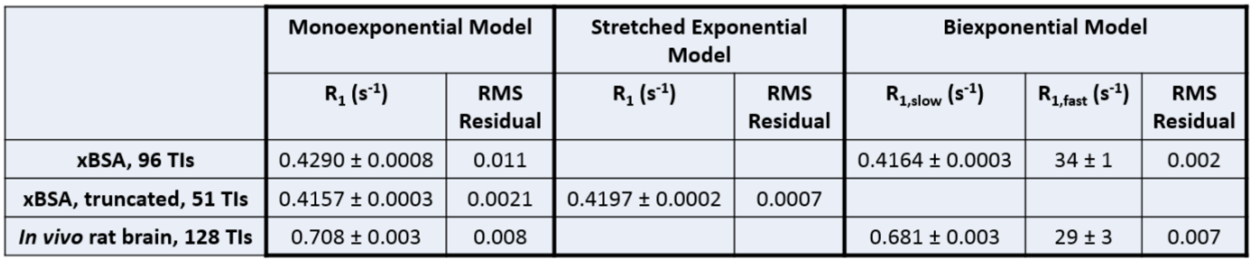

| | **Monoexponential Model** | | **Stretched Exponential Model** | | **Biexponential Model** | | |
|---|---|---|---|---|---|---|---|
| | **$R_1$ ($s^{-1}$)** | **RMS Residual** | **$R_1$ ($s^{-1}$)** | **RMS Residual** | **$R_{1,slow}$ ($s^{-1}$)** | **$R_{1,fast}$ ($s^{-1}$)** | **RMS Residual** |
| **xBSA, 96 TIs** | 0.4290 ± 0.0008 | 0.011 | | | 0.4164 ± 0.0003 | 34 ± 1 | 0.002 |
| **xBSA, truncated, 51 TIs** | 0.4157 ± 0.0003 | 0.0021 | 0.4197 ± 0.0002 | 0.0007 | | | |
| ***In vivo* rat brain, 128 TIs** | 0.708 ± 0.003 | 0.008 | | | 0.681 ± 0.003 | 29 ± 3 | 0.007 |

Following truncation of the xBSA datasets as described in Methods, twelve datasets, corresponding to the slow relaxation component (51 Tis; Figure 2.4), were analyzed jointly and the stretched exponential model was found to be heavily favored. Residuals from the stretched exponential model and the monoexponential model (Figure 2.4B) show similar oscillatory patterns as in the full xBSA relaxation dataset, suggesting that neither model is able to characterize fully the longitudinal relaxation of the sample. However, it is evident from the RMS residuals that the stretched exponential model (0.0007) achieves a better goodness of fit than the monoexponential model (0.0021). The resulting parameter estimates from this model are $R_1$ = 0.4197 $s_{-1}$ ± 0.0002 $s_{-1}$ (Figure 2.4C) with $\alpha$ = 0.9759 ± 0.0004. When the monoexponential model is used, the derived rate constant $R_1$ is found to be 0.4157 ± 0.0003 $s_{-1}$.

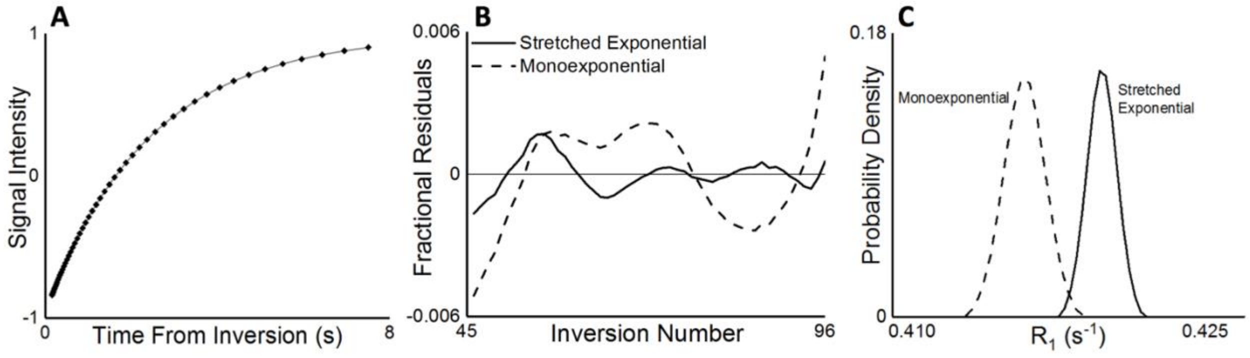

**Figure 2.4. A)** Representative truncated dataset from xBSA phantom illustrating the “slow” relaxation component (black diamonds), fit with the heavily favored stretched exponential model (gray line), plotted against the time from the inversion pulse. **B)** The resulting residuals from the heavily favored stretched exponential model (solid black line) and the monoexponential model (dashed black line) are shown against the “inversion number” (i.e., the 51 TI increments arranged linearly by increment number). The stretched exponential fit achieves an RMS residual value of 0.0007, whereas the monoexponential fit achieves an RMS residual value of 0.0021. **C)** Bayesian-estimated posterior probability densities from joint analysis of all twelve truncated datasets for the rate constants from (i) the favored stretched exponential (solid black line), peaking at $R_1 = 0.4197 \pm 0.0002$ $s_{-1}$ and (ii) the monoexponential model (dashed black line), peaking at $R_1 = 0.4157 \pm 0.0003$ $s_{-1}$.

Modification of the truncated (slow relaxation component only) xBSA datasets to more closely approach the *in vivo* case with respect to either limited sampling density, SNR, or the combination thereof, leads to Bayesian-estimated posterior probability densities for the stretched exponential with respect to the number of TIs (Figure 2.5A, Table 2.2), the SNR (Figure 2.6), and the number of TIs at decreased SNR (Figure 2.5B). In the case of high SNR with decreasing sampling density, the resulting parameter estimates are (Figure 2.5A) $R_1 = 0.4197 \pm 0.0002$ $s_{-1}$ and $\alpha = 0.9760 \pm 0.0004$ for 51 TIs; $R_1 = 0.4197 \pm 0.0002$ $s_{-1}$ and $\alpha = 0.9759 \pm 0.0006$ for 26 TIs; and $R_1 = 0.4195 \pm 0.0004$ $s_{-1}$ and $\alpha = 0.9769 \pm 0.0013$ for 7 TIs. The stretched exponential is favored in all cases. The resulting parameter estimates in the case of high sampling density, 51 TIs, with decreasing SNR

(Figure 2.6, Table 2.3) are $R_1$ = 0.4197 ± 0.0002 $s^{-1}$ and $\alpha$ = 0.9759 ± 0.0004 for SNR = 600; $R_1$ = 0.4187 ± 0.0011 $s^{-1}$ and $\alpha$ = 0.9746 ± 0.0035 for SNR = 100; and $R_1$ = 0.4228 ± 0.0041 $s^{-1}$ with $\alpha$ = 0.9733 ± 0.0130 for SNR = 25. The stretched exponential model is heavily favored for the SNR = 600 and SNR = 100 datasets, as denoted by the asterisk (*) in the figure. For the monoexponential model (Figure 2.6C) the resulting parameter estimates are $R_1$ = 0.4157 ± 0.0003 $s^{-1}$ for SNR = 600; $R_1$ = 0.4145 ± 0.0010 $s^{-1}$ for SNR = 100; and $R_1$ = 0.4185 ± 0.0035 $s^{-1}$ for SNR = 25 (for which the monoexponential model was favored). In the case of intermediate signal (SNR = 100) with decreasing sampling density, the resulting parameter estimates are (Figure 2.5B, Table 2.2) $R_1$ = 0.4187 ± 0.0011 $s^{-1}$ and $\alpha$ = 0.9746 ± 0.0035 for 51 TIs; $R_1$ = 0.4183 ± 0.0014 $s^{-1}$ and $\alpha$ = 0.9696 ± 0.0043 for 26 TIs; and $R_1$ = 0.4179 ± 0.0015 $s^{-1}$ and $\alpha$ = 0.9631 ± 0.0045 for 7 TIs. The stretched exponential is favored in all cases.

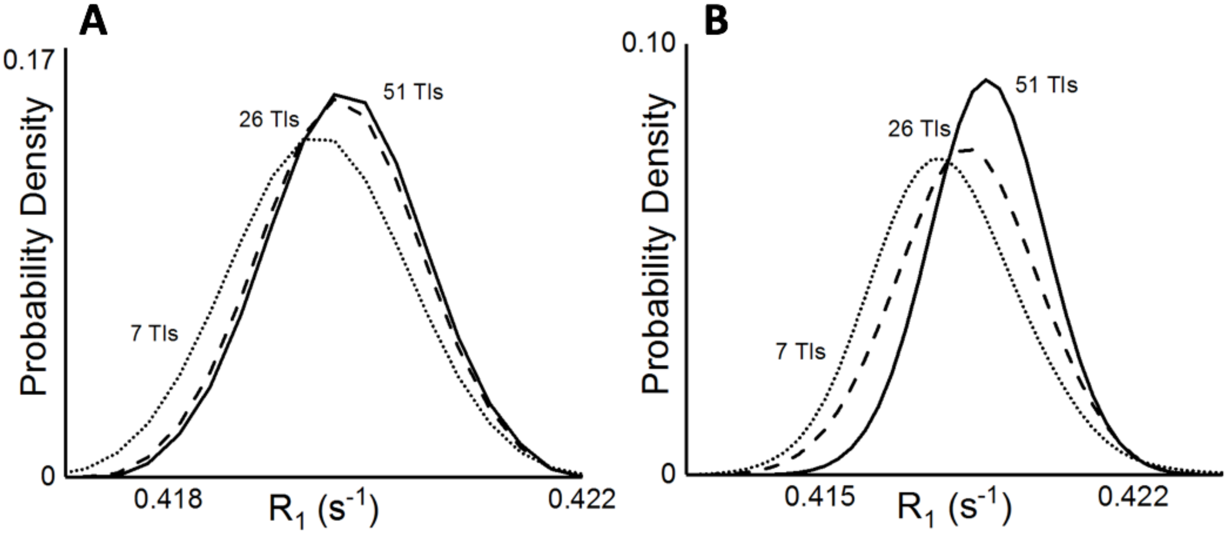

**Figure 2.5.** Bayesian-estimated posterior probability density of the heavily favored, stretched exponential model's decay-rate constant, $R_1$, **(A)** for the case of 51 TIs (solid black line) peaking at $R_1$ = 0.4197 ± 0.0002 $s^{-1}$, 26 TIs (solid gray line) peaking at $R_1$ = 0.4197 ± 0.0002 $s^{-1}$, and 7 TIs (dotted black line) peaking at $R_1$ = 0.4195 ± 0.0004 $s^{-1}$

following truncation of the original 96 TI datasets. **B)** The same culled datasets as in **(A)** following the addition of Gaussian-distributed noise to reduce the SNR to approximately 100. For each case, the heavily favored model is the stretched exponential and the $R_1$ is found to be 0.419 ± 0.001 s$_{-1}$ for 51 TIs, 0.418 ± 0.001 s$_{-1}$ for 26 TIs, and 0.418 ± 0.002 s$_{-1}$ for 7 TIs. Each posterior probability density curve is the result of twelve jointly analyzed xBSA relaxation datasets.

**Table 2.2:** Sparsity & SNR Reduction Effects Upon Parameter Estimates in xBSA Phantom

| TI > 5*$T_{1,fast}$ (160 ms – 7.5 s) | SNR = 600 | | SNR = 100 | |
|---|---|---|---|---|
| | $R_1$ ($s^{-1}$) | α | $R_1$ ($s^{-1}$) | α |
| **51 TIs** | 0.4197 ± 0.0002 | 0.9760 ± 0.0004 | 0.419 ± 0.001 | 0.975 ± 0.004 |
| **26 TIs** | 0.4197 ± 0.0002 | 0.9759 ± 0.0006 | 0.418 ± 0.001 | 0.970 ± 0.004 |
| **7 TIs** | 0.4195 ± 0.0004 | 0.977 ± 0.001 | 0.418 ± 0.002 | 0.963 ± 0.005 |

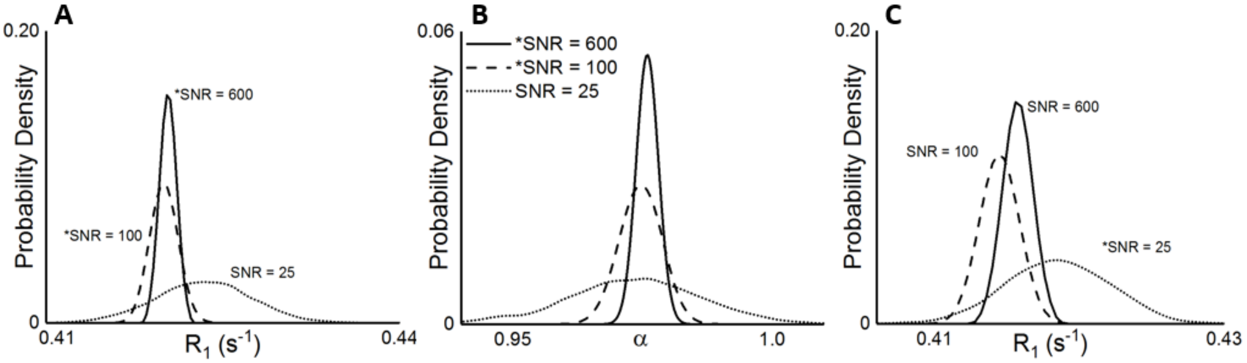

**Figure 2.6.** Bayesian-estimated posterior probability densities for the cases of SNR = 600 (solid black line), SNR = 100 (solid gray line), and SNR = 25 (dotted black line) for the "slow" relaxation component (51 TIs) following the addition of Gaussian-distributed noise. **A)** The posterior probability densities for the $R_1$ determination, using the stretched exponential model. The case of SNR = 600 peaks at $R_1$ = 0.4197 ± 0.0002 s$_{-1}$, SNR = 100 peaks at $R_1$ = 0.419 ± 0.001 s$_{-1}$, and SNR = 25 peaks at $R_1$ = 0.423 ± 0.004 s$_{-1}$. **B)** The corresponding posterior probability densities for $\alpha$ in each of the three cases. When SNR = 600, $\alpha$ peaks at 0.9759 ± 0.0004; for SNR = 100, $\alpha$ peaks at 0.975 ± 0.004; for SNR = 25, $\alpha$ peaks at 0.97 ± 0.01. **C)** The posterior probability densities for the $R_1$ determination using the monoexponential model. The case of SNR = 600 peaks at $R_1$ = 0.4157 ± 0.0003 s$_{-1}$, SNR = 100 peaks at $R_1$ = 0.415 ± 0.001 s$_{-1}$, and SNR = 25 peaks at

$R_1 = 0.419 \pm 0.004$ s$^{-1}$. In each case, if the model used was the favored model, an asterisk (*) accompanies the label. The heavily favored model for the SNR = 600 and SNR = 100 was found to be the stretched exponential and for the case of SNR = 25 the heavily favored model was found to be the monoexponential.

**Table 2.3:** Parameter Estimates for xBSA Phantom Following SNR Reduction

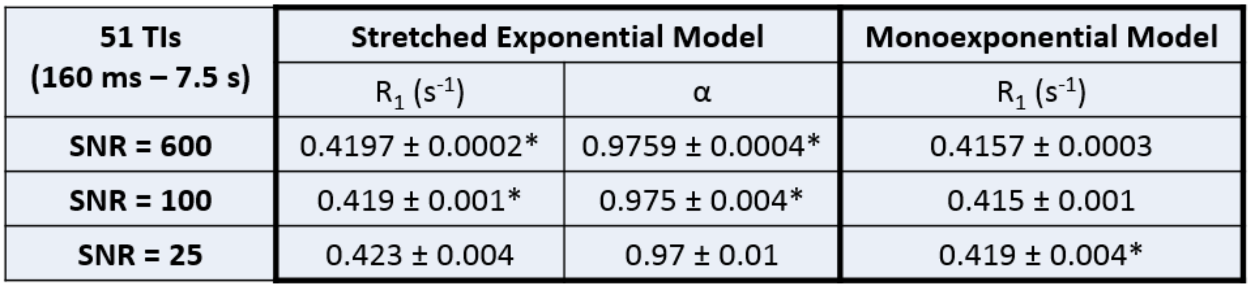

| 51 TIs (160 ms – 7.5 s) | Stretched Exponential Model | | Monoexponential Model |
|---|---|---|---|
| | $R_1$ (s$^{-1}$) | α | $R_1$ (s$^{-1}$) |
| **SNR = 600** | 0.4197 ± 0.0002* | 0.9759 ± 0.0004* | 0.4157 ± 0.0003 |
| **SNR = 100** | 0.419 ± 0.001* | 0.975 ± 0.004* | 0.415 ± 0.001 |
| **SNR = 25** | 0.423 ± 0.004 | 0.97 ± 0.01 | 0.419 ± 0.004* |

* denotes favored model.

To validate methodology employed herein for quantifying relaxation, data acquired with the MFIR protocol were compared to data acquired with the standard inversion recovery (IR) protocol under two conditions: (i) short 90 and180 degree RF-pulses ($\theta_2$ and $\theta_1$, respectively), as are commonly employed with high resolution (analytical) NMR spectrometers, herein ~10 and 20 µs, respectively; and (ii) long 90 and 180 degree RF-pulses as are commonly employed with MRI scanners, herein ~650 and 1,300 µs, respectively. Data were acquired in triplicate on a single xBSA sample, interleaving the MFIR and IR protocols. When short pulses yielding broad excitation bandwidths were employed, the MFIR and IR protocols resulted in essentially identical parameter estimates for the most probable model, biexponential. When long pulses yielding narrow excitation bandwidths were employed, the MFIR and IR protocols again resulted in essentially identical parameter estimates for the most probable model, biexponential. Of particular note, however, the estimated fractional amplitude of the fast relaxation component (F) increased markedly from ~3% with short (broadband) pulses to ~20% with long (narrow band) pulses. Consistent with the signal-to-noise increase for the fast relaxation component, and corresponding decrease for the slow component, the uncertainly in the estimated $R_{1,fast}$ decreased and that for the estimated $R_{1,slow}$ increased [17]. These results are summarized in Table 2.4.

**Table 2.4:** Summary of Parameter Estimates for xBSA Phantom Comparing MFIR & IR *vs.* Pulse Width

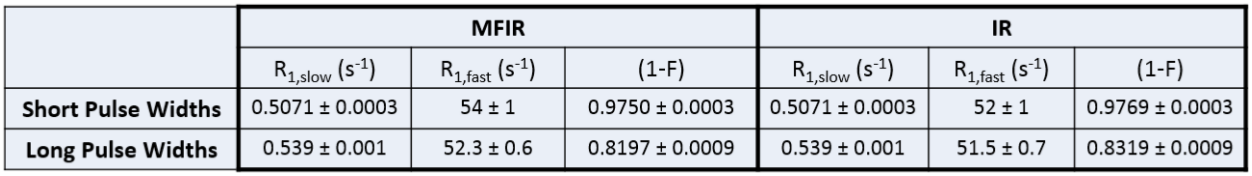

| | MFIR | | | IR | | |
|---|---|---|---|---|---|---|
| | $R_{1,slow}$ ($s^{-1}$) | $R_{1,fast}$ ($s^{-1}$) | (1-F) | $R_{1,slow}$ ($s^{-1}$) | $R_{1,fast}$ ($s^{-1}$) | (1-F) |
| **Short Pulse Widths** | 0.5071 ± 0.0003 | 54 ± 1 | 0.9750 ± 0.0003 | 0.5071 ± 0.0003 | 52 ± 1 | 0.9769 ± 0.0003 |
| **Long Pulse Widths** | 0.539 ± 0.001 | 52.3 ± 0.6 | 0.8197 ± 0.0009 | 0.539 ± 0.001 | 51.5 ± 0.7 | 0.8319 ± 0.0009 |

## 2.4 Discussion

The biexponential model is heavily favored for the high SNR, high sampling density, relaxation datasets from both the xBSA phantom and mouse brain (white matter) *in vivo*, supporting the conclusion that the xBSA phantom is a good *in vitro* longitudinal relaxation surrogate for tissue [8, 10]. In addition, both samples (xBSA, *in vivo* brain) yield derived model parameters that have similar characteristics: (i) the relaxation rate constants associated with the fast and slow relaxation components are well-resolved, separated by two orders of magnitude, and (ii) the fractions of the total amplitude attributable to the fast and slow relaxation components from the xBSA phantom and the *in vivo* results are comparable. Though the *in vivo* and *in vitro* data were collected at different magnetic field strengths – 200 MHz and 500 MHz, respectively – and, thus, the $R_1$ values cannot be directly compared, as expected, relaxation of the dominant component ($R_{1,slow}$) at 11.74

T *vs.* 4.7 T is less efficient due to reduced spectral density at the higher resonance frequency. Finally, the residuals from the biexponential modeling of both the xBSA and *in vivo* datasets show the same systematic oscillatory feature, indicating that, while the model captures well the principal features of the signal, it does not fully characterize the data. However, when tested against a triexponential function, Bayesian model selection still heavily favored the biexponential model in both the *in vitro* and *in vivo* cases (data not shown). In Bayesian analysis, each additional parameter added to a model naturally incurs a penalty related to the posterior probability distribution of that parameter, so that more complex models (models with more parameters) must markedly improve the goodness of fit (e.g., chi squared) or be rejected, a manifestation of Occam's razor.

The failure of a triexponential function to improve the modeling indicates that the penalty associated with adding two additional parameters (a third rate constant and associated fractional amplitude) more than offsets any resulting improvement in the goodness of fit. The failure of the triexponential model, of course, does not preclude the use of other models that might better describe the system. Having demonstrated that the xBSA phantom mimics *in vivo* tissue longitudinal relaxation will allow us to utilize this phantom in future experiments as a tissue surrogate to further probe the $R_1$ measurement as regards modifiers of interest, e.g., pH, protein content, $pO_2$.

As the monoexponential model is used frequently to fit longitudinal relaxation data, the residuals and the Bayesian-estimated posterior probability distributions from the favored model were compared with those from the monoexponential model for the full, 96 TIs, and truncated, 51 TIs, xBSA relaxation datasets, and the *in vivo* datasets, 128 TIs. In all cases, we observe a clear shift in the location of the peak (maximum probability) of the posterior probability distribution for the slow decay-rate constant derived with the favored model *vs.* the rate constant posterior probability distribution derived from a monoexponential fit. The monoexponential model is a relatively poor representation of the system, lacking sufficient parameters to accurately characterize the longitudinal relaxation, especially for the early time points (short TI values). For both the full xBSA and *in vivo* datasets, the monoexponential model attempts to characterize both the fast and slow components with a single rate constant, resulting in a skewed parameter estimation. Attempting to fit a dataset with a model that lacks sufficient complexity may yield a precise parameter estimate(s) that is not accurate, as seen in Figures 2.2C (full xBSA dataset), 2.3C (*in vivo* dataset), and 2.4C (truncated xBSA dataset). In each case, however, the change in the uncertainty of the estimated rate constant from the preferred rate-constant model is insignificant compared to that derived from the less probable, simple monoexponential model.

As noted, given its rapid decay and small fractional amplitude, it is difficult to characterize accurately the fast relaxation component. This will be especially true in relaxation experiments *in vivo*, in which acquisition time and SNR are limiting. Consequently, it is worth considering how to collect data corresponding only to the slow component, and to consider how doing so may affect the derived parameters. Using the resulting $T_{1,fast}$ from the joint analysis of twelve full xBSA datasets with 96 TIs, the time t = 5 x $T_{1,fast}$ was calculated and the data points collected at shorter TI values were dropped (truncated) from the dataset. In principle, at TI = 5 x $T_{1,fast}$, >99% of the fast relaxation component will have returned (decayed) to thermal equilibrium polarization so that, in effect, all of the relaxation signal derives from the slow relaxation component. Therefore, it would seem logical that the favored (most probable) relaxation model describing the truncated data would be monoexponential. Instead, however, these data were best described by the stretched exponential model. As illustrated by the estimated parameter values shown in Results, the stretching parameter ($\alpha$) is very close to 1 and, therefore, the stretched model is not far removed from a pure monoexponential. However, as shown in Figure 2.4B, even a small change in $\alpha$ is enough to produce significant changes in the resulting residuals. The RMS residual from the monoexponential fit is three times greater than that of the stretched exponential, illustrating that the added complexity results in significantly improved modeling of the data. In addition, the peak in the posterior probability density for the $R_1$ relaxation rate constant (Figure 2.4C) for the monoexponential ($R_1 = 0.4157$ $s^{-1}$) is shifted with respect to the peak of the distribution corresponding to the stretched exponential ($R_1 = 0.4197$ $s^{-1}$). This shift is significant enough that the distributions are well resolved, demonstrating that the choice of model does affect the accuracy of parameter estimation. (If only the relative differences in parameter values between tissue types, and not their true values, are important, this introduction of bias into parameter estimation may not matter.) Thus, when attempting to quantify $R_1$ accurately and precisely, model selection is necessary. When applied to a cohort of competing signal models, Bayesian model selection can provide: (i) an avenue to make quantitative biophysical inferences and (ii) a check against over-interpretation/over-parameterization of data. Of the five models we tested, the biexponential and stretched exponential models best represent the full TI datasets and the truncated datasets, respectively. However, systematic smooth oscillations in the residuals demonstrate that these functions do not fully model the data.

The existence of these systemic oscillations, even from the favored choice among our cohort of five signal models, is not a limitation of Bayesian-based model selection but, instead, is a limitation in the ability of the models used to represent the data. As described previously, even when a more complex exponential model --a triexponential model – was included, the biexponential model was still favored. This means the increase in parameterization did not result in a sufficiently decreased residual so as to favor the more complex model. To further reduce or eliminate those systemic oscillations, other signal models will have to be explored. A model that accounts for exchange between water-relaxation-populations, such as the Bloch-McConnell exchange model [18] or perhaps a multi-modal $R_1$ distribution model, such as those based on the work of Brownstein and Tarr [19, 20] may result in a substantially improved data representation.

To select the “best” (most probable) model, $M_{opt}$, from the cohort of competing models, M = $\{M_i\}$, the Bayesian-based algorithm seeks the highest valued posterior probability *P(M|DI)*, Eq. [7]. Assuming relatively uninformative model prior probabilities, *P(M|I)*, as employed herein, *P(M|DI)* is principally determined by the marginal direct probability for the data, *P(D|MI)*, given model M, which is inversely proportional to the aggregate calculated uncertainty over all parameters (more formally, integration over all probability distributions); see Eq. [8] for an example. A more complex model must result in a significant decrease in the aggregate uncertainty to be favored over a model with fewer free parameters, a manifestation of Occam’s razor. Examples of this are given by the modeling residuals described in Results, as well as the RMS residual values for the favored and monoexponential models shown in Table 2.1.

Often, experiments are acquisition-time- or signal-to-noise-limited. To better understand the effect of such limitations, the data corresponding to the xBSA slow relaxation component were modified. To mimic time constraints, the xBSA datasets with 51 TIs were truncated to reduce the sampling density within each dataset. Collecting data with all 51 TI values, which requires 20 or more minutes, represents the case of no significant time constraints, as in, for example, the study of *ex vivo* tissue samples. 26 TIs, requiring perhaps 10 minutes of data collection, represents a typical small-animal scan. Finally, the relaxation experiment employing only 7 TIs, represents a short data-collection period, as might be required for a clinical scan. For each of these cases, Bayesian-based model selection was performed jointly on twelve datasets and, in each case, the stretched exponential model was heavily favored.

The effect of decreasing sampling density, mimicking increasingly limited data-acquisition time, on the Bayesian-estimated posterior probability distribution for the decay-rate constant is illustrated in Figure 2.5A. As the number of TIs decreases, the posterior probability distribution becomes broader, demonstrating that certainty in the parameter estimation decreases with decreasing sampling density. We note that as the original xBSA datasets were acquired under very high SNR conditions and the preferred model, the stretched exponential, has only four parameters, the Bayesian-estimated posterior probability distributions are narrow, even for the case of 7 TIs.

To see this effect more clearly, Gaussian-distributed noise was added to the twelve xBSA datasets with 51 TIs to reduce the SNR to the intermediate case of SNR = 100, which can be achieved in a single voxel *in vivo* MR spectroscopy (MRS) relaxation experiment, and subsequently truncated to reduce the sampling density to 26 TIs and further 7 TIs.

For each of these cases, Bayesian-based model selection was performed jointly on twelve datasets and, in each case, the stretched exponential model was heavily favored. The resulting posterior probability distributions for the rate constants are shown in Figure 2.5B. We see the same general trend as that of the high SNR case (Figure 2.5A), broadening of the distributions as the sampling density decreases. Here, the effect is exacerbated by the decreased SNR (SNR = 600 *vs.* 100).

To simulate the case in which signal-to-noise is the limiting factor, Gaussian-distributed noise was added to the 51 TI datasets so that the SNR decreased from its original value of 600, to an intermediate value of 100, and further down to 25, typical of an *in vivo* MR imaging relaxation experiment. For the SNR = 25 case, the monoexponential model was heavily favored, whereas the stretched exponential model was heavily favored for both the cases of SNR = 600 and SNR = 100. The resulting Bayesian-estimated posterior probability distributions for the decay-rate constant and alpha parameters from the stretched exponential model are shown in Figures 2.6A and 2.6B, respectively. Figure 2.6C shows the resulting parameter estimates when the monoexponential model is used.

As the SNR decreased, the resulting posterior probability distributions become much broader, with the standard deviation for the $R_1$ estimation increasing by a factor of approximately 5. It is important to note that in this case, the standard deviation is not a measure of the spread of measured rate constants within our population. Here, the standard deviation is a Bayesian-derived measure of the uncertainty in the calculated parameter estimate. The added noise can be thought of as uncertainty within the data, which is propagated through, and reflected in, the increased uncertainty of the parameter estimates. This means that with increased noise, the precision of the parameter estimation decreases.

There is also a shift in the peak of the posterior probability distribution for the case of SNR = 25 with respect to the high and intermediate SNR cases (Figures 2.6A & 2.6B, Table 2.3). This can be explained by the change in the favored model, as the result of fitting the data with a different model introduces bias into the parameter estimation. While the variations in the parameter estimates (shifts in positions of the peaks of the posterior probability distributions) and uncertainties therein (changes in widths of the posterior probability distributions) are modest as SNR and sampling density are degraded, the trends are informative and consistent with what would be observed under more severe degradation of data quality.

An important consideration regarding this result is that, while a SNR = 25 can be considered low, the joint analysis of three (*in vivo*) and twelve (xBSA) replicate datasets, each with different additive noise elements but the same noise power, greatly increases the statistical power of Bayesian inference. From a frequentist point of view, assuming all dataset members are of equal quality (i.e., equally informative), the full dataset SNR is proportional to the square root of the number of replicate members in the dataset. Thus, while each of the twelve replicate members of the xBSA dataset had SNR = 25, the full dataset can be considered to have a SNR = 25 x (12)$_{1/2}$ = 87. Thus, even under conditions in which each xBSA dataset member had SNR = 25, the joint analysis of twelve replicate members yielded quite precise parameter estimates.

The tissue-mimicking xBSA phantom possesses both a narrow water $_1$H resonance, characteristic of a small, highly mobile, randomly reorienting molecule and a very broad crosslinked-protein $_1$H resonance feature, characteristic of semi-solid macromolecules. A short, 180-degree pulse will invert magnetization over a broad range of resonance frequencies (e.g., 20 μs → ~5,000 Hz), thus, to first approximation, inverting both the water and the crosslinked protein $_1$H magnetization. In this case, $_1$H magnetization transfer between water and protein pools does not act as an efficient longitudinal relaxation mechanism for water. A long, 180-degree pulse will invert magnetization over a narrow range of resonance frequencies (e.g., 1.6 ms → ~600 Hz), thus, to first approximation, inverting the water $_1$H magnetization while leaving the majority of the protein $_1$H magnetization in the thermally equilibrated (Boltzmann) polarized state. In this case, $_1$H magnetization transfer between water and protein pools acts as an efficient longitudinal relaxation mechanism for water. The data summarized in Table 2.4 bear this out. In the case of short (broadband) RF pulses, the fractional amplitude of the fast relaxation component, which reflects the population of water molecules that relax via magnetization transfer with the crosslinked protein pool, is near zero (~3%), but increases markedly to 20% in the case of long (narrowband) RF pulses. Long RF pulses (1 - 4 ms) are typical of *in vivo* MRI protocols and, thus, magnetization transfer effects will manifest significantly in longitudinal relaxation experiments *in vivo* [10]**.**

In conclusion, we have shown that xBSA displays similar longitudinal relaxation characteristics to that of *in vivo* brain tissue, allowing for future characterization of the effects of likely important endogenous modifiers of $R_1$ in tissue, such as $pO_2$, pH, and protein content. We have also shown that the MFIR pulse sequence yields very similar results to the standard IR pulse sequence but that, in the presence $_1$H magnetization transfer between water and cross-linked protein, pulse widths can have a substantial effect upon relaxation characteristics and, thus, parameter estimates. Finally, we have shown the utility of Bayesian-based model selection (and related parameter estimation) for selecting amongst a cohort of competing signal models. As data become less informative (e.g., sparser, lower SNR), simpler models (e.g., those with fewer parameters) are preferred, in the Bayesian sense of being more probable, given the data and the prior information.

## 2.5 Acknowledgments

Research supported, in part, by the McDonnell Center for Cellular and Molecular Neurobiology (JA) and National Institute of Health grants: P50 CA094056, R01 HD086323, 5T32 EB014855, and the Small Animal Cancer Imaging Shared Resource of the Alvin J. Siteman Cancer Center (P30 CA091842). The content is solely the responsibility of the authors and does not necessarily represent the official views of the NIH.

## 2.6 References

1. Cox, R.T., *The Algebra of Probable Inference*. 1961, Baltimore, MD: The John Hopkins Press.
2. Bretthorst, E.T.J.G.L., *Probability Theory: The Logic of Science.* 2003.
3. Jaynes, E.T., *Papers on Probability, Statistics and Statistical Physics*. 1 ed. Synthese Library. 1989: Springer Netherlands. 458.
4. Cheng, H.L.M., et al., *Practical medical applications of quantitative MR relaxometry.* Journal of Magnetic Resonance Imaging, 2012. 36(4): p. 805-824.

5. O'Connor, J.P.B., et al., *Preliminary Study of Oxygen-Enhanced Longitudinal Relaxation in Mri: A Potential Novel Biomarker of Oxygenation Changes in Solid Tumors.* International Journal of Radiation Oncology Biology Physics, 2009. 75(4): p. 1209-1215.
6. O'Connor, J.P.B., et al., *Comparison of Normal Tissue R-1 and R-2* Modulation by Oxygen and Carbogen.* Magnetic Resonance in Medicine, 2009. 61(1): p. 75-83.
7. Matsumoto, K., et al., *MR assessment of changes of tumor in response to hyperbaric oxygen treatment.* Magnetic Resonance in Medicine, 2006. 56(2): p. 240-246.
8. Koenig, S.H., R.D. Brown, 3rd, and R. Ugolini, *Magnetization transfer in cross-linked bovine serum albumin solutions at 200 MHz: a model for tissue.* Magn Reson Med, 1993. 29(3): p. 311-6.
9. Henkelman, R.M., G.J. Stanisz, and S.J. Graham, *Magnetization transfer in MRI: a review.* NMR Biomed, 2001. 14(2): p. 57-64.
10. Prantner, A.M., et al., *Magnetization transfer induced biexponential longitudinal relaxation.* Magnetic Resonance in Medicine, 2008. 60(3): p. 555-563.
11. Wolff, S.D. and R.S. Balaban, *Magnetization transfer contrast (MTC) and tissue water proton relaxation in vivo.* Magn Reson Med, 1989. 10(1): p. 135-44.
12. Sass, M. and D. Ziessow, *Error Analysis for Optimized Inversion Recovery Spin-Lattice Relaxation Measurements.* Journal of Magnetic Resonance, 1977. 25(2): p. 263-276.
13. Moore, W.S. and T. Yalcin, *Experimental Measurement of Exponential Time Constants in Presence of Noise.* Journal of Magnetic Resonance, 1973. 11(1): p. 50-57.
14. Kroeker, R.M. and R.M. Henkelman, *Analysis of Biological Nmr Relaxation Data with Continuous Distributions of Relaxation-Times.* Journal of Magnetic Resonance, 1986. 69(2): p. 218-235.
15. Yablonskiy, D.A. and A.L. Sukstanskii, *Theoretical models of the diffusion weighted MR signal.* Nmr in Biomedicine, 2010. 23(7): p. 661-681.
16. Gupta, R.K., et al., *A Modified Fast Inversion-Recovery Technique for Spin-Lattice Relaxation Measurements.* Journal of Magnetic Resonance, 1980. 38(3): p. 447-452.
17. Bretthorst, G.L., *How accurately can parameters from exponential models be estimated? A Bayesian view.* Concepts in Magnetic Resonance Part A, 2005. 27a(2): p. 73-83.
18. Quirk, J.D., et al., *Equilibrium water exchange between the intra- and extracellular spaces of mammalian brain.* Magnetic Resonance in Medicine, 2003. 50(3): p. 493-499.

19. Brownstein, K.R. and C.E. Tarr, *Spin-Lattice Relaxation in a System Governed by Diffusion.* Journal of Magnetic Resonance, 1977. 26(1): p. 17-24.
20. Davies, S. and K.J. Packer, *Pore-Size Distributions from Nuclear-Magnetic-Resonance Spin-Lattice Relaxation Measurements of Fluid-Saturated Porous Solids .1. Theory and Simulation.* Journal of Applied Physics, 1990. 67(6): p. 3163-3170.

# Chapter 3: Elucidating Challenges to $^1$H Longitudinal Relaxation Quantification of $pO_2$ with a Tissue Mimic[2]

## 3.1 Introduction

Molecular oxygen ($O_2$) is a vital component of energy production within the body, and impaired delivery or consumption of oxygen is a recognized hallmark of metabolic dysfunction and disease. Knowledge of tissue oxygen partial pressure ($pO_2$) can aid in diagnosis and treatment planning. For example, hypoxic tumors exhibit increased resistance to chemotherapy[1] and radiation therapy[2], and increased angiogenesis[3]. Recent studies suggest that hypoxia in adipose tissue drives insulin resistance[4]. Impaired delivery of $O_2$ is also a potential biomarker for placental dysfunction, inducing long-term adverse outcomes for both mother and fetus[5, 6].

Robust methods for the non-invasive quantification of tissue $pO_2$ are lacking. Optical imaging techniques are sensitive to blood oxy- and deoxy-hemoglobin levels[7], which can be modeled to yield, for example, the tissue metabolic rate of oxygen consumption[8] and hemoglobin oxygen saturation[9-11]. Optical imaging has limited depth of penetration, however, typically on the order of a few millimeters to a centimeter. Positron Emission Tomography (PET) utilizes hypoxia-sensitive radiotracers to detect hypoxic

---

[2] This chapter largely reflects a manuscript that has been submitted to Magnetic Resonance in Medicine and is under revision, with minor additions relevant to the thesis.
(Kelsey Meinerz, Scott C Beeman, James D Quirk, G Larry Bretthorst, Joel R Garbow, and Joseph JH Ackerman).

cells[12-14]. However, PET spatial resolution is typically a millimeter or larger and requires administration of radioactive isotopes.

Magnetic Resonance (MR) techniques are non-invasive, can probe the entire body, and provide sub-millimeter spatial resolution. Blood-oxygen-level dependent (BOLD) MR contrast results from alterations in the magnetic susceptibility of blood arising from changes in the oxy-hemoglobin to deoxy-hemoglobin ratio[15]. An increase in the relative amount of diamagnetic oxy-hemoglobin vs paramagnetic deoxy-hemoglobin decreases the susceptibility difference between intra- and extra-vascular spaces. This increases the magnetic field homogeneity over the affected tissue, leading to a decrease in the tissue water $_1$H transverse relaxation rate constants (principally $R_2$* but also $R_2$). In essence, BOLD MRI leverages the magnetic state of hemoglobin to provide endogenous contrast reflecting the oxygen content of blood. However, quantitative BOLD experiments are quite challenging[16] and BOLD results are often expressed simply as signal change relative to a baseline measurement.

A related technique, termed Tissue Oxygen Level Dependent (TOLD) MR, recognizes that $O_2$ is weakly paramagnetic and thus that dissolved oxygen affects the $_1$H longitudinal relaxation rate constant ($R_1$) of tissue water (see Ding, et al.[17], and references therein). *In principle*, $R_1$ is directly proportional to tissue $pO_2$ via the relationship

$$\mathrm{R_1}=\mathrm{R_{1,0}}+\mathrm{r_1}\cdot\mathrm{pO_2}, \qquad [1]$$

in which $R_{1,0}$ is the longitudinal relaxation rate constant in the absence of oxygen and $r_1$ is the “relaxivity” of oxygen. TOLD protocols employ inhaled gas mixtures of varying oxygen content to change tissue $pO_2$ while collecting $R_1$-weighted images. Changes in $R_1$ are interpreted as resulting from changes in tissue $pO_2$.

Knowledge of $R_{1,0}$ and $r_1$ would potentially allow for an $R_1$-based method for true quantification of $pO_2$. However, as the solubility of $O_2$ in water is limited (~1.1 mM or ~34 mg/L at 37 °C and 1 atmosphere partial pressure of 100% $O_2$[18]) and the $O_2$ magnetic relaxivity is weak (~14% that of Gd-DTPA[18, 19]), the effect of dissolved $O_2$ on tissue water relaxation is expected to be quite small[20, 21]. Indeed, we have previously reported the oxygen $r_1$ for in vivo mouse brain to be ~ $9 \times 10^{-4}$ $mmHg^{-1}s^{-1}$[22]. Thus, substantial MR measurement and analysis challenges need to be addressed to account for and/or mitigate other relaxation dependencies, e.g., blood flow[22], which compete with the direct effect of oxygen on longitudinal relaxation in vivo.

Of specific relevance to this study, longitudinal relaxation of tissue water is better approximated *in practice* by a biexponential model rather than a monoexponential model[23-25]. This reflects, to first approximation, the presence of two *apparent* distinct populations of $^1H$ spins. The rapidly relaxing population, characterized by rate constant $R_{1,fast}$ and fraction F, describes the minority population of water molecules that relax quickly via magnetization transfer (MT) with the semi-solid macromolecular matrix. The immobile protons associated with the macromolecular matrix have very large $R_2$ values (very short $T_2$; < 1 ms) such that direct detection via MR is unfeasible[26]. However, through either direct chemical exchange, where the hydrogen nuclei themselves are exchanged, or indirect dipole-dipole cross-relaxation, where the spin states between pairs of nuclei are exchanged, magnetization is transferred and the water protons are aided in their return to thermal equilibrium[27]. This MT effect is likely driven by direct chemical exchange with solvent (water) accessible amides on the surface of proteins. The slowly relaxing population, characterized by rate constant $R_{1,slow}$ and fraction 1-F, describes the majority population of water molecules. This slowly relaxing majority population is referred to herein as “non-MT” although it is recognized that MT through mechanisms other than rapid chemical exchange can affect relaxation at longer timescales[28]. The biexponential function can be written as

$$M_z(t)= A+B\left[F^* \exp\left(-R_{1,fast}{}^*t\right)+(1-F)^* \exp\left(-R_{1,slow}{}^*t\right)\right]. \qquad [2]$$

in which *A* is a constant representing the signal intensity at equilibrium (t = ∞) and *A* + *B* is the signal intensity at t = 0. Since the relaxivity of $O_2$ is small and MT dominates the $R_{1,fast}$ spin population, we expect $R_{1,fast}$ will be relatively insensitive to oxygen concentration. Indeed, data acquired on brain and muscle in mouse in vivo show that, while $R_{1,fast}$ is insensitive to $pO_2$ changes (Figure 3.1, B & E), $R_{1,slow}$ is linearly dependent on $pO_2$ (Figure 3.1, A & D). Therefore, the relationship from eq.[1] becomes

$$R_{1,slow}=R_{1,0,slow}+r_{1,slow}{}^*pO_2, \qquad [3]$$

where $R_{1,0,slow}$ is the background relaxation rate constant describing the slowly relaxing component in the absence of dissolved tissue oxygen, and $r_{1,slow}$ is the relaxivity of oxygen pertaining to the slow component.

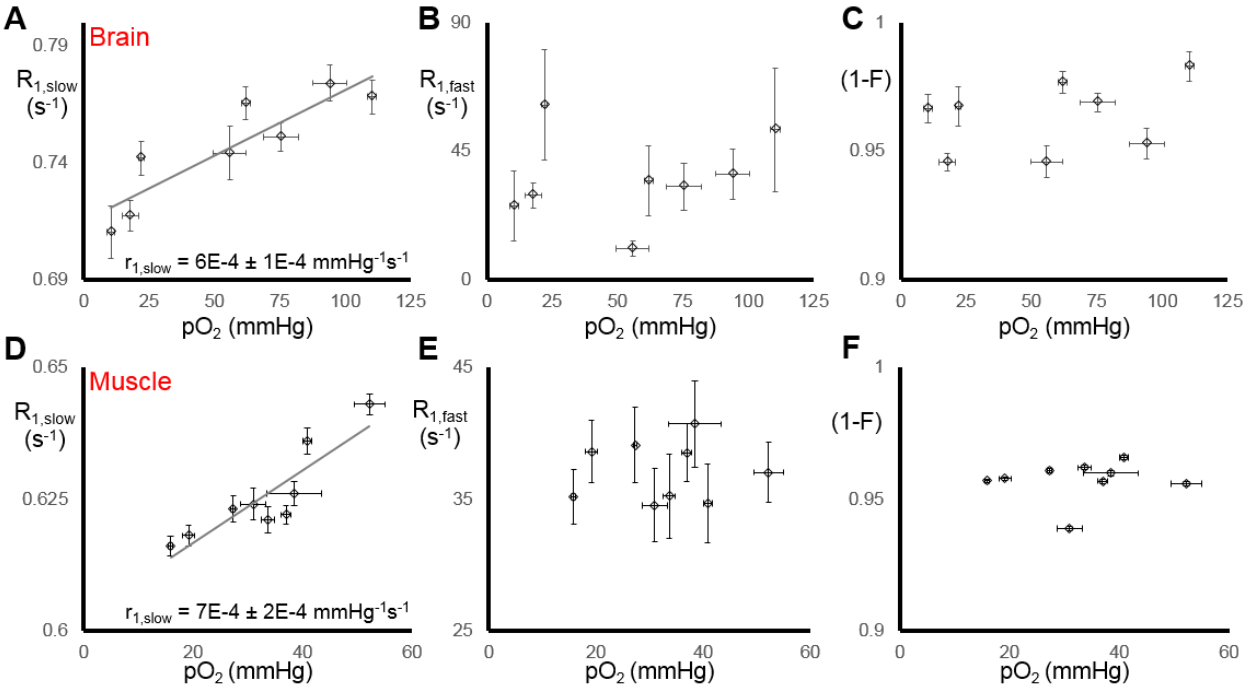

**Figure 3.1. Biexponential Modeling of Longitudinal Relaxation in Vivo vs Tissue $pO_2$ in the Mouse. A)** $R_{1,slow}$, **B)** $R_{1,fast}$, and **C)** (1-F) as a function of $pO_2$ in the thalamus and **D)** $R_{1,slow}$, **E)** $R_{1,fast}$, and **F)** (1-F) as a function of $pO_2$ in the gastrocnemius muscle. Relaxation data were collected with the voxel placed directly beneath the OxyLite® probe tip and tissue $pO_2$ was modulated by administering varying breathing gas mixtures of $O_2$ and $N_2$. All animal experiments were approved by the Washington University Institutional Animal Care and Use Committee. Each point is the result of a single PRESS-IR experiment as described previously[24] at 4.7 T, selecting a $(2\ mm)^3$ voxel, with 64 TIs ranging from 0.0075 s to 6 s, echo time (TE) of 14 ms, and a relaxation delay of 4 s (total scan time 9 min 4 s). Relaxation data were fit to a biexponential model using Bayesian probability theory-based methods[29]. Vertical error bars show ± a calculated standard deviation, reflecting the uncertainty in the parameter estimation. Horizontal error bars show ± a standard deviation of the directly measured $pO_2$ values in the tissue over the course of each PRESS-IR experiment. The relaxivity values for $R_{1,slow}$ vs $pO_2$ were determined via the Errors in Variables package in the Bayesian analysis toolbox[30] and are inlaid in **A)** and **D)**.

In addition to blood flow, physiologic parameters such as temperature, pH, and protein concentration also likely affect $R_{1,slow}$, thereby confounding quantitative measurements of

$pO_2$. To understand the magnitude of these effects, cross-linked bovine serum albumin (xBSA) was employed as an experimentally tractable phantom that mimics relaxation in tissue[23, 24, 31]. Cross-linked bovine serum albumin exhibits a substantial MT effect such that the longitudinal relaxation is better modeled as biexponential vs monoexponential (Figure 3.2). As an in vitro tissue surrogate, its pH, temperature, and protein content can be varied. Herein, we use xBSA phantoms to investigate and quantify the relationship between $R_1$ and $pO_2$, and investigate the effects of potential physiologic confounds on an $R_1$-based $pO_2$ measurement.

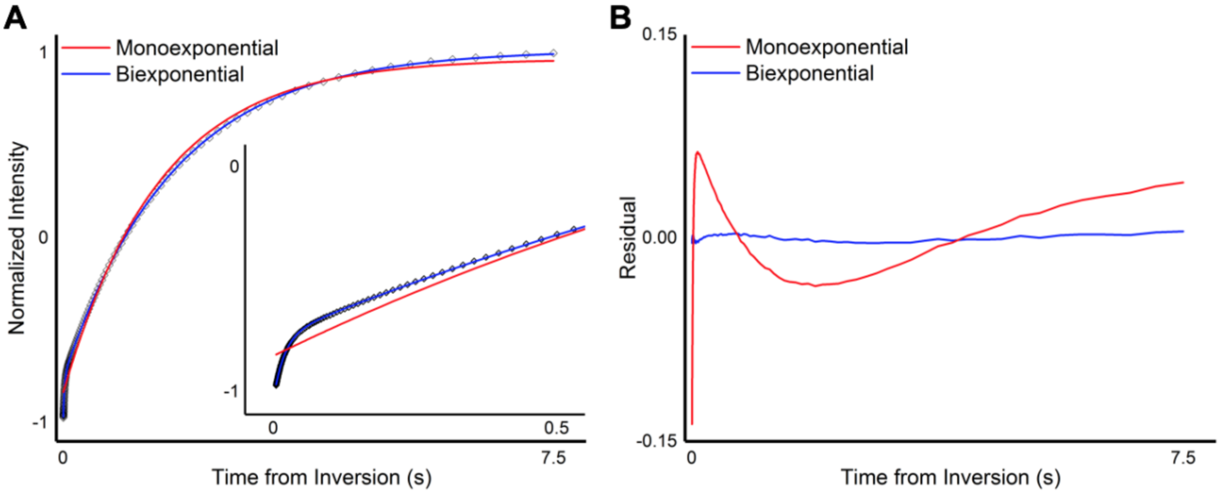

**Figure 3.2. Longitudinal Relaxation in xBSA is Biexponential. A)** Representative 128 TI relaxation time dataset (open diamonds) from the xBSA phantom, fit with the heavily favored biexponential model (blue line) and the monoexponential model (red line). Early time points are inlaid to show where the monoexponential model deviates most significantly. **B)** Resulting residual amplitudes from fitting with both models. The biexponential fit has a normalized root mean square (RMS) residual of 0.002, while the monoexponential fit has a resulting RMS residual of 0.686.

# 3.2 Methods

## 3.2.1 Phantom Preparation and Data Acquisition

xBSA samples were prepared by dissolving lyophilized bovine serum albumin (BSA) powder (Sigma-Aldrich, St. Louis, MO, USA) in phosphate buffered saline (PBS, pH 7.4) solution. The solution was prepared to be 30% (w/v) BSA for all experiments, except those varying protein concentration. Samples were cross-linked using 2.5% (v/v) of a 50% glutaraldehyde solution (Electron Microscopy Sciences, Hatfield, PA, USA) in a 35-mm diameter polystyrene petri dish. Following the addition of glutaraldehyde, samples were stirred by hand with a spatula for approximately one minute, covered in parafilm, and placed into a sealed container in the refrigerator (~4°C) for five days. Cylindrical pieces of xBSA were then cored out and placed into a 5-mm, susceptibility-matched, NMR microtube (Shigemi Inc, Allison Park, PA, USA) (Figure 3.3, A & B), sealed with parafilm, and maintained at 37°C for ~24 hours prior to data acquisition. Unless otherwise noted, all MR experiments were performed with samples maintained at 37°C.

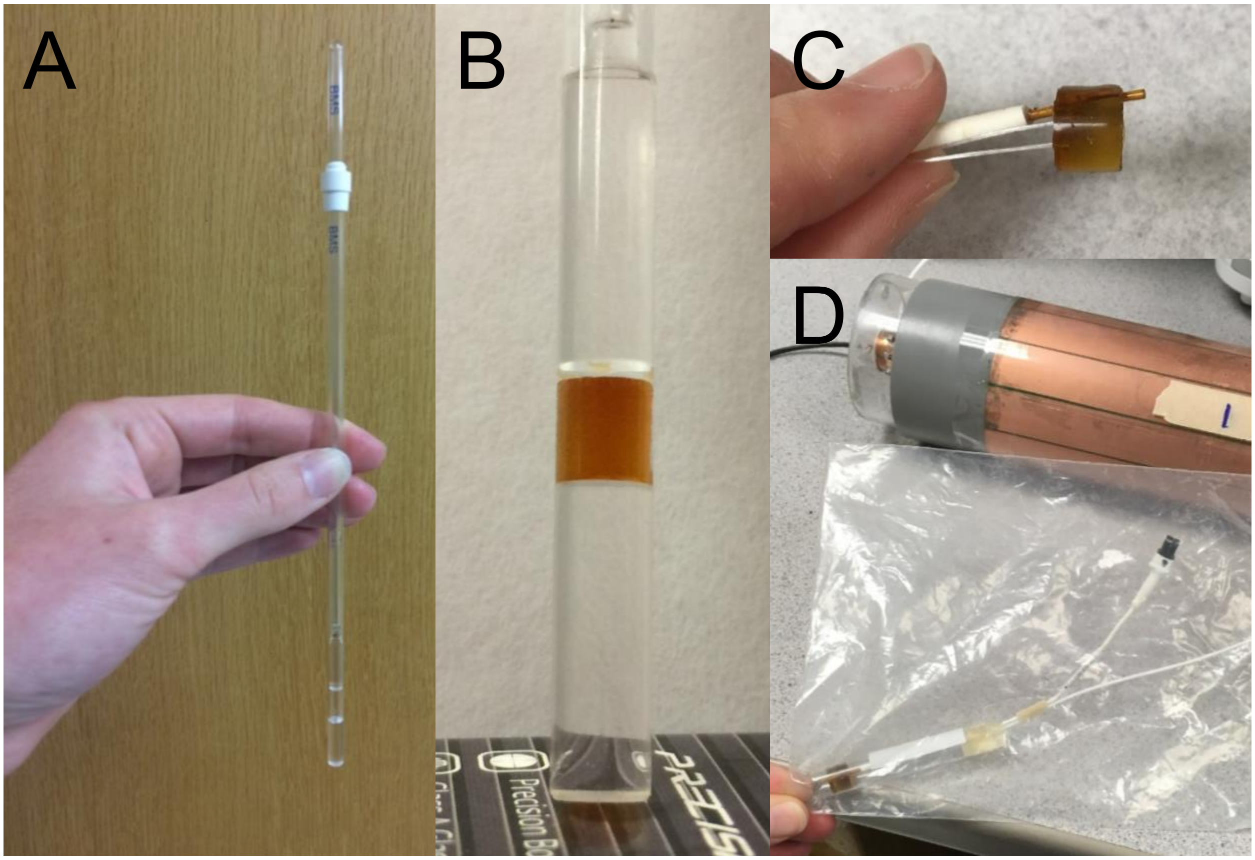

**Figure 3.3. xBSA sample preparation. A)** Full Shigemi tube with susceptibility matched insert and **B)** zoomed-in image of Shigemi tube combination with cylindrical piece of xBSA sample inside, for temperature, pH, and protein concentration modulation experiments. **C)** Cylindrical xBSA sample with OxyLite® and temperature sensor embedded within it for $pO_2$ modulation experiment and **D)** xBSA sample and sensors placed in glass vial and plastic bag prior to placement within the RF coil.

In experiments examining the dependence of xBSA relaxation on temperature, the sample temperature was varied by initially equilibrating the samples at 40°C overnight using a heating block and acquiring data using an NMR probe maintained at 40°C. This overnight heating was dual purpose: 1) xBSA samples exhibited color and opacity changes following crosslinking and heating and 2) was a matter of convenience. The color and opacity changes occurred within a few hours of heating and it was unknown if the root of these changes would also affect the MR results, driving the decision to wait until the samples had stabilized. Following data acquisition at 40°C, the probe temperature was lowered to 37°C and samples were allowed to equilibrate prior to data collection at that temperature. The probe temperature was then lowered to 34°C, followed by another equilibration period prior to data acquisition.

In experiments examining the dependence of xBSA relaxation on protein content, the sample protein concentration was varied by initially dissolving lyophilized BSA powder into PBS to create a solution that was 40% protein (w/v) and subsequently diluting this sample to create solutions that were 30%, 20%, and 10% protein (w/v). Crosslinking and subsequent sample preparation were as described above.

In experiments examining the dependence of xBSA relaxation on pH, the sample pH was varied through the addition of either sodium hydroxide (NaOH) or hydrochloric acid (HCl) to the 30% BSA solution before crosslinking. The pH of the solution prior to crosslinking was measured using an Orion PerpHecT ROSS Comb Micro pH electrode probe (Thermo Fischer Scientific Inc, Waltham, MA, USA). Crosslinking and subsequent sample preparation were as described above. The pH of the crosslinked material was measured by two different methods: (i) the electrode probe used in solution and (ii) NMR via $_{31}$P measurements of the pH sensitive inorganic phosphate resonance[32]. The two methods provided similar results; herein the reported values resulted from measurements via the pH electrode.

In experiments examining the dependence of xBSA relaxation on pO$_2$, the sample pO$_2$ was varied by blowing humidified O$_2$ gas over a small xBSA cylindrical sample placed in an open glass vial contained in a partially sealed plastic bag under positive pressure (Figure 3.3, C & D). Sample $pO_2$ was measured in real time via an implantable OxyLite® (Oxford Optronix, Abingdon, Oxford, UK) $O_2$-sensing optical microprobe at a rate of one measurement per minute. Reported values are the averages of all measurements performed over the course of each relaxation experiment and the error bars reflect the calculated standard deviation of those values.

Agar gel samples were prepared by initially dissolving agar powder (Sigma-Aldrich, St. Louis, MO, USA) in PBS at a concentration of 0.6% (w/v) agar. The agar solution was heated in a boiling water bath, with occasional stirring, until the solution became transparent. The solution was then removed from the bath, poured into polystyrene weigh boats (Thermo Fischer Scientific Inc, Waltham, MA, USA) and allowed to cool overnight at room temperature. Modulation of sample $pO_2$ was varied by blowing humidified gas mixtures over a small sample of this agar gel in an open glass vial contained in a partially sealed plastic bag under positive pressure. The humidified gas was created by combining $N_2$ gas, $O_2$ gas, and medical air (~20% $O_2$) via a gas mixer (Matheson Tri-Gas, Irving, TX, USA) and bubbling the subsequent gas mixture through a sealed flask of water. Sample $pO_2$ was monitored in real time as stated above.

$_1$H NMR relaxation experiments were performed on either (i) a 500-MHz (11.74 T) Agilent (Agilent Technologies, Santa Clara, CA, USA) high-resolution (“analytical”) NMR spectrometer in a standard 5-mm RF probe or (ii) a 11.74 T small-animal Agilent MRI system using a 1.6 cm ID birdcage coil (Stark Contrast MRI Coils Research, Erlangen, Germany). The former instrument was employed to quantify the relaxation dependence upon temperature, pH, and protein concentration while the latter was employed to quantify the relaxation dependence upon $pO_2$. Data acquisition on the analytical NMR spectrometer employed a Modified Fast Inversion Recovery (MFIR) pulse sequence[33] with acquisition parameters: 10,000 Hz bandwidth, 2,500 complex data points, water $_1$H linewidth ~100 Hz, 128 exponentially spaced inversion delay times (TI) ranging from 5 ms to 7.5 s. Total repetition time (TR = W + TI), where W is the relaxation delay, was 8.5 s. Square radiofrequency (RF) pulses were employed for inversion and observation with a typical 180 degree pulse ~1400 μs (i.e., approximating the in vivo MR situation, which maximizes the MT $R_{1,fast}$ component), and five discarded acquisitions were utilized to achieve steady-state. A 1 ms crusher gradient was applied following the inversion pulse to suppress any residual transverse magnetization arising from imperfect inversion.

Data acquisition on the MRI scanner also employed the MFIR pulse sequence in combination with IR-PRESS single-voxel localization. Measurements on each sample were acquired in triplicate with a $(1.5\ \text{mm})_3$ voxel that included the tip of the OxyLite® sensor. MRS acquisition parameters were 4,000 Hz bandwidth, 2048 complex data points, water $_1$H linewidth ~100 Hz, 64 exponentially spaced TIs ranging from 5 ms to 7.5 s. Total repetition time (TR = W + TI) was 8.5 s. Optimized RF pulses were employed for inversion and observation[34], and five discarded acquisitions were utilized to achieve steady-state. A 1 ms crusher gradient was applied following the inversion pulse to suppress any residual transverse magnetization arising from imperfect inversion.

### 3.2.2 Bayesian-Based Parameter Estimation

Relaxation parameters were estimated using Bayesian probability theory-based methods, as described previously[24, 29, 30]. For these calculations, 400 parallel simulations were performed within the Markov-chain Monte Carlo algorithm to sample the posterior probabilities for the models and their associated parameters. A minimum of 400 annealing steps brought the 400 simulations into a steady-state, at which point 30 samples were drawn from each of the 400 simulations. Therefore, 12,000 parameter samples were incorporated into the posterior probability density distributions for the models and their parameters. The peak of the posterior probability distribution is the most probable parameter estimate and the uncertainty for each parameter estimate is taken as the standard deviation of the distribution.

In many cases, the results were calculated from a joint analysis of multiple replicate datasets, where some model parameters are considered common for all included datasets, while others are dataset specific. For the experiments that varied temperature, pH, and BSA concentration, in which relaxation data was obtained in triplicate for two samples from the same bulk material and relaxation data were collected in triplicate on each, all reported model parameters ($R_{1,slow}$, $R_{1,fast}$, and (1-F)) were considered common for the six replicate datasets while the initial and equilibrium magnetizations were independent for each dataset. The optimal value for each of the common parameters was that which best represented all six replicate datasets. For the experiments in which $pO_2$ was varied, each relaxation dataset was collected on a sample from a different bulk material and optimal model parameters were determined for each dataset individually due to potential variability between bulk materials. Thereafter, the resulting relaxation parameters vs $pO_2$ datasets were fit jointly with a common slope ($r_1$) but a unique intercept ($R_{1,0}$). The background relaxation rate constant ($R_{1,0}$) was allowed to vary between datasets to reflect small potential variations in bulk material preparation. For comparison, these individual datasets were also combined into a single dataset and modeled with both a common slope ($r_1$) and common intercept ($R_{1,0}$), incorporating information about the uncertainty in the relaxation parameters and the standard deviation of the $pO_2$ measurement at each point into the fit.

### 3.2.3 Data Truncation

To simulate the in vivo situation in which scan time is limited and accurate determination of the rapidly relaxing component is impractical (and likely unnecessary, vide infra), the xBSA relaxation data were truncated to include only the longer half of the TI values. Therefore, the data remaining only include those associated with the slowly relaxing component such that the shortest TI was approximately 200 ms.

## 3.3 Results

### 3.3.1 Temperature Dependence

Within the range 34 to 40 $_{o}$C (physiologic normal ± 3 $_{o}$C), both the fast and slow longitudinal relaxation rate constants depend linearly on temperature (Figure 3.4, A & B). In these figures, each data point represents the parameter estimation resulting from Bayesian joint analysis of six replicate datasets. Across this range, $R_{1,slow}$ decreases with increasing temperature with a slope of $-0.011 \pm 0.003$ °$C_{-1}s_{-1}$ and a y-intercept of $0.9 \pm 0.1$ $s_{-1}$ ($R_2 = 0.97$), while $R_{1,fast}$ increases with a slope of $0.8 \pm 0.2$ °$C_{-1}s_{-1}$ and a y-intercept of 21 ± 6 $s^{-1}$ ($R^2$ = 0.99). The fraction of the amplitude reflecting the slow component is insensitive to temperature changes (Figure 3.4C).

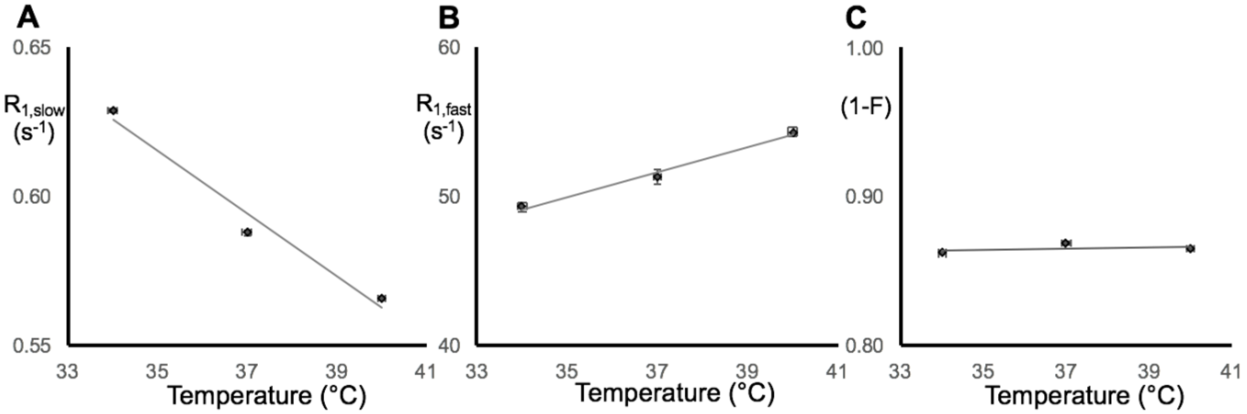

**Figure 3.4. Longitudinal Relaxation in xBSA is Temperature Dependent. A)** $R_{1,slow}$, **B)** $R_{1,fast}$, and **C)** (1-F) as a function of temperature variations about physiologic normal. Each point in the plot is the result of Bayesian joint analysis of six replicate datasets, with vertical error bars reflecting the uncertainty in the joint parameter estimation, and horizontal error bars reflecting uncertainly in the temperature maintenance of the spectrometer. $R_{1,slow}$ and $R_{1,fast}$ both depend linearly on temperature, (1-F) is unchanged with temperature. The trendline for $R_{1,slow}$ is described by the equation y = (-0.011 ± 0.003 °$C^{-1}s^{-1}$)x + (0.9 ± 0.1 $s^{-1}$) with an $R^2$ coefficient of 0.97, the trendline for $R_{1,fast}$ is y = (0.8 ± 0.2 °$C^{-1}s^{-1}$)x + (21 ± 6 $s^{-1}$) with an $R^2$ coefficient of 0.99, and the trendline for (1-F) is y = (0.001 ± 0.001 °$C^{-1}$)x + (0.84 ± 0.05) with an $R^2$ coefficient of 0.15.

## 3.3.2 Protein Content Dependence

For the range of protein concentrations studied, both the fast and slow relaxation components and the fractional amplitude of those components depend linearly on BSA concentration, i.e., protein density (Figure 3.5). In this figure, each point represents the parameter estimation resulting from Bayesian joint analysis of six replicate datasets. As the protein concentration increases, $R_{1,slow}$ increases with a slope of 0.010 ± 0.005 $(w/v)^{-1}s^{-1}$ and a y-intercept of 0.2 ± 0.1 $s^{-1}$ ($R^2$ = 0.82) and $R_{1,fast}$ increases with a slope of 0.4 ±

0.1 (w/v)$_{-1}$s$_{-1}$ and a y-intercept of 41 ± 4 s$_{-1}$ ($R_2$ = 0.89). The fraction of the total amplitude describing the slow component also shows a linear relationship with BSA concentration, decreasing with a slope of -0.0034 ± 0.0009 (w/v)$_{-1}$ and a y-intercept of 0.98 ± 0.02 ($R_2$ = 0.95).

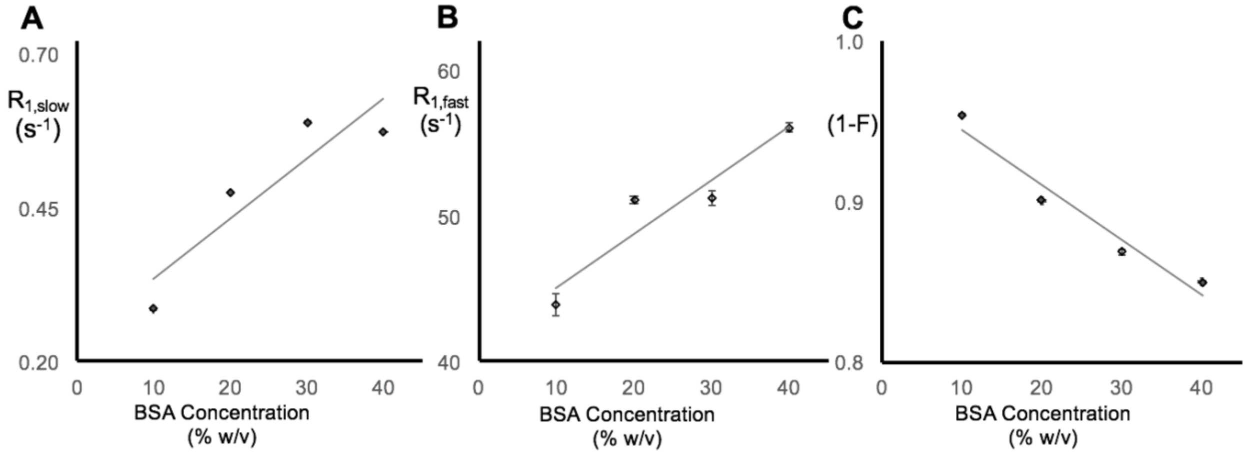

**Figure 3.5. Longitudinal Relaxation in xBSA is Protein Concentration Dependent. A)** $R_{1,slow}$, **B)** $R_{1,fast}$, and **C)** (1-F) as a function of BSA concentration. Each point in the plot results from Bayesian joint analysis of six replicate datasets, with vertical error bars reflecting the uncertainty in the parameter estimation and horizontal error bars reflecting the estimated uncertainty in concentration determination. $R_{1,slow}$, $R_{1,fast}$, and (1-F) are linearly related to macromolecule concentration. The trendline for $R_{1,slow}$ is described by the equation y = (0.010 ± 0.005 (%w/v)$_{-1}$s$_{-1}$)x + (0.2 ± 0.1 s$_{-1}$) with an $R_2$ coefficient of 0.82, the trendline for $R_{1,fast}$ is y = (0.4 ± 0.1 (%w/v)$_{-1}$s$_{-1}$)x + (41 ± 4 s$_{-1}$) with an $R_2$ coefficient of 0.89, and the trendline for (1-F) is y = (-0.0034 ± 0.0009 (%w/v)$_{-1}$)x + (0.98 ± 0.02) with an $R_2$ coefficient of 0.95.

### 3.3.3 pH Dependence

Over the range of pH 6.0 to 7.0, both the fast and slow relaxation rate constants are linearly related to pH (Figure 3.6). In this figure, each point represents the parameter estimation resulting from Bayesian joint analysis of six replicate datasets. As pH increases, $R_{1,slow}$ decreases with a slope of -0.08 ± 0.01 s$_{-1}$ and a y-intercept of 1.18 ±

0.09 $s_{-1}$ ($R_2$ = 0.97), while $R_{1,fast}$ decreases with a slope of -11 ± 4 $s_{-1}$ and a y-intercept of 130 ± 30 $s_{-1}$ ($R_2$ = 0.83). The fractional amplitude of the slow component shows a slight increase with pH with a slope of 0.03 ± 0.01 and a y-intercept of 0.68 ± 0.07 ($R_2$ = 0.85). Note that at the lowest pH value, relaxation does not fit the trend observed over the pH range of 6.0 – 7.0. At low pH, serum albumin is known to undergo reversible conformational changes that can lead to differences in the final crosslinked product [35].

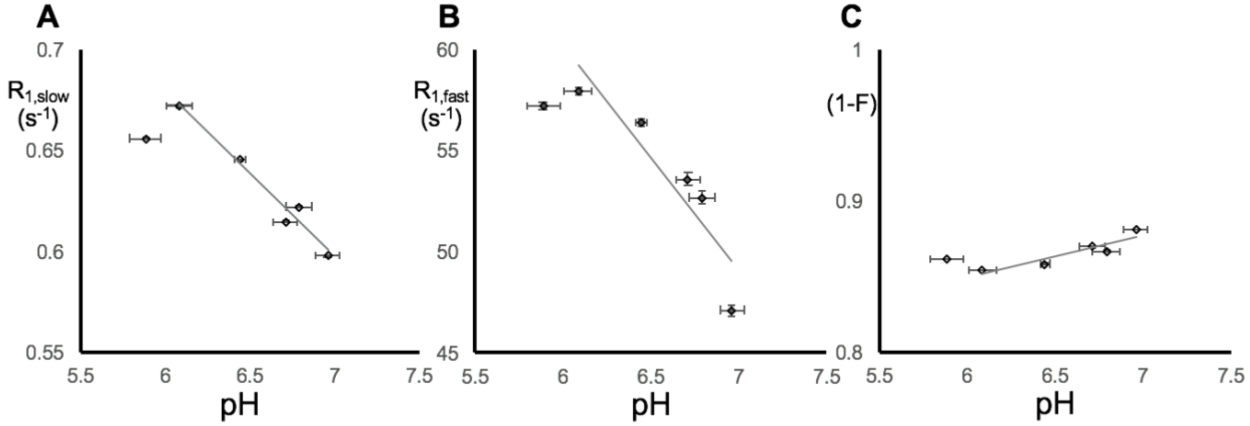

**Figure 3.6. Longitudinal Relaxation in xBSA is pH Dependent. A)** $R_{1,slow}$, **B)** $R_{1,fast}$, and **C)** (1-F) as a function of pH. Each point in the plot is the result of Bayesian joint analysis of six replicate datasets, with vertical error bars reflecting the uncertainty in the joint parameter estimation and horizontal error bars reflecting the calculated standard deviation of the measured pH. $R_{1,slow}$ and $R_{1,fast}$ are sensitive to changes in pH. The trendline for $R_{1,slow}$ is described by the equation y = (-0.08 ± 0.01 $s_{-1}$)x + (1.18 ± 0.09 $s_{-1}$) with an $R_2$ coefficient of 0.97, the trendline for $R_{1,fast}$ is y = (-11 ± 4 $s_{-1}$)x + (130 ± 30 $s_{-1}$) with an $R_2$ coefficient of 0.83, and the trendline for (1-F) is y = (0.03 ± 0.01)x + (0.68 ± 0.07) with an $R_2$ coefficient of 0.85. Note that at the lowest pH value, relaxation does not reflect the trend observed over the pH range of 6.0 – 7.0 and was therefore excluded from the linear fit. At low pH, serum albumin undergoes reversible conformational changes that can lead to differences in the final product following crosslinking[35].

### 3.3.4 pO2 Dependence

Over the range of 20 to 80 mmHg, we observed a linear relationship between $pO_2$ and $R_{1,slow}$ in xBSA tissue mimics (Figure 3.7A) and the relative insensitivity of $R_{1,fast}$ and the fractional amplitude to changes in $pO_2$ changes (Figure 3.7, B & C), as predicted. When the four experiments were analyzed jointly with a common-valued slope but unique y-intercepts, $r_{1,slow}$ was found to be $0.00212 \pm 0.00005$ $mmHg^{-1}s^{-1}$.

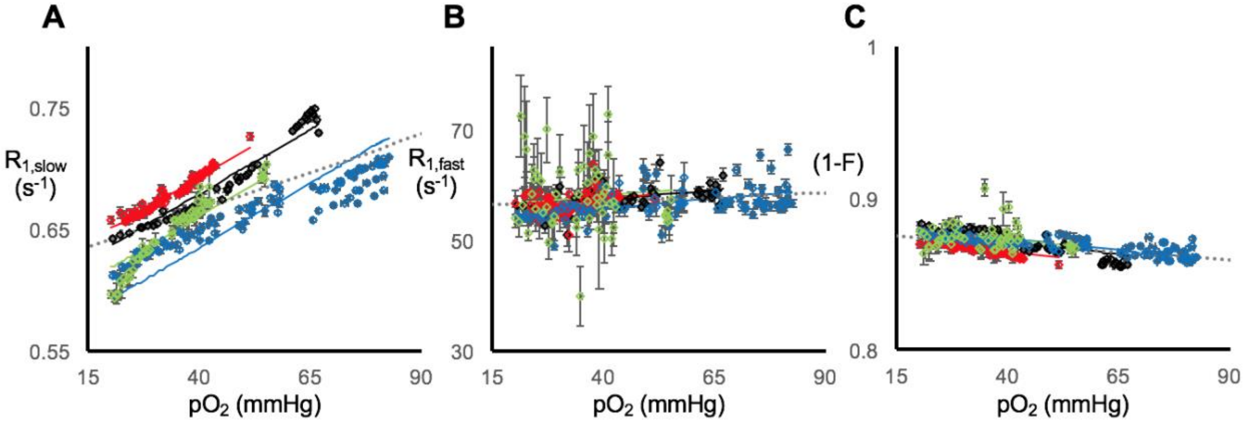

**Figure 3.7. Longitudinal Relaxation in xBSA is $pO_2$ Dependent. A)** $R_{1,slow}$, **B)** $R_{1,fast}$, and **C)** (1-F) as a function of $pO_2$ in multiple xBSA samples. Each color represents a separate sample preparation, the solid lines for each of the four colors represent the fit from a joint analysis in which the slope had a common value while the y-intercept was unique for each dataset. The dotted gray line represents the fit that results if all the data from the four experiments are combined into a single dataset and fit with a linear model. In A), the joint and combined relaxivities for the slow component are $2.12 \times 10^{-3} \pm 5 \times 10^{-5}$ $mmHg^{-1}s^{-1}$ and $1.23 \times 10^{-3} \pm 8 \times 10^{-5}$ $mmHg^{-1}s^{-1}$, respectively. In B), the joint and combined relaxivities for the fast component are $0.07 \pm 0.01$ $mmHg^{-1}s^{-1}$ and $0.03 \pm 0.01$ $mmHg^{-1}s^{-1}$, respectively. In C), the joint and combined slopes for the fractional amplitude are $-3.1 \times 10^{-4} \pm 3 \times 10^{-5}$ $mmHg^{-1}$ and $-2.2 \times 10^{-4} \pm 2 \times 10^{-5}$ $mmHg^{-1}$, respectively.

**Table 3.1. Effects of temperature, pH, protein concentration, and $pO_2$ on relaxivities and volume fraction of xBSA**

| Parameter | $r_1$ Units | $r_{1,slow}$ | $r_{1,fast}$ | (1-F) slope | Truncated $r_1$ (Monoexponential) |
|---|---|---|---|---|---|
| Temperature | $°C^{-1}s^{-1}$ | -0.011 (0.003)$_a$ | 0.8 (0.2)$_a$ | 0.001 (0.001)$_a$ [$°C^{-1}$] | -0.010 (0.003)$_a$ |
| pH [6.0-7.0] | $s^{-1}$ | -0.08 (0.01)$_a$ | -11 (4)$_a$ | 0.03 (0.01)$_a$ | -0.08 (0.02)$_a$ |
| BSA Concentration | $(\%w/v)^{-1}s^{-1}$ | 0.010 (0.005)$_a$ | 0.4 (0.1)$_a$ | -3.4E-3 (9E-4)$_a$ [$(\%w/v)^{-1}$] | 0.010 (0.005)$_a$ |
| $pO_2$ | $mmHg^{-1}s^{-1}$ | 2.12E-3 (5E-5)$_b$ | 0.07 (0.01)$_b$ | -3.1E-4 (3E-5)$_b$ [$mmHg^{-1}$] | 2.05E-3 (6E-5)$_b$ |

Values reported as mean (calculated parameter uncertainty)

[a] Resulting from Given Polynomial Order package in the Bayesian analysis toolbox.

[b] Resulting from joint linear model from the Enter Ascii Model package in the Bayesian analysis toolbox in which slope is common valued while y-intercepts are allowed to vary across datasets.

Over the range of 0 to 150 mmHg, the linear relationship between $pO_2$ and $R_1$ in agar is additionally confirmed (Figure 3.8) with considerably higher inter-sample precision compared to xBSA samples. However, this agar sample does not exhibit the full characteristics of a tissue mimic as it does not show a fast relaxing MT component (i.e., its longitudinal relaxation is monoexponential). When the three experiments were jointly analyzed with a common-valued slope but unique y-intercepts, $r_1$ in agar was found to be $0.00019 \pm 0.00006$ $mmHg^{-1}s^{-1}$.

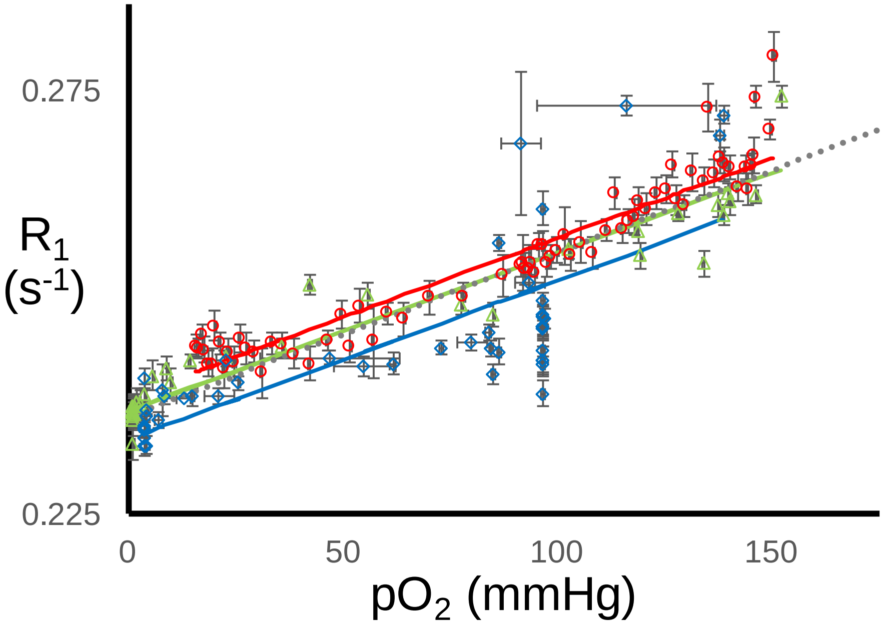

**Figure 3.8. Longitudinal Relaxation in Agar Gel is $pO_2$ Dependent.** $R_1$ as a function of $pO_2$ in multiple 0.6% (w/v) agar samples with each color denoting a separate sample preparation. The solid lines for each of the three colors represent the resulting fit from a joint analysis in which the slope had a common value, while the y-intercept was unique for each of the three datasets. The dotted gray line represents the fit that results if all the data from the three experiments are combined into a single dataset and fit with a linear model. The joint and combined relaxivities for the rate constant are 0.00019 ± 0.00006 $mmHg^{-1}s^{-1}$ and 0.00018 ± 0.00002 $mmHg^{-1}s^{-1}$, respectively.

## 3.4 Discussion

### 3.4.1 The Two-Component Relaxation (Biexponential) Model

Modeling the $^1$H longitudinal relaxation of water in xBSA as reflecting two, idealized, monoexponentially-relaxing, water populations (MT and non-MT) is, of course, an approximation. There is exchange between the two populations, although this exchange is sufficiently slow such that the two-component relaxation character is clearly evident and the two orders of magnitude difference between observed rate constants implies that the system lies close to the slow exchange limit. Therefore, the observed rate constants and amplitudes should approximate the true population amplitudes and rate constants. Additionally, exchangeable $_1$H in proteins exhibit a range of exchange rate constants (inverse of pre-exchange lifetimes)[36, 37], thus, $R_{1,fast}$ is an “apparent” or “effective” rate constant. While the fast relaxing water $_1$H MT population is likely dominated by solvent (water) accessible primary amide groups, e.g., amide moieties on the peptide surface, it is unrealistic to assume a single pre-exchange lifetime for all “fast” exchange sites. Similar considerations apply to $R_{1,slow}$; it is an apparent or effective rate constant, one that best captures the slow relaxation character of the non-MT pool.

### 3.4.2 Temperature Dependence

While 37.0 °C ± 0.5 °C is considered the normal human body temperature, interpersonal and intrapersonal temperature variations are expected due to a number of factors, including a person’s circadian rhythm[38]. xBSA phantom measurements described herein found a linear dependence of $R_{1,fast}$ (increasing) and $R_{1,slow}$ (decreasing) over a 34-40 °C temperature range.

While the effect is modest, it is consistent with a temperature-driven (i) increase in the rate of $_1$H magnetization exchange (magnetization transfer) between the semi-solid-like macromolecular matrix and highly mobile tissue water and (ii) an increase in the correlation time of the highly mobile tissue water. These data imply that modest changes in tissue temperature will affect measured values of $R_{1,slow,}$ thereby confounding quantification of tissue $pO_2$. Therefore, the accuracy of an $R_{1,slow}$-based method for quantifying $pO_2$ in vivo will depend on knowledge of tissue temperature.

In some cases, the use of minimally invasive, MR-compatible, implantable probes, i.e., fiber optic sensors, will allow measurement of tissue temperature. However, some regions of the body, i.e., brain tissue, are inaccessible via such methods. Magnetic Resonance Spectroscopy (MRS) techniques can in some cases be used to determine tissue temperature via the temperature-sensitive $_1$H chemical shift of water relative to a reference resonance. For example, in the brain, the chemical shift of water relative to NAA can provide precise measurements of tissue temperature[39].

### 3.4.3 Protein Content Dependence

As expected from the simple two-population model (MT and non-MT), both the measured $R_{1,fast}$ and $R_{1,slow}$ increase (linearly) with BSA concentration. This is consistent with (i) an increase in sites for MT as the concentration (density) of the semi-solid-like macromolecular matrix increases with an increase in protein concentration and (ii) the presence of slow exchange between the two water populations. Note that F, the population fraction of the fast relaxing (MT pool) also increases (1-F decreases) with protein concentration, consistent with the two-population model.

Protein concentration varies across tissue types in vivo[40] and will need to be considered in development of $R_{1,slow}$-based $pO_2$ quantification. Fortunately, protein concentration in various tissues has been studied, with results reported in the literature[41, 42]. For example, it has been reported that muscle cells are approximately 23% protein by weight, and actively growing cells approximately 17-26% protein by weight[40].

### 3.4.4 pH Dependence

$_1$H exchange between amide groups in proteins and solvent (water) is acid, base, and ion catalyzed. Principal sites for the chemical-exchange-driven MT that results in the fast relaxing component in the xBSA phantom are solvent accessible primary amides. Given their weak acidity, pKa > 15, a pH change from 6 to 7 is expected to produce a negligible shift in amide protonation state. However, the number of fast exchanging $_1$H sites has been shown to increase as the pH increases from 5 to 8. This has been proposed[36] to be due to subtle changes in the protein's equilibrium conformational ensemble, resulting in an increase in the population of solvent accessible $_1$H exchange sites. Nevertheless, irrespective of the underlying mechanism that changes some of the slow $_1$H exchange sites into fast $_1$H exchange sites, it is likely that a substantial fraction of these new fast exchange sites are only partially solvent accessible, compared to fast exchange sites on the protein surface. Thus, these new $_1$H exchange sites are characterized by "fast" rate constants that are somewhat slower than those of the fully solvent accessible $_1$H exchange sites. The addition of these "slower" fast exchange sites with increasing pH could cause a decrease in $R_{1,fast}$ and, due to exchange between the two relaxation populations, MT and non-MT, a decrease in $R_{1,slow}$. Amide exchange has been reported to decrease with decreases in pH[43, 44]. Therefore, as pH increases - driving faster exchange - the observed population fraction of the slow component (1-F) is increasingly weighted by the dominant slow component.

Tissue pH is known to vary across tissue types, with some evidence suggesting variability even within an extended region of similar tissue, i.e., variation across regions of the brain[45]. Additionally, studies have shown significant changes in tissue pH following incision[46], development of arthritis[47], and in tumor vs healthy tissue[48]. Precise characterization of pH in vivo is challenging, as most implantable probes are invasive and not MR-compatible. Alternatively, a variety of MR-detectable molecules, both endogenous and exogenous, have been employed to determine pH in vivo[49]. Endogenous phosphorus metabolites[32, 50] and histidine[51] have pH-dependent $^{31}P$ and $^{1}H$ chemical shifts, respectively. Administration of exogenous 3-aminopropylphosphonate (3-APP)[52] or (±) 2-imidazole-1-yl-3-ethoxycarbonyl propionic acid (IEPA)[53], also yield detectable agents with pH-dependent $^{31}P$ and $^{1}H$ chemical shifts, respectively. Recently, chemical exchange saturation transfer has been exploited to yield measures of tissue pH[49]. The use of MR to accurately determine tissue pH remains an area of active interest and will be important in quantifying $pO_2$ via tissue water $^{1}H$ relaxation.

### 3.4.5 $pO_2$ Dependence

One of the motivating aims underlying this phantom study was to elucidate the factors that would affect the use of $^{1}H$ longitudinal relaxation of tissue water to derive tissue $pO_2$. Thus, the effects of temperature, protein concentration, and pH were examined. However, central to the use of $^{1}H$ longitudinal relaxation of tissue water to derive tissue $pO_2$ is defining the $^{1}H$ water relaxivity of $O_2$ in a tissue-like environment. Toward this end, $^{1}H$ water relaxation in xBSA was measured under conditions of variable $pO_2$. The $r_{1,slow}$ determined for xBSA at 11.7 T is ~ 2 to 3 fold larger than those determined in our preliminary in vivo results at 4.7 T, possibly a manifestation of magnetic-field-strength-dependent relaxation.

Normal tissue $pO_2$, otherwise referred to as physioxia[54], has been characterized using invasive probes in various tissues, including 33.8 ± 2.6 mmHg in brain tissue, 57.6 ± 2.3

mmHg in intestinal tissue, 40.6 ± 5.4 mmHg in the liver, and 29.2 ± 1.8 mmHg in muscle tissue[55]. The range of $pO_2$ values investigated in the xBSA phantom study greatly exceeded the range of $pO_2$ values characteristic of in vivo tissue. This increased dynamic range was designed to provide improved characterization of the relationship between $pO_2$ and $R_{1,slow}$. The reduced dynamic range in vivo is an additional challenge for tissue $pO_2$ studies, further emphasizing the importance of a more precise signal model that accounts for the additional physiologic confounds explored in this work.

The difficulty in reproducibly determining the relationship between $R_{1,slow}$ and $pO_2$ in xBSA phantoms, which we speculate was due to internal variations in the individual sample preparations, led us to verify our methodology in additional media, including agar gel (Figure 3.8). A gel made with 0.6% (w/v) agar solution was chosen, as this concentration has been shown to be a good in vitro surrogate for brain tissue[56]. While the agar gel does not mimic tissue's biexponential longitudinal relaxation characteristic[57], the reproducibility of the linear relationship between $R_1$ and $pO_2$ from our measurements is greatly improved compared with the variations seen in the xBSA samples. The $r_1$ of oxygen in the agar gel is very close to reported $r_1$ values in aqueous liquids[20, 21, 58] as the concentration of agar in this gel is only 0.6% w/v and the MT effect is absent. These results confirmed that our experimental design was capable of reproducibly determining the linear relationship between $R_1$ and $pO_2$.

A number of difficulties or surprising anomalies arose from using xBSA. For instance, a change in color and opacity was noticed as the sample aged over the course of a few days, suggesting some internal changes occurring during that time. This led to the decision to age all xBSA samples for 5 days prior to experiments to improve sample consistency. Another surprising result was that the initial $pO_2$ measurement for xBSA was consistently on the order of a few mmHg or less, regardless of the time following chemical crosslinking. Additionally, the apparent diffusivity of $O_2$ through xBSA was significantly slower than that of the agar gel, taking tens of hours to increase by 60 mmHg in xBSA with pure $O_2$ gas as opposed to tens of minutes to increase by more than 100 mmHg in the agar gel with medical air (~20% $O_2$). Other works have focused on developing tissue mimics which have similar $T_1$ and $T_2$ properties as various tissues[59, 60]. However, these studies only employed a monoexponential model when determining relaxation parameters and therefore do not entirely capture the underlying biophysics. Lamellar liquid crystals[61] have been shown to display biexponential relaxation, however the composition of this sample deviates from that of in vivo tissue. Development of a phantom that mimics in vivo tissue both in composition and in relaxation characteristics remains an open field of study.

In moving from phantom to in vivo measurements of $pO_2$, the effects of blood flow provide an additional confounding factor that must be mitigated or modeled. For example, in 2D slice-selective protocols the blood-flow-driven inflow of ~ Boltzmann-equilibrium polarized $_1H$ spins from outside the slice produces an increase in the tissue's apparent $R_1$ (reduced apparent $T_1$) within the selected slice. Employing a non-slice-selective inversion pulse in inversion-recovery-type relaxation protocols substantially mitigates this effect. Further, employing weak diffusion sensitizing gradients prior to readout markedly reduces any transverse magnetization coherence within the vasculature, thus mitigating confounding signals from blood.

Additionally, the relaxation experiments in xBSA phantoms were all performed at 11.74 T and while preclinical in vivo experiments can be performed at this field strength, clinical scanners currently operate at lower fields. Clinical translation of the phantom results, as well as preclinical measurements at other field strengths, will require a careful characterization of field-strength-dependent effects for incorporation into a combined signal model. Further, in vivo experiments place constraints upon the time allotted for the $R_1$ measurement. $R_{1,slow}$ is more readily/accurately quantified than $R_{1,fast}$ and, therefore, requires significantly fewer inversion recovery delay times to determine precisely. A faster acquisition could then be utilized that contains a smaller array of TI values necessary to characterize the slowly relaxing component. Table 3.1, showing the results of using only the latter/longer half of the set of TI values collected in the analysis fit with a monoexponential, demonstrates that these truncated relaxivity results are essentially identical to the slow component relaxivities for each varied parameter.

Given the challenges in utilizing $_1$H longitudinal relaxation to quantify tissue $pO_2$ in vivo, additional applications should also be considered. Tissue engineering and in vitro organogenesis show promise as potential solutions to the worldwide shortage of donor tissues for transplantation[62, 63]. However, these techniques are not yet widely available in the clinic because methods for providing proper oxygen supply to the tissue scaffolds are still being investigated. Our $R_{1,slow}$-based technique for non-invasively monitoring tissue $pO_2$ could be used to aid in the development of best practices for oxygen delivery to facilitate proper tissue growth and development.

In conclusion, we have investigated physiologic confounds to an $R_{1,slow}$-based method for $pO_2$ quantification in tissue using xBSA phantoms. As observed with in vivo tissue, $R_1$

relaxation in these phantoms is well modeled as biexponential, with the slower component, $R_{1,slow}$, demonstrating a linear dependence on sample $pO_2$. Experiments in which temperature, BSA concentration, and pH were varied independently demonstrate clearly that $R_1$ relaxation depends upon each of these factors. Applications of $R_{1,slow}$-based methods for $pO_2$ quantification must properly account for their effects.

## 3.5 Acknowledgments

Research was supported, in part, by the McDonnell Center for Cellular and Molecular Neurobiology (JA) and National Institute of Health grants: R01 HD086323, T32 EB014855, U24 CA209837, and the Small Animal Cancer Imaging Shared Resource of the Alvin J. Siteman Cancer Center (P30 CA091842). The studies presented in this work were carried out, in part, using the Small Animal Magnetic Resonance Facility of the Washington University Mallinckrodt Institute of Radiology.

## 3.6 References

**[1]**. Tan EY, Yan M, Campo L, et al. The key hypoxia regulated gene CAIX is upregulated in basal-like breast tumours and is associated with resistance to chemotherapy. *Brit J Cancer.* 2009;100(2):405-411.10.1038/sj.bjc.6604844.

**[2]**. Gray LH, Conger AD, Ebert M, Hornsey S, Scott OCA. The Concentration of Oxygen Dissolved in Tissues at the Time of Irradiation as a Factor in Radiotherapy. *Brit J Radiol.* 1953;26(312):638-648.Doi 10.1259/0007-1285-26-312-638.

**[3]**. Hockel M, Vaupel P. Biological consequences of tumor hypoxia. *Semin Oncol.* 2001;28(2):36-41.10.1016/S0093-7754(01)90211-8.

**[4]**. Ye J. Emerging role of adipose tissue hypoxia in obesity and insulin resistance. *Int J Obesity.* 2009;33(1):54-66.10.1038/ijo.2008.229.

**[5]**. Goplerud JM, Delivoriapapadopoulos M. Physiology of the Placenta - Gas-Exchange. *Ann Clin Lab Sci.* 1985;15(4):270-278

**[6]**. Burton GJ. Oxygen, the Janus gas; its effects on human placental development and function. *J Anat.* 2009;215(1):27-35.10.1111/j.1469-7580.2008.00978.x.

**[7]**. Intes X, Chance B. Non-PET functional imaging techniques: optical. *Radiol Clin North Am.* 2005;43(1):221-234, xii.10.1016/j.rcl.2004.07.002.

**[8]**. Ghijsen M, Lentsch GR, Gioux S, et al. Quantitative real-time optical imaging of the tissue metabolic rate of oxygen consumption. *J Biomed Opt.* 2018;23(3):1-12.10.1117/1.JBO.23.3.036013.

**[9]**. Saito T, Yamaguchi H. Optical imaging of hemoglobin oxygen saturation using a small number of spectral images for endoscopic application. *J Biomed Opt.* 2015;20(12):126011.10.1117/1.JBO.20.12.126011.

**[10]**. Li Q, Lin J, Clancy NT, Elson DS. Estimation of tissue oxygen saturation from RGB images and sparse hyperspectral signals based on conditional generative adversarial network. *Int J Comput Assist Radiol Surg.* 2019;14(6):987-995.10.1007/s11548-019-01940-2.

**[11]**. Tzoumas S, Nunes A, Olefir I, et al. Eigenspectra optoacoustic tomography achieves quantitative blood oxygenation imaging deep in tissues. *Nat Commun.* 2016;7:12121.10.1038/ncomms12121.

**[12]**. Jensen RL. Brain tumor hypoxia: tumorigenesis, angiogenesis, imaging, pseudoprogression, and as a therapeutic target. *J Neurooncol.* 2009;92(3):317-335.10.1007/s11060-009-9827-2.

**[13]**. Lopci E, Grassi I, Chiti A, et al. PET radiopharmaceuticals for imaging of tumor hypoxia: a review of the evidence. *Am J Nucl Med Mol Imaging.* 2014;4(4):365-384

**[14]**. Fleming IN, Manavaki R, Blower PJ, et al. Imaging tumour hypoxia with positron emission tomography. *Br J Cancer.* 2015;112(2):238-250.10.1038/bjc.2014.610.

**[15]**. Ogawa S, Lee TM, Nayak AS, Glynn P. Oxygenation-sensitive contrast in magnetic resonance image of rodent brain at high magnetic fields. *Magn Reson Med.* 1990;14(1):68-78.10.1002/mrm.1910140108.

**[16]**. He X, Yablonskiy DA. Quantitative BOLD: mapping of human cerebral deoxygenated blood volume and oxygen extraction fraction: default state. *Magn Reson Med.* 2007;57(1):115-126.10.1002/mrm.21108.

**[17]**. Ding Y, Mason RP, McColl RW, et al. Simultaneous measurement of tissue oxygen level-dependent (TOLD) and blood oxygenation level-dependent (BOLD) effects in abdominal tissue oxygenation level studies. *J Magn Reson Imaging.* 2013;38(5):1230-1236.10.1002/jmri.24006.

**[18]**. Rumble J. *CRC Handbook of Chemistry and Physics.* 100 ed. Boca Raton, FL: CRC Press/Taylor & Francis; 2019.

**[19]**. Weis J, Nilsson S, Ericsson A, Wikstrom M, Sperber GO, Hemmingsson A. Measurement of magnetic susceptibility and MR contrast agent concentration. *Magn Reson Imaging.* 1994;12(6):859-864.10.1016/0730-725x(94)92026-5.

**[20]**. Zaharchuk G, Martin AJ, Rosenthal G, Manley GT, Dillon WP. Measurement of cerebrospinal fluid oxygen partial pressure in humans using MRI. *Magn Reson Med.* 2005;54(1):113-121.10.1002/mrm.20546.

**[21]**. Berkowitz BA, McDonald C, Ito Y, Tofts PS, Latif Z, Gross J. Measuring the human retinal oxygenation response to a hyperoxic challenge using MRI: eliminating blinking artifacts and demonstrating proof of concept. *Magn Reson Med.* 2001;46(2):412-416.10.1002/mrm.1206.

**[22]**. Beeman SC, Shui YB, Perez-Torres CJ, Engelbach JA, Ackerman JJ, Garbow JR. O2 -sensitive MRI distinguishes brain tumor versus radiation necrosis in murine models. *Magn Reson Med.* 2016;75(6):2442-2447.10.1002/mrm.25821.

**[23]**. Prantner AM, Bretthorst GL, Neil JJ, Garbow JR, Ackerman JJ. Magnetization transfer induced biexponential longitudinal relaxation. *Magn Reson Med.* 2008;60(3):555-563.10.1002/mrm.21671.

**[24]**. Meinerz K, Beeman SC, Duan C, Bretthorst GL, Garbow JR, Ackerman JJH. Bayesian Modeling of NMR Data: Quantifying Longitudinal Relaxation in Vivo, and in Vitro with a Tissue-Water-Relaxation Mimic (Crosslinked Bovine Serum Albumin). *Applied Magnetic Resonance.* 2018;49(1):3-24.10.1007/s00723-017-0964-z.

**[25]**. Gochberg DF, Gore JC. Quantitative magnetization transfer imaging via selective inversion recovery with short repetition times. *Magnetic Resonance in Medicine.* 2007;57(2):437-441.10.1002/mrm.21143.

**[26]**. Henkelman RM, Stanisz GJ, Graham SJ. Magnetization transfer in MRI: a review. *NMR Biomed.* 2001;14(2):57-64

**[27]**. Sled JG. Modelling and interpretation of magnetization transfer imaging in the brain. *Neuroimage.* 2018;182:128-135.10.1016/j.neuroimage.2017.11.065.

**[28]**. Grad J, Bryant RG. Nuclear Magnetic Cross-Relaxation Spectroscopy. *Journal of Magnetic Resonance.* 1990;90(1):1-8.Doi 10.1016/0022-2364(90)90361-C.

**[29]**. Bretthorst GL, Hutton WC, Garbow JR, Ackerman JJH. Exponential parameter estimation (in NMR) using Bayesian probability theory. *Concept Magn Reson A.* 2005;27a(2):55-63.10.1002/cmr.a.20043.

**[30]**. Quirk JD, Bretthorst GL, Garbow JR, Ackerman JJH. Magnetic resonance data modeling: The Bayesian analysis toolbox. *Concept Magn Reson A.* 2018;47a(2).ARTN e21467. 10.1002/cmr.a.21467.

**[31]**. Koenig SH, Brown RD, 3rd, Ugolini R. Magnetization transfer in cross-linked bovine serum albumin solutions at 200 MHz: a model for tissue. *Magn Reson Med.* 1993;29(3):311-316

**[32]**. Ackerman JJ, Soto GE, Spees WM, Zhu Z, Evelhoch JL. The NMR chemical shift pH measurement revisited: analysis of error and modeling of a pH dependent reference. *Magn Reson Med.* 1996;36(5):674-683

**[33]**. Gupta RK, Ferretti JA, Becker ED, Weiss GH. A Modified Fast Inversion-Recovery Technique for Spin-Lattice Relaxation Measurements. *Journal of Magnetic Resonance.* 1980;38(3):447-452.Doi 10.1016/0022-2364(80)90326-1.

**[34]**. Raddi A, Klose U. Optimized Shinnar-Le Roux RF 180 degrees pulses in fast spin-echo measurements. *J Magn Reson Imaging.* 1999;9(4):613-620.10.1002/(sici)1522-2586(199904)9:4<613::aid-jmri16>3.0.co;2-0.

**[35]**. Aoki K, Foster JF. Electrophoretic Behavior of Bovine Plasma Albumin at Low Ph. *J Am Chem Soc.* 1957;79(13):3385-3393.DOI 10.1021/ja01570a021.

**[36]**. Benson ES, Hallaway BE, Lumry RW. Deuterium-Hydrogen Exchange Analysis of Ph-Dependent Transitions in Bovine Plasma Albumin. *J Biol Chem.* 1964;239:122-129

**[37]**. Matthew JB, Richards FM. The pH dependence of hydrogen exchange in proteins. *J Biol Chem.* 1983;258(5):3039-3044

**[38]**. Mackowiak PA, Wasserman SS, Levine MM. A critical appraisal of 98.6 degrees F, the upper limit of the normal body temperature, and other legacies of Carl Reinhold August Wunderlich. *JAMA.* 1992;268(12):1578-1580

**[39]**. Zhu M, Bashir A, Ackerman JJ, Yablonskiy DA. Improved calibration technique for in vivo proton MRS thermometry for brain temperature measurement. *Magn Reson Med.* 2008;60(3):536-541.10.1002/mrm.21699.

**[40]**. Fulton AB. How crowded is the cytoplasm? *Cell.* 1982;30(2):345-347

**[41]**. Bray D. *Cell movements : from molecules to motility.* 2nd ed. New York: Garland Pub.; 2001.

**[42]**. Theillet FX, Binolfi A, Frembgen-Kesner T, et al. Physicochemical properties of cells and their effects on intrinsically disordered proteins (IDPs). *Chem Rev.* 2014;114(13):6661-6714.10.1021/cr400695p.

**[43]**. van Zijl PC, Yadav NN. Chemical exchange saturation transfer (CEST): what is in a name and what isn't? *Magn Reson Med.* 2011;65(4):927-948.10.1002/mrm.22761.

**[44]**. Mori S, Eleff SM, Pilatus U, Mori N, van Zijl PC. Proton NMR spectroscopy of solvent-saturable resonances: a new approach to study pH effects in situ. *Magn Reson Med.* 1998;40(1):36-42.10.1002/mrm.1910400105.

**[45]**. Monoranu CM, Apfelbacher M, Grunblatt E, et al. pH measurement as quality control on human post mortem brain tissue: a study of the BrainNet Europe consortium. *Neuropath Appl Neuro.* 2009;35(3):329-337.10.1111/j.1365-2990.2008.01003a.x.

**[46]**. Woo YC, Park SS, Subieta AR, Brennan TJ. Changes in tissue pH and temperature after incision indicate acidosis may contribute to postoperative pain. *Anesthesiology.* 2004;101(2):468-475.10.1097/00000542-200408000-00029.

**[47]**. Andersson SE, Lexmuller K, Johansson A, Ekstrom GM. Tissue and intracellular pH in normal periarticular soft tissue and during different phases of antigen induced arthritis in the rat. *J Rheumatol.* 1999;26(9):2018-2024

**[48]**. Gerweck LE, Seetharaman K. Cellular pH gradient in tumor versus normal tissue: potential exploitation for the treatment of cancer. *Cancer Res.* 1996;56(6):1194-1198

**[49]**. Chen LQ, Pagel MD. Evaluating pH in the Extracellular Tumor Microenvironment Using CEST MRI and Other Imaging Methods. *Adv Radiol.* 2015;2015.10.1155/2015/206405.

**[50]**. Moon RB, Richards JH. Determination of intracellular pH by 31P magnetic resonance. *J Biol Chem.* 1973;248(20):7276-7278

**[51]**. Vermathen P, Capizzano AA, Maudsley AA. Administration and (1)H MRS detection of histidine in human brain: application to in vivo pH measurement. *Magn Reson Med.* 2000;43(5):665-675.10.1002/(sici)1522-2594(200005)43:5<665::aid-mrm8>3.0.co;2-3.

**[52]**. Gillies RJ, Liu Z, Bhujwalla Z. 31P-MRS measurements of extracellular pH of tumors using 3-aminopropylphosphonate. *Am J Physiol.* 1994;267(1 Pt 1):C195-203.10.1152/ajpcell.1994.267.1.C195.

**[53]**. Garcia-Martin ML, Herigault G, Remy C, et al. Mapping extracellular pH in rat brain gliomas in vivo by 1H magnetic resonance spectroscopic imaging: comparison with maps of metabolites. *Cancer Res.* 2001;61(17):6524-6531

**[54]**. McKeown SR. Defining normoxia, physoxia and hypoxia in tumours-implications for treatment response. *Brit J Radiol.* 2014;87(1035).ARTN 20130676 10.1259/bjr.20130676.

**[55]**. Carreau A, El Hafny-Rahbi B, Matejuk A, Grillon C, Kieda C. Why is the partial oxygen pressure of human tissues a crucial parameter? Small molecules and hypoxia. *J Cell Mol Med.* 2011;15(6):1239-1253.10.1111/j.1582-4934.2011.01258.x.

**[56]**. Chen ZJ, Gillies GT, Broaddus WC, et al. A realistic brain tissue phantom for intraparenchymal infusion studies. *J Neurosurg.* 2004;101(2):314-322.DOI 10.3171/jns.2004.101.2.0314.

**[57]**. Henkelman RM, Huang X, Xiang QS, Stanisz GJ, Swanson SD, Bronskill MJ. Quantitative interpretation of magnetization transfer. *Magn Reson Med.* 1993;29(6):759-766.10.1002/mrm.1910290607.

**[58]**. Nestle N, Baumann T, Niessner R. Oxygen determination in oxygen-supersaturated drinking waters by NMR relaxometry. *Water Res.* 2003;37(14):3361-3366.10.1016/S0043-1354(03)00211-2.

**[59]**. D'Souza WD, Madsen EL, Unal O, Vigen KK, Frank GR, Thomadsen BR. Tissue mimicking materials for a multi-imaging modality prostate phantom. *Med Phys.* 2001;28(4):688-700.10.1118/1.1354998.

**[60]**. Liney GP, Tozer DJ, Turnbull LW. A simple and realistic tissue-equivalent breast phantom for MRI. *J Magn Reson Imaging.* 1999;10(6):968-971.10.1002/(sici)1522-2586(199912)10:6<968::aid-jmri9>3.0.co;2-0.

**[61]**. Malyarenko DI, Zimmermann EM, Adler J, Swanson SD. Magnetization transfer in lamellar liquid crystals. *Magn Reson Med.* 2014;72(5):1427-1434.10.1002/mrm.25034.

**[62]**. Farris AL, Rindone AN, Grayson WL. Oxygen Delivering Biomaterials for Tissue Engineering. *J Mater Chem B.* 2016;4(20):3422-3432.10.1039/C5TB02635K.

**[63]**. Griffith LG, Wu B, Cima MJ, Powers MJ, Chaignaud B, Vacanti JP. In vitro organogenesis of liver tissue. *Ann N Y Acad Sci.* 1997;831:382-397.10.1111/j.1749-6632.1997.tb52212.x.

# Chapter 4: MRI-Derived Biomarkers Assess Placental Function & Development in Mouse Models of Placental Insufficiency[3]

## 4.1 Introduction

Placental dysfunction can lead to life threatening situations for both mother[1, 2] and fetus[3-6]. Pre-eclampsia (PE), estimated to affect 2-8% of pregnancies worldwide, is the leading cause of maternal and perinatal morbidity and mortality[7, 8], and involves altered vascular development within the placenta[9]. Intrauterine growth restriction (IUGR), characterized by a fetus that is small for gestational age, is estimated to affect 3-7% of pregnancies worldwide[10], and can lead to an increased risk of perinatal mortality and morbidity[11]. There are many potential causes for IUGR, including insufficient delivery of nutrients or oxygen, infection with TORCH pathogens[12] which are able to cross the placenta, genetic predisposition, and various maternal disorders or stress factors[13]. Often, the treatment protocol for mothers diagnosed with severe PE or IUGR is early delivery, though determining optimal timing for delivery to ensure the best outcome for both fetus and mother remains a challenge[7, 11]. Establishing quantitative biomarkers of placental development and function could provide a means for determining when fetal development is no longer being properly supported, a trigger for early delivery. Magnetic

---

[3] This chapter largely reflects a manuscript that is in preparation, with minor additions relevant to the thesis.
(Kelsey Meinerz, James D Quirk, and Joel R Garbow).

resonance imaging (MRI) is a non-invasive modality for generating high-resolution, *in vivo* images having outstanding soft-tissue contrast that are sensitive to tissue microstructure and physiology. MRI is, therefore, an excellent tool for probing placental function and development during gestation.

While placental shapes and structural designs vary wildly across mammals[14], humans, many primates, and rodents have discoid hemochorial placentas with a distinct layer structure [15, 16]. With respect to the fetus, the most proximal layer, the labyrinth zone in mice and the ‘fetal placenta’ in humans, is characterized by both maternal and fetal blood supplies and is the main site of exchange between these systems[15]. The middle layer, the junctional zone in mice and the basal plate in humans, contains only maternal blood that flows in and out of the most proximal layer. The most distal layer is significantly different between mice and humans[15]. As a consequence, we focused on the two murine layers that are analogous to the human placenta, the labyrinth and junctional zones.

The strains of mice we studied typically deliver at embryonic day 19.5 (E19.5) [17] and in contrast to humans, the murine uterus is composed of two horns, each associated with an ovary[18], which is designed to accommodate large litters of fetoplacental units. Blood flow within the uterine loop is bidirectional[18] and while having multiple fetoplacental units per dam increases imaging efficiency, movement of the uterus within the abdominal cavity over time makes it challenging to uniquely track individual fetoplacental units across gestation. Techniques to non-invasively determine the order of fetoplacental units within a uterine horn via MRI exist[19], but are challenging and would have added significant time to an already lengthy imaging protocol.

Numerous murine models of abnormal pregnancy have been established, including models of PE[20, 21] and IUGR[22-24]. Interleukin 10 knock-out (IL-10 KO) mice display increased inflammatory reactions[25] and when pregnant and treated with polyinosinic-polycytidylic acid (Poly(I:C)) develop symptoms characteristic of PE[20], including hypertension and proteinuria. Herein we employed the “crowded uterine horn” model of IUGR[22] wherein super ovulation is induced *via* removal of a single ovary prior to mating. As each horn has its own cervix, the eggs released from one ovary are confined to that horn, resulting in the entire litter being located within a single horn. Blood enters the uterine horn from both the ovarian and uterine arteries and fetoplacental units located within the middle of the horn receive diminished blood flow and reduced nutrient and oxygen content, resulting in fetuses characterized by fetal growth restriction (FGR) [22]. For the purposes of this study, fetoplacental units from the middle third of the total litter in each dam were deemed IUGR.

MRI can non-invasively probe the entirety of the abdomen with sub-millimeter resolution, allowing placental volume measurements at multiple time points across gestation in the same animals. Additionally, the MRI longitudinal relaxation rate constant ($R_1$) and the effective transverse relaxation rate constant ($R_2$*) can be measured and used to infer information about the amounts of oxygen within the tissue and vasculature, respectively. As molecular oxygen ($O_2$) is weakly paramagnetic, $R_1$ is, in principle, directly proportional to local tissue $pO_2$ [26-28] and has been used as a measure of placental oxygenation/hypoxia[29, 30]. $R_2$* has been shown to be linearly proportional to the concentration of deoxyhemoglobin within the vasculature[31, 32]. Measuring these rate constants while the mother is breathing medical air (20% $O_2$) and during a gas challenge with 100% $O_2$ probes the level of placental function and its response to environmental changes.

The purpose of this study is to use MRI to non-invasively probe placental development and investigate biomarkers of placental function in late gestation for established mouse models of common placental dysfunctions.

# 4.2 Methods

## 4.2.1 Mouse Models of Placental Insufficiency

All animal experiments were approved by the Washington University Institutional Animal Care and Use Committee. An overview of the protocol for these experiments is shown in Fig. 4.1 A. Pregnant, healthy C57BL/6 dams were received E11.5 in gestation from Charles River Laboratories (Wilmington, MA, USA). Non-pregnant C57BL/6 females and males were ordered from Charles River Laboratories and bred to generate the IUGR cohort. Prior to breeding, a left hemi-ovariectomy was performed on the female mice, which were allowed a minimum of two weeks to recover before breeding. A colony of IL-10 KO mice was established with mice purchased from Jackson Laboratory (Bar Harbor, ME, USA; stock #002251)[25]. All in-house breeding was managed by the Mouse Genetics Core facility at Washington University in St Louis.

To intensify PE-like symptoms in pregnant IL-10 KO dams, each received a 2.5 mg/kg intraperitoneal (IP) injection of 1 mg/mL Poly(I:C) high molecular weight solution (InvivoGen US, San Diego, CA, USA) on days E12.5, E14.5, and E16.5. IP injections were administered carefully, restricting the needle's depth of penetration to just below the peritoneum, to avoid injury to fetoplacental units in the abdomen.

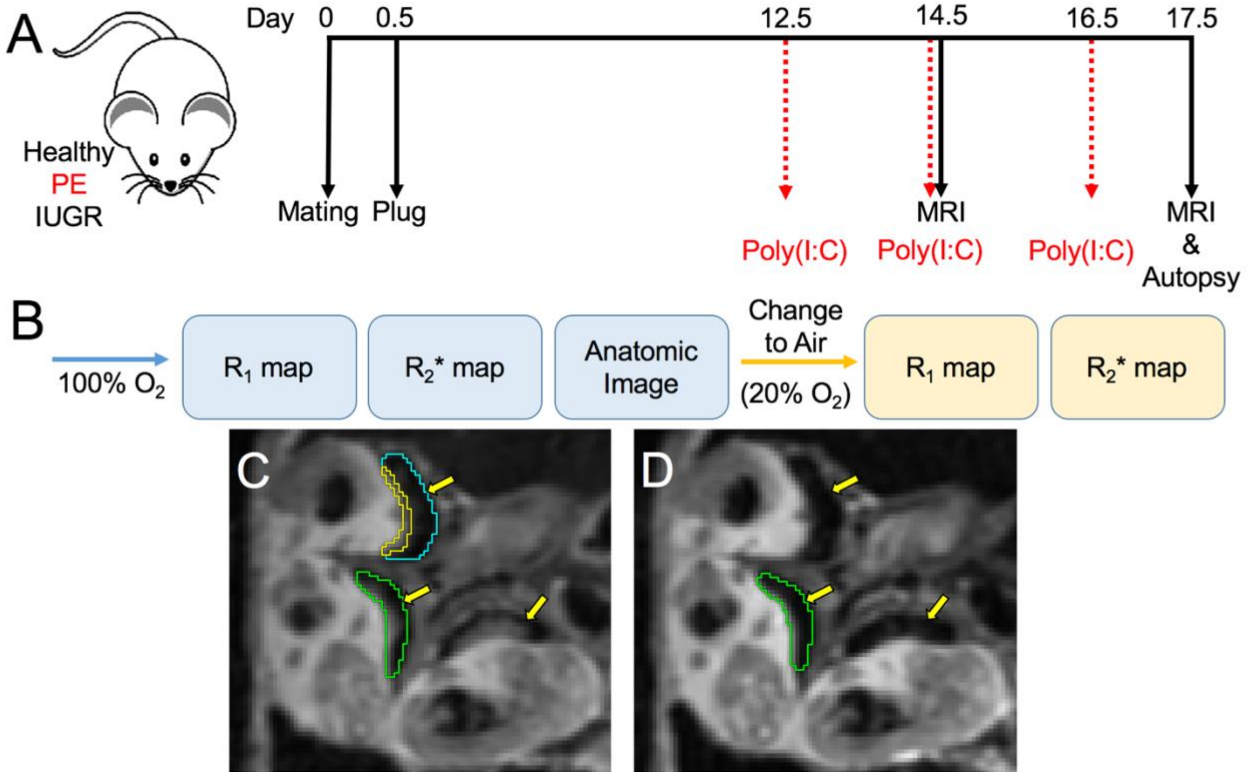

**Figure 4.1. Overview of the experimental and imaging protocols. A)** Experimental protocol: Poly(I:C) IP injections were administered only to IL-10 knockout mice (PE model). **B)** Imaging protocol: The minimum equilibration period after switching breathing gases was 2 minutes. Identical regions of $T_2$-weighted anatomic images in the same E14.5 IUGR dam breathing **C)** 100% $O_2$ and **D)** medical air (20% $O_2$). Three placentas are indicated with yellow arrows. One complete placenta is outlined in green, while a second placenta, segmented into labyrinth (yellow outline) and junctional (blue outline) zones by our automated algorithm is shown in **C).** Image contrast within the placenta between the labyrinth and junctional zones is lost when breathing medical air.

### 4.2.2 MRI Protocol and Analysis

An overview of the imaging protocol is shown in Fig. 4.1 B. MRI experiments were performed on a 11.74-T small-animal MRI system (Agilent Technologies, Santa Clara, CA, USA) using a 5-cm ID birdcage coil (Extend MR LLC, San Francisco, CA, USA) at gestational days E14.5 and E17.5. In this study, 11 Healthy dams, 14 IUGR dams, and 18 PE dams were imaged. Mice were anesthetized with isoflurane (3% for induction, 1-2% for maintenance) mixed with oxygen (1 L/min), delivered through a nose cone. Once anesthetized, animals were placed in the supine position on a custom-built imaging cradle and taped across the abdomen to restrict respiratory motion. Respiration rate and body temperature were monitored using an MR-compatible monitoring and gating system (SA Instruments, Inc., Stony Brook, NY, USA). Body temperature was maintained at 37°C via circulation of warm air and the respiration rate was maintained at ~50 breaths per minute through modulation of anesthesia. Halfway through the MRI study, the anesthesia delivery gas was switched to medical air (20% O2) and the mice were allowed to equilibrate for a minimum of two minutes prior to additional imaging.

The volumes of all placentas (5-10/mouse) were calculated by manual segmentation of respiratory-gated, $T_2$-weighted, multi-slice spin-echo images (SEMS). Each placenta was automatically divided into labyrinth and junctional zones based on the relative intensities of each voxel using Otsu's method[33]. The SEMS parameters were: time to repetition (TR) = 1500 ms; echo time (TE) = 30 ms; field of view, 4.8 x 6.4 $cm_2$; matrix, 96 x 256, zero-filled to 192 x 256 to yield in-plane resolution of 0.25 mm; 0.5 mm slice thickness; 1 average; scan time ~ 15 minutes. High resolution images were collected with a data matrix of 512 x 192, zero-filled to 512 x 384 to yield in-plane resolution of 0.125 mm. For $R_1$ mapping, a 3D gradient-echo variable flip angle (VFA) imaging sequence with TR/TE = 50/2.1 ms, utilizing five flip angles (5, 10, 15, 30, and 50 degrees) was acquired[34]. The flip angles used were optimized for characterizing the following signal model[34]

$$SI_{VFA}(\theta) = \frac{\mathrm{M_0}\sin(\theta)\,(1 - e^{-R_1 * TR})}{1 - \cos(\theta)\, e^{-R_1 * TR}}$$

in which $SI_{VFA}$ is the VFA signal as a function of flip angle, $\theta$, and $M_0$ incorporates the proton density. Using $R_1$ values from preliminary experiments and normalizing $M_0$ to one, the expected range of $SI_{VFA}$ curves is shown in Fig 4.2. Five flip angles were then chosen to accurately characterize the $SI_{VFA}$ curve and stratify curves for differing $R_1$ values within the expected range.

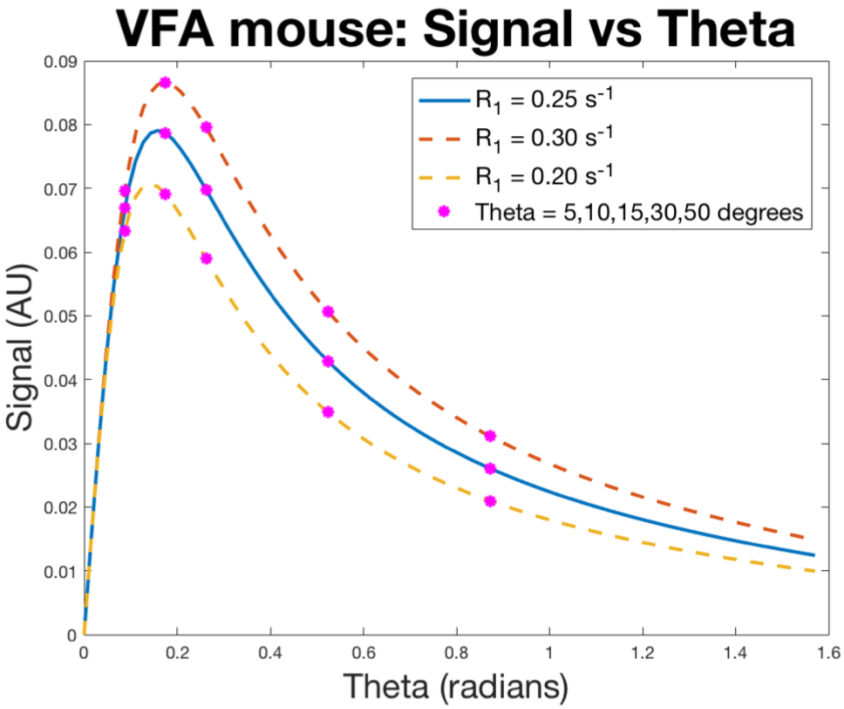

**Figure 4.2.** $SI_{VFA}$ curves as a function of $\theta$ (in radians) for the expected range of $R_1$ values: $R_1$ = 0.25 $s^{-1}$ [solid blue]; $R_1$ = 0.3 $s^{-1}$ [dashed orange]; and $R_1$ = 0.2 $s^{-1}$ [dashed yellow]. Each $SI_{VFA}$ curve is overlaid with the chosen flip angles [pink stars].

The flip angle that is most sensitive to $R_1$ differences over the expected range was determined by calculating the derivative of the difference between the $SI_{VFA}$ curves for $R_1$ = 0.3 $s^{-1}$ and $R_1$ = 0.2 $s^{-1}$ and solving for $\theta$, which was approximately 0.28 radians or 16°.

This calculated flip angle represents the optimum value for this expected $R_1$ range for a single flip angle. As we were using five flip angles, we selected a range of flip angles about the optimum flip angle, as shown in Fig. 4.3.

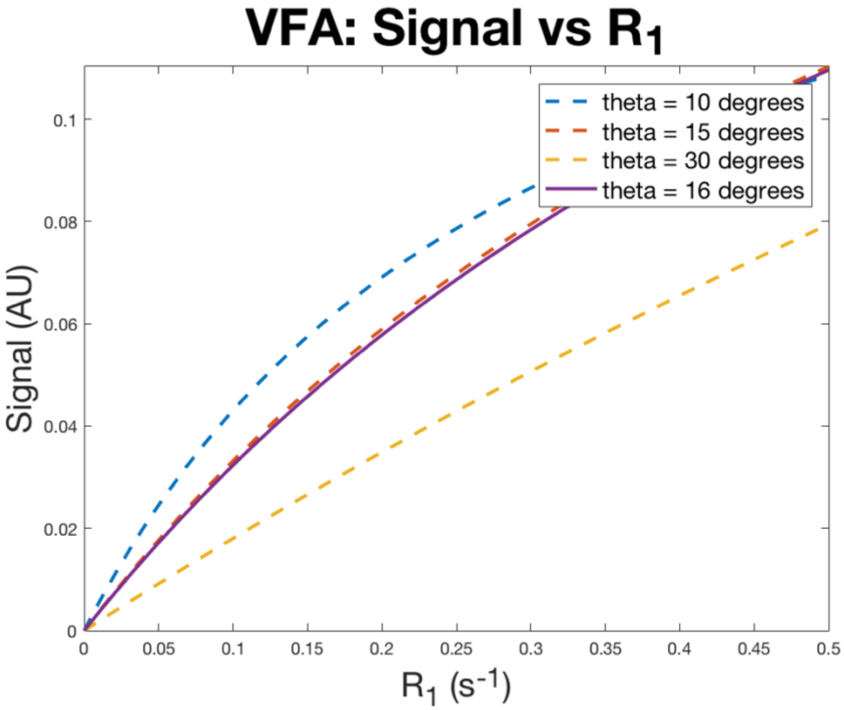

**Figure 4.3.** $SI_{VFA}$ curves as a function of $R_1$ showing the optimal flip angle (θ = 16°) [solid purple] and the middle three flip angles (θ = 10° [dashed blue], θ = 15° [dashed orange], and θ = 30° [dashed yellow]) from the chosen range of 5 flip angles for the expected range of $R_1$ = 0.2 $s^{-1}$ to 0.3 $s^{-1}$.

For $R_2$* mapping, a 3D multi-echo, gradient-echo imaging sequence was acquired with TR = 50 ms, flip angle = 15 degrees, six echoes starting at 2.1 ms, and an echo spacing of 4 ms. The echo times used were optimized for the following signal model:

$$SI_{TE}(t) = SI_0 e^{-t*R_2^*}$$

where $SI_{TE}$ is the signal intensity as a function of time, t, and $SI_0$ is the baseline signal intensity. Using $R_2^*$ values from preliminary experiments and normalizing $SI_0$ to one, the expected range of $SI_{TE}$ curves as a function of time are shown in figure 4.4 A. The echo time that is most sensitive to $R_2^*$ differences over the expected range was determined by calculating the derivative of the difference between the $SI_{TE}$ curves when $R_2^* = 100\ s^{-1}$ and $R_2^* = 40\ s^{-1}$ and solving for t to find the optimum TE, which was approximately 15.3 ms. The minimum TE of 2.1 ms was dictated by the scanner hardware and the echo spacing was chosen to be 4 ms such that the final array of 6 echoes was distributed about the optimum TE, as shown in figure 4.4 B.

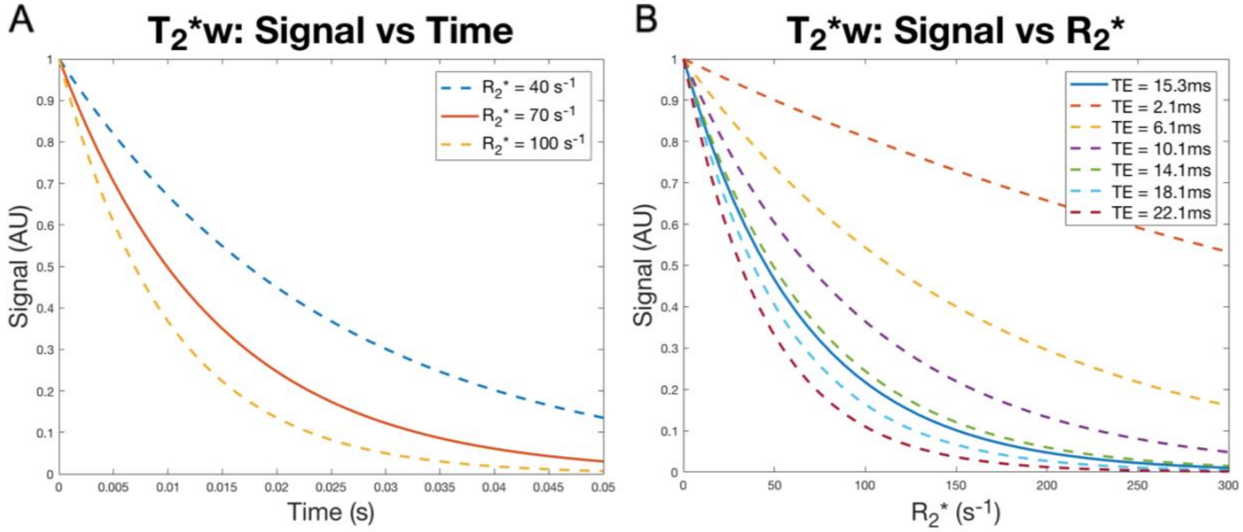

**Figure 4.4. A)** $SI_{TE}$ curves as a function of t in seconds for the expected range of $R_2^*$ values: $R_2^* = 40\ s^{-1}$ [dashed blue]; $R_2^* = 70\ s^{-1}$ [solid orange]; and $R_2^* = 100\ s^{-1}$ [dashed yellow]. **B)** The $SI_{TE}$ curves as a function of $R_2^*$ for the optimum TE = 15.3 ms [solid blue line] and the array of chosen TEs for the acquisition [dashed lines].

$R_1$ and $R_2^*$ maps were acquired both while the dams were freely breathing medical air (20% $O_2$) and 100% $O_2$ to modulate tissue and vasculature oxygenation. Optimal relaxation rate constants were determined *via* Bayesian probability theory based software[35] on a voxel-wise basis. Herein, the data points reflect the average across all voxels within a segmented region and the reported values represent the median of each distribution of points.

Placentas that were not fully covered by the anatomical scans were excluded from the volume results, but were included for $R_1$ and $R_2$* mapping. The numbers of full placentas at E14.5 were 95 (PE), 66 (healthy), and 21 (IUGR), while at E17.5, the numbers were 78 (PE), 63 (healthy), and 31 (IUGR), respectively. The combined numbers of full and partial placentas at E14.5 were 101 (PE), 82 (healthy), and 44 (IUGR), while at E17.5, the numbers were 88 (PE), 62 (healthy), and 44 (IUGR). Midway into the study, we determined that the $T_2$ contrast between the labyrinth and junctional zones was improved in anatomic images acquired while the mother was breathing 100% $O_2$ (Figs. 4.1 C and 4.1 D). Overall volume determinations were unaffected by breathing gas. The zone-specific analysis was only applied to images collected under 100% $O_2$; the numbers of such placentas at E14.5 were 18 (PE), 14 (healthy), and 44 (IUGR), while at E17.5, these numbers were 15 (PE), 14 (healthy), and 41(IUGR).

Following imaging on E17.5, IL-10 KO and healthy control mice were euthanized via cervical dislocation and an autopsy was performed to determine the size of the litter, note the number and location of unhealthy or resorbing fetuses, and weigh each placenta. For IUGR dams, euthanasia was performed with an IP injection of pentobarbital without disturbing the dam from the supine position in the imaging cradle. The autopsy was performed carefully and video-recorded so that the order of fetoplacental units from the ovary to the cervix could be determined and later matched to the anatomic images.

Manual segmentation was performed on the SEMS images and the resulting regions of interests were translated to the $R_1$ and $R_2$* maps using VOXA (VOXel based image Analysis toolset) custom image processing tools implemented in MATLAB (Mathworks, Natick, MA, USA) and co-developed by Pfizer, Inc. and the Mallinckrodt Institute of Radiology. Statistical analysis was performed using Origin (OriginLab Corporation, Northhampton, MA, USA) and the free and open source Jamovi Project software (The Jamovi Project, www.jamovi.org) using ANOVA and post hoc Tukey tests, in which $p < 0.05$ was regarded as statistically significant.

Herein, quantitative results are reported in the form of box and whisker plots to visualize the summary statistics, overlaid with the individual data points. The mean of each distribution is represented by an open square and the median is represented by the midline of the box. The top and bottom edges of the box represent the 75th and 25th percentiles, respectively, and the range which they cover is referred to as the interquartile range. The top and bottom whiskers represent the 95th and 5th percentiles, respectively and the dashes above the edge of the 95th percentile whisker and below the 5th percentile whisker denote the maximum and minimum values, respectively.

## 4.3 Results

### 4.3.1 Placental Volume

The placental volumes, shown in Fig. 4.5 A illustrate the differences between healthy, PE, and IUGR placentas at both gestational ages. Median placental volumes for each group can be found in Table 1. Significant differences in placental volumes are seen across cohorts ($p < 0.001$) and with gestational age ($p < 0.001$), specifically that healthy placentas are smaller than those of PE dams ($p < 0.001$), but larger than those characterized by IUGR ($p = 0.012$) and that PE placentas are larger than IUGR placentas ($p < 0.001$). A representative, high-resolution image of a PE mouse at E17.5 with two placentas indicated is shown in Fig. 4.5 B.

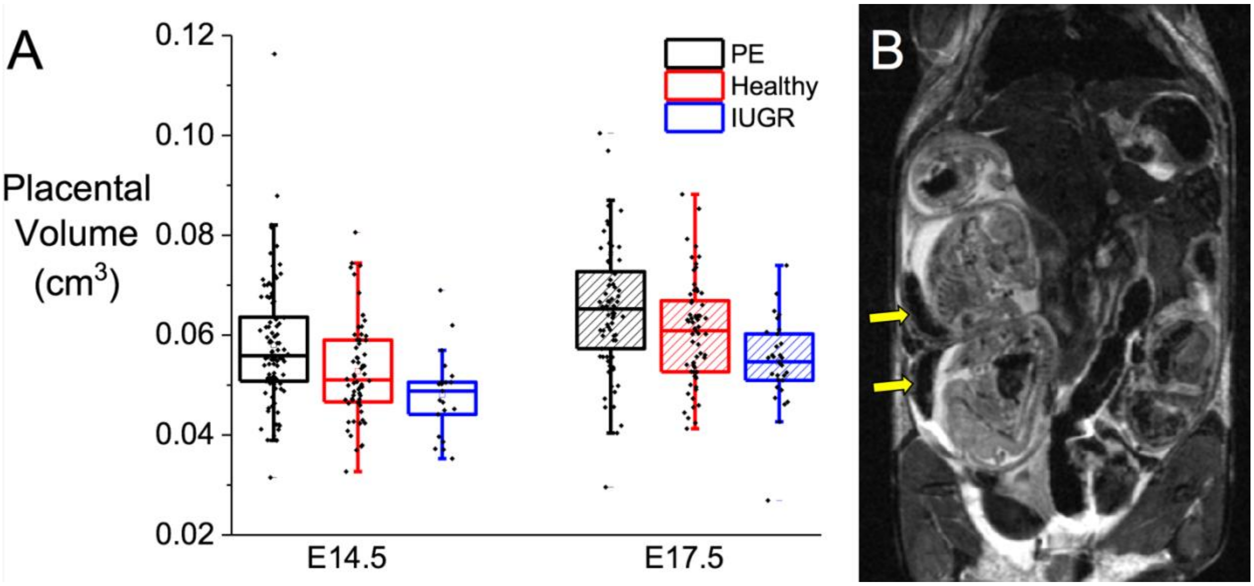

**Figure 4.5. Placental Volume. A)** Placental volumes across cohorts at gestational ages E14.5 and E17.5. Each data point represents a single placenta. Significant differences in placental volumes are seen across cohorts and with gestational age. Average placental volume in healthy dams is significantly smaller than in PE and greater than in IUGR, while average placental volume in PE is significantly larger than in IUGR. **B)** Representative high resolution $T_2$-weighted anatomic image within the mouse abdomen at E17.5 with yellow arrows indicating placentas.

**Table 4.1. Summary of median parameter values across each cohort of mice**

| | **E14.5** | | | **E17.5** | | |
|---|---|---|---|---|---|---|
| | **PE** | **Healthy** | **IUGR** | **PE** | **Healthy** | **IUGR** |
| **Volume [$cm^3$]** | 0.056 | 0.051 | 0.049 | 0.065 | 0.061 | 0.055 |
| **$R_1$ (air) [$s^{-1}$]** | 0.26 | 0.25 | 0.31 | 0.23 | 0.24 | 0.28 |
| **$R_1$ (100% $O_2$) [$s^{-1}$]** | 0.26 | 0.24 | 0.30 | 0.24 | 0.24 | 0.29 |
| **$\Delta R_1$ [$s^{-1}$]** | 0 | 0 | 0.01 | 0 | -0.01 | -0.01 |
| **$R_2$* (air) [$s^{-1}$]** | 115 | 130 | 122 | 136 | 139 | 144 |
| **$R_2$* (100% $O_2$) [$s^{-1}$]** | 99 | 93 | 92 | 131 | 137 | 146 |
| **$\Delta R_2$* [$s^{-1}$]** | 6 | 31 | 12 | 6 | 11 | -3 |
| **Junctional $R_2$* (air) [$s^{-1}$]** | 133 | 167 | 142 | 132 | 146 | 147 |
| **Junctional $R_2$* (100% $O_2$) [$s^{-1}$]** | 120 | 111 | 115 | 132 | 141 | 151 |
| **Junctional $\Delta R_2$* [$s^{-1}$]** | 7 | 63 | 8 | 6 | 3 | -2 |
| **Labyrinth $R_2$* (air) [$s^{-1}$]** | 117 | 120 | 86 | 130 | 153 | 134 |
| **Labyrinth $R_2$* (100% $O_2$) [$s^{-1}$]** | 114 | 70 | 70 | 112 | 124 | 130 |
| **Labyrinth $\Delta R_2$* [$s^{-1}$]** | 12 | 50 | 19 | 9 | 32 | -3 |

### 4.3.2 Placental $R_1$ and $\Delta R_1$

The average $R_1$ for all voxels within each placenta across cohorts, at both Gas, and with the breathing gas challenge is shown in figure 4.6 A and median $R_1$ values for each group can be found in Table 1. Significant differences are seen across cohorts ($p < 0.001$) and with GA ($p < 0.001$) but not due to the breathing gas challenge. $R_1$ of placentas in healthy dams is significantly less than that of PE placentas ($p < 0.001$) and IUGR placentas ($p < 0.001$) and, furthermore, IUGR $R_1$ is greater than that of PE ($p < 0.001$).

The change in average $R_1$ ($\Delta R_1 = R_1[air] – R_1[oxygen]$) between breathing air and oxygen across all voxels within each placenta across cohorts and at both Gas is shown in Fig. 4.6 B and median $\Delta R_1$ values for each group are listed in Table 1. $\Delta R_1$ is significantly different with GA ($p = 0.015$), but not with cohort. The color map of voxel wise $R_1$ values in Fig. 4.6 C for all placentas within a single image from a representative IUGR dam shows the heterogeneity of $R_1$ across and within the placentas.

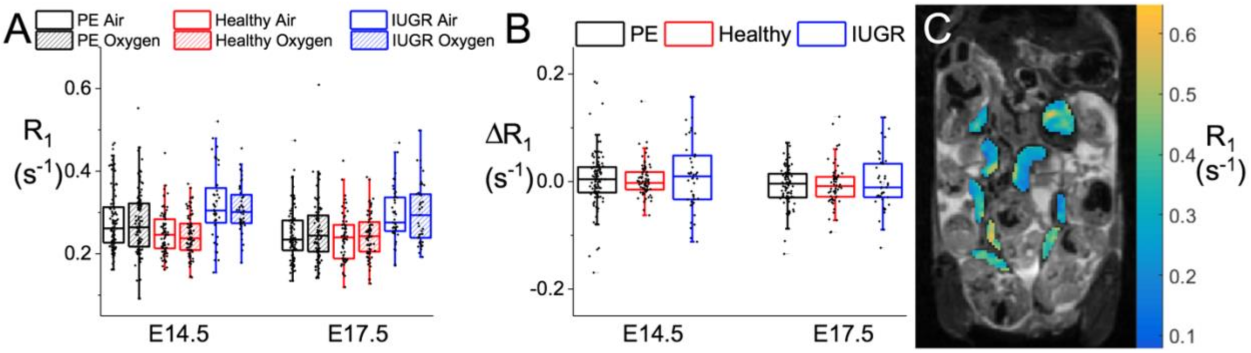

**Figure 4.6. Placental $R_1$ and $\Delta R_1$. A)** Placental $R_1$ across cohorts, with the breathing gas challenge, at each GA. Significant differences in placental $R_1$ are seen across cohorts and with GA. Average placental $R_1$ in healthy dams is less than in PE or IUGR; average $R_1$ in PE is less than in IUGR. **B)** Placental $\Delta R_1$ [$R_{1,Air} – R_{1,Oxygen}$] due to the breathing gas challenge across cohorts, at each GA. $\Delta R_1$ is significantly different with GA. Each point in **A)** and **B)** represents a single placenta. **C)** Representative color map of $R_1$ values at

E17.5 in an IUGR dam shows the heterogeneity of $R_1$ rate constants across and within each placenta.

### 4.3.3 Placental $R_2$* and $\Delta R_2$*

The average $R_2$* for all voxels within each placenta across cohorts, at both GAs, and with the breathing gas challenge is shown in figure 4.7 A and median $R_2$* values for each group are listed in Table 1. Significant differences are seen across cohorts ($p = 0.001$), with GA ($p < 0.001$), and in response to the breathing gas challenge ($p < 0.001$). $R_2$* values of placentas in healthy dams are greater than those of PE placentas ($p = 0.002$), but not different from IUGR placentas. $R_2$* values in placentas of PE and IUGR dams are not different from one another. The change in average $R_2$* ($\Delta R_2^* = R_2^*[\text{air}] - R_2^*[\text{oxygen}]$) between breathing air and oxygen for all voxels within each placenta across cohorts and at both GAs is shown in figure 4.7 B and median $\Delta R_2$* values for each group are listed in Table 1. $\Delta R_2$* is significantly different with GA ($p < 0.001$) and cohort ($p < 0.001$). Placental $\Delta R_2$* values in healthy dams are greater than those in either PE placentas ($p < 0.001$) or IUGR placentas ($p < 0.001$), though $\Delta R_2$*values in PE vs. IUGR placentas are not significantly different. The color map in Fig 4.7 C showing voxel-wise $R_2$* values for all placentas within a single image from a representative IUGR dam shows the intra- and inter-placental heterogeneity of $R_2$*.

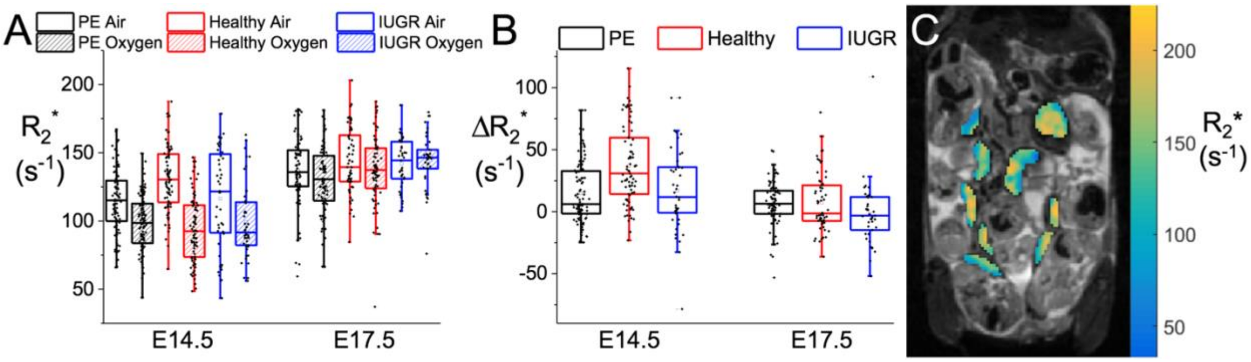

**Figure 4.7. Placental $R_2$* and $\Delta R_2$*. A)** Placental $R_2^*$ across cohorts, with the breathing gas challenge, at each GA. Significant differences in $R_2^*$ are seen across cohorts, GA, and due to the breathing gas challenge. Average $R_2^*$ in healthy dams is greater than in PE. **B)** Placental $\Delta R_2^*$ [$R_2^*{}_{Air} - R_2^*{}_{Oxygen}$] due to the breathing gas challenge is significantly different with GA and cohort. Average placental $\Delta R_2^*$ in healthy dams is significantly greater than in PE or IUGR. Each point in **A)** and **B)** represents a single placenta. **C)** Representative color map of $R_2^*$ values at E17.5 in an IUGR dam shows the heterogeneity of $R_2^*$ rate constants across and within each placenta.

### 4.3.4 Zone-Specific $R_1$ and $\Delta R_1$

The average $R_1$ values for all voxels within each junctional and labyrinth zone across cohorts, at both GAs, and with the breathing gas challenge is shown in Figs. 4.8 A and 4.8 B, respectively. Significant differences are seen in both the junctional (Fig. 4.8 A) and labyrinth (Fig. 4.8 B) zones with GA (junctional: $p < 0.001$; labyrinth: $p = 0.003$) and breathing gas challenge ($p < 0.001$). The change in average $R_1$ value between breathing air and oxygen for all voxels within each junctional and labyrinth zones across cohorts and at both GAs is shown in Figs. 4.8 C and 4.8 D, respectively. No statistically significant differences in either junctional and labyrinth zone $\Delta R_1$ due to the gas challenge are seen with cohorts or GA.

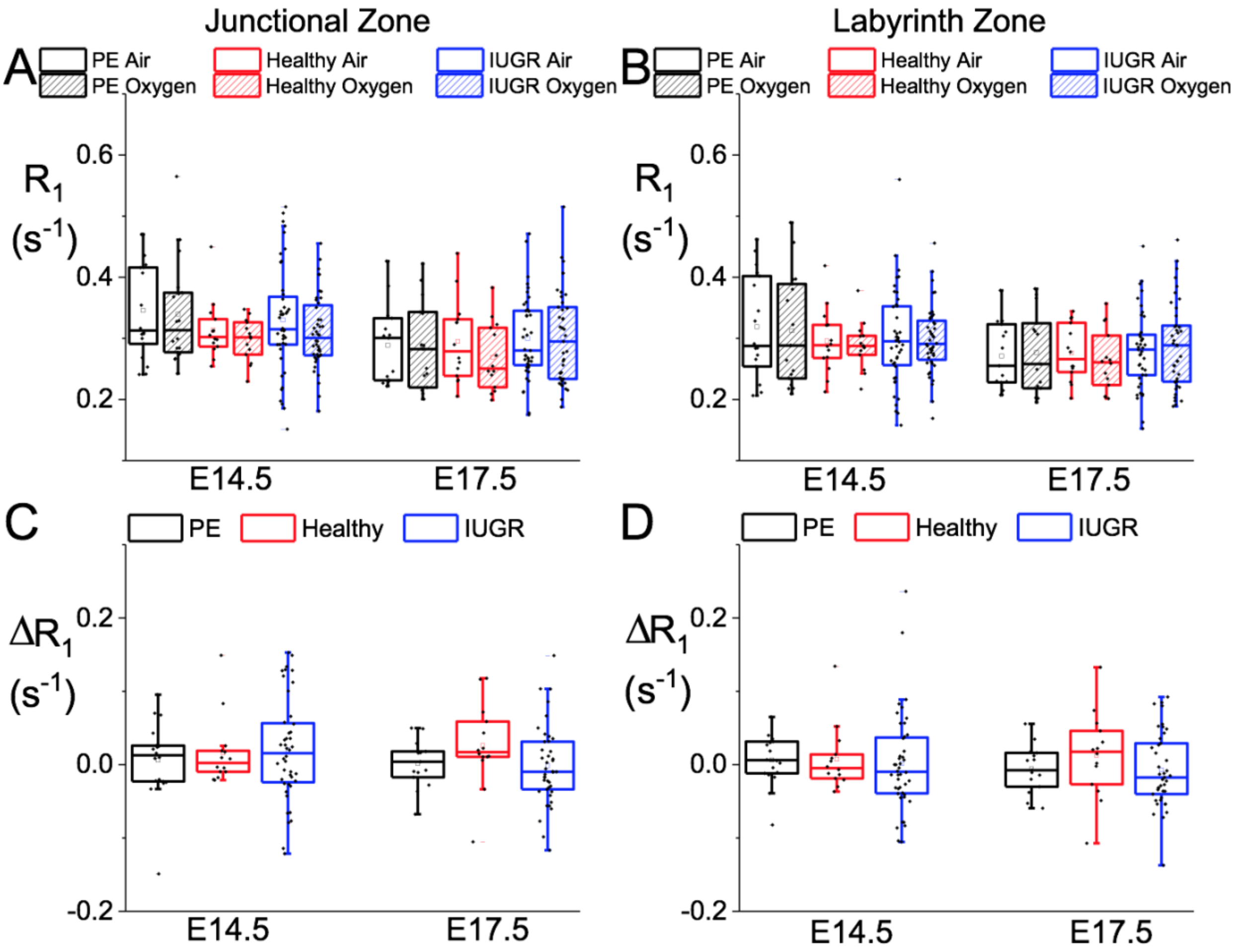

**Figure 4.8. Zone-specific $R_1$ and $\Delta R_1$.** Placental $R_1$ in the **A)** Junctional and **B)** Labyrinth zones and $\Delta R_1$ in the **C)** Junctional and **D)** Labyrinth zones. Each point represents a single placental zone. **A)** Statistically significant differences in junctional zone $R_1$ seen with GA. **B)** Statistically significant differences in labyrinth zone $R_1$ seen with GA. **C) & D)** No statistically significant differences in either junctional and labyrinth zone $\Delta R_1$ due to the gas challenge are seen with cohorts or GA.

### 4.3.5 Zone-Specific $R_2$* and $\Delta R_2$*

The average $R_2$* values for all voxels within each junctional and labyrinth zone across cohorts, at both GAs, and with the breathing gas challenge is shown in Figs. 4.9 A and 4.9 B, respectively. Median $R_2$* values for each distribution are listed in Table 1. Significant differences are seen in both the junctional (Fig. 4.9 A) and labyrinth (Fig. 4.9

B) zones with GA (junctional: $p = 0.005$; labyrinth: $p < 0.001$) and breathing gas challenge ($p < 0.001$). The change in average $R_2^*$ value between breathing air and oxygen for all voxels within each junctional and labyrinth zones across cohorts and at both GAs is shown in Figs. 4.9 C and 4.9 D, respectively. Median $\Delta R_2^*$ values for each group are listed in Table 1. Significant differences are seen in both the junctional and labyrinth zones across cohorts ($p < 0.001$) and with GA ($p < 0.001$). Junctional zone $\Delta R_2^*$ in response to the gas challenge is greater in placentas in healthy dams than in PE ($p = 0.029$) or IUGR ($p < 0.001$) placentas. $\Delta R_2^*$ in junctional zones in PE and IUGR placentas are not significantly different from one another. Labyrinth zone $\Delta R_2^*$ in response to the gas challenge is greater in placentas in healthy dams than in IUGR placentas ($p < 0.001$), but not in PE placentas. Labyrinth $\Delta R_2^*$ values in PE placentas are greater than in IUGR placentas ($p = 0.036$).

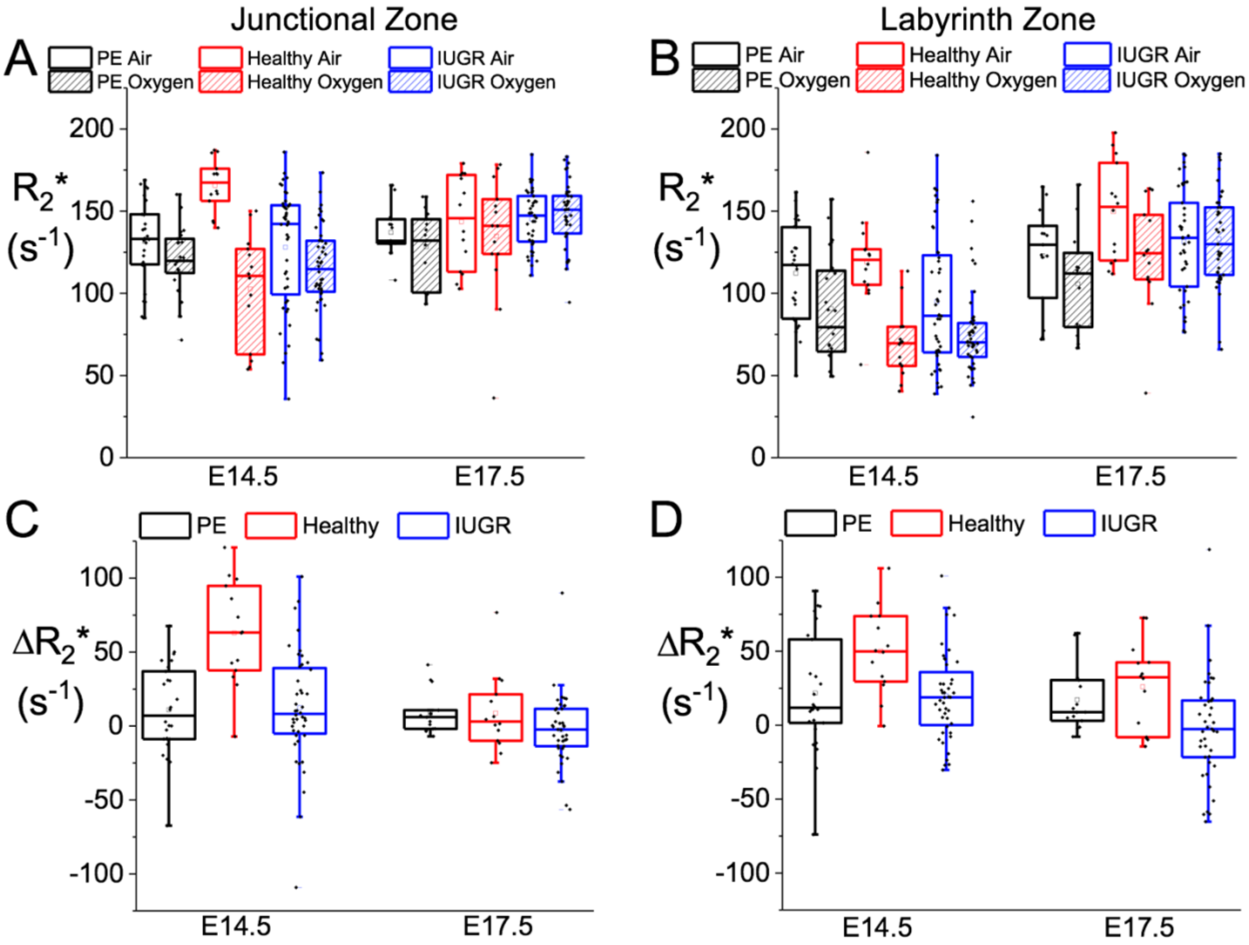

**Figure 4.9. Zone-specific R2* and ΔR2*.** Placental $R_2$* in the **A)** Junctional and **B)** Labyrinth zones and $\Delta R_2$* in the **C)** Junctional and **D)** Labyrinth zones. Each point represents a single placental zone. **A)** Statistically significant differences in junctional zone $R_2$* are seen with GA and breathing gas challenge. **B)** Statistically significant differences in labyrinth zone $R_2$* are seen with GA and breathing gas challenge. **C)** Statistically significant differences in junctional zone $\Delta R_2$* due to the gas challenge are seen across cohorts and with GA, with the response in placentas in healthy dams being greater than in PE or IUGR. **D)** Statistically significant differences in labyrinth zone $\Delta R_2$* due to the gas challenge are seen across cohorts and with GA, with the response in placentas in healthy dams greater than in IUGR and the response in PE greater than in IUGR.

## 4.4 Discussion

Optimal timing of early delivery in cases of placental dysfunction is critical. Biomarkers which can report whether suboptimal placental function supports continued fetal growth and guide the decision to deliver early are needed. Clinical cases of placental dysfunction can have many potential causes[36] further complicated by non-uniform classification and nomenclature[37], increasing the difficulty of establishing reliable biomarkers. Pre-clinical experiments allow for greater control of external variables in cases of pregnancy complications and could provide useful direction for future clinical studies.

### 4.4.1 Placental Volume

Median placental volumes for the healthy cohort at each GA agree well with reported stereological determinations of murine placental volumes at similar stages of gestation[38]. Clinical studies have shown that placental volume increases with GA[39, 40], similar to our results. Additionally, differences in placental volume across cohorts are supported by ultrasound (US) based clinical investigations that postulate abnormal placental volume is related to low birth weight[40, 41]. However, these 2D and 3D US-based volume techniques have their limitations and are generally restricted to first and second trimester determinations with conflicting reports of reproducibility[42]. Recent advances in 3D US techniques which manually combine multiple images allow for whole placenta imaging with improved reproducibility, but as yet are still restricted to only second trimester capabilities[43]. MRI’s superior ability to probe the entire abdomen eliminates this gestational limitation such that placental volumes can be tracked accurately across gestation, including during the third trimester. We have shown that murine placental volumes differ across cohorts; placentas in the PE model are relatively larger and IUGR placentas are relatively smaller compared with healthy controls. These volume differences are likely explained by differences in blood flow altering the total blood volume, as blood volume makes up approximately 50% of the placental volume[44]. Maternal hypertension and improper development of the maternal spiral arteries in PE placentas have been proposed to result in increased branching and capillary volume fraction[36], resulting in larger placental volumes. The bidirectional blood flow and multi-fetus litter in the murine uterus naturally creates a gradient of blood flow to each fetoplacental unit[45]. The blood flow in the crowded uterine horn is insufficient to adequately perfuse all of the placentas, an effect that results in smaller placental volumes in the central fetoplacental units[22]. Clinical studies of placental perfusion and diffusion-based techniques assessed by MRI have shown decreased perfusion and diffusion in placentas characterized by IUGR[29, 46], supporting the hypothesis that the volume differences seen are due to differences in blood volume.

### 4.4.2 Placental $R_1$ and $\Delta R_1$

Clinical studies comparing healthy pregnancies with dysfunctional placentas found significantly higher baseline $R_1$ in placentas complicated by severe FGR[47] and increased $R_1$ generally in compromised pregnancies[48], similar to our results in IUGR mice. The unknown causes of FGR in humans complicates interpretation of this increased baseline $R_1$, however, in mice this could be due to hormonal differences resulting from the hemiovariectomy. Studies have shown that hemiovariectomy increases follicle stimulating hormone and decreases progesterone, inducing hyperplasia in the remaining ovary[49], and could feasibly affect other organs. Bovine studies showed that reduction of serum progesterone coincided with decreased partial pressure of oxygen within the ovarian vein[50]. The increased $R_1$ in IUGR placentas could be due to these systemic hormonal changes resulting from the hemiovariectomy. The ovaries produce estrogen, testosterone, and progesterone[51, 52] and removal of one or both can induce systemic effects[49, 53, 54]. Retrospective $R_1$ measurements within the maternal spinal muscle visible in our anatomic images also showed increased $R_1$ in IUGR dams compared to healthy (Fig 4.10), supporting the hypothesis of systemic differences. The placenta is responsible for the creation and secretion of certain hormones and signaling molecules during pregnancy that are known to enter the maternal circulation[55]. Therefore, it is possible that the dysfunctional placenta is driving the increased $R_1$ seen clinically via similar systemic effects.

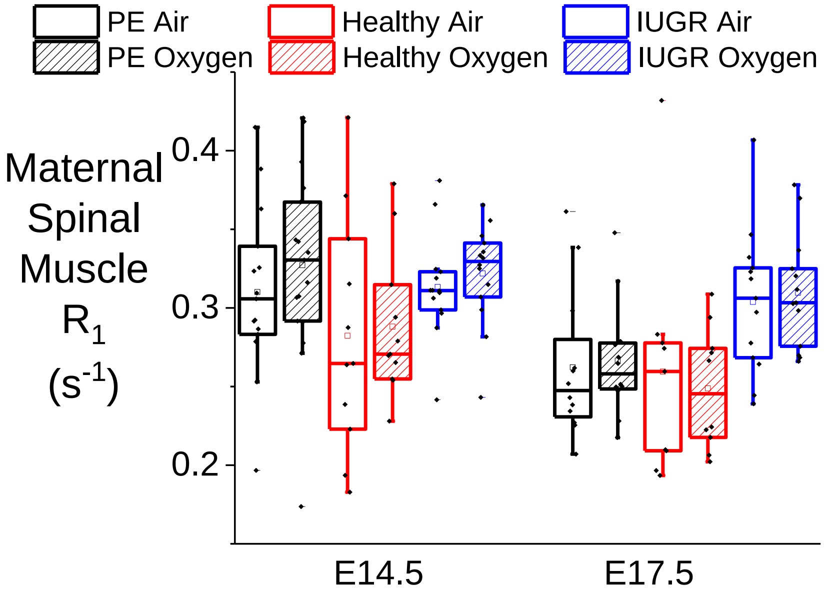

**Figure 4.10. Maternal spinal muscle $R_1$.** Each point represents a dam measurement. Maternal spinal muscle $R_1$ across cohorts, with the breathing gas challenge, at each GA. Significant differences in maternal $R_1$ are seen across cohorts ($p < 0.001$) and with GA ($p < 0.001$). A post hoc Tukey test shows that the healthy $R_1$ is less than the IUGR ($p < 0.001$) but not different from PE and also the PE $R_1$ is less than the IUGR ($p = 0.047$).

The breathing gas challenge was expected to induce small changes in $R_1$, due to the weak paramagnetic nature of $O_2$[26]. Herein, the $R_1$ response to the gas challenge is near zero for all cohorts at both gestational ages. Others have reported measurable $R_1$ differences in murine placentas in response to variations in breathing gas from 20% to 100% $O_2$[56]. One possibility for the lack of measured $R_1$ response to the gas challenge is that the VFA sequence lacks the necessary sensitivity to detect the expected small differences. Studies in healthy human pregnancies have shown that baseline $R_1$ values decrease with GA[57, 58] and the change in $R_1$ with gas challenge also decreases with GA[59], with term-equivalent change in $R_1$ values near zero. A similar decrease in $\Delta R_1$ with increasing GA have also been observed in cases of severe FGR[47]. The necessary precision and the small anticipated effect make $R_1$ measurements with a gas challenge unlikely to provide clinically useful results at near-term or term, although it may provide useful results earlier in gestation when $\Delta R_1$ is greater.

### 4.4.3 Placental $R_2$* and $\Delta R_2$*

As $R_2$* is proportional to the concentration of deoxyhemoglobin within the vasculature, baseline $R_2$* values increasing with GA are likely due to the significant oxygen requirements of the growing, developing fetus that drive greater exchange of $O_2$ across the placenta. Placental hemoglobin saturation of $O_2$ has been reported to decrease with GA[59], resulting in increased baseline $R_2$*. A similar result was previously shown where the true transverse relaxation rate constant ($R_2$) also increased with GA[57]. Additionally, in a study comparing $R_2$ values in healthy and FGR pregnancies in conjunction with Doppler US, it was shown that $R_2$ values in placentas that yielded FGR fetuses were significantly higher than healthy controls and were correlated with impedance to flow in the uterine arteries as measured by US[60]. We also found significant differences in baseline $R_2^*$ across cohorts, however with $R_2^*$ decreased in IUGR placentas with respect to healthy controls. As $R_2^*$ is the combination of $R_2$ (microscopic fluctuations in the magnetic field) and inhomogeneous broadening due to magnetic susceptibility effects (macroscopic fluctuations in the magnetic field), the inhomogeneous component may be masking the changes seen in only $R_2$ had that been measured directly in this experiment. It is also possible that our particular model for IUGR result from different underlying causes than the severe cases of FGR in that study.

The decrease in $R_2^*$ when the mother is breathing 100% $O_2$ is expected due to the decrease in deoxygenated hemoglobin. This has been shown to occur clinically in healthy pregnancies[59, 61] and cases of dysfunction[61]. The $\Delta R_2^*$ response to gas challenge varies across cohorts at E14.5, suggesting this may be a good biomarker of placental function for pre-term pregnancies, but is diminished at E17.5 to nearly no change. Clinical reports of $R_2^*$ response to gas challenge vary greatly with GA[59, 61, 62] and across cohorts[47, 61].

### 4.4.4 Zone-Specific $R_1$ and $\Delta R_1$

Zone specific analysis of $R_1$ recapitulated the lack of response to the gas challenge seen in the whole placenta.

### 4.4.5 Zone-Specific $R_2^*$ and $\Delta R_2^*$

To our knowledge, there have been no previously reported $R_2^*$ and $\Delta R_2^*$ in zone-specific regions of the murine placenta. $R_2^*$ measurements within the junctional and labyrinth zones show subtle differences. In the junctional zone, both $R_2^*$ and $\Delta R_2^*$ show very similar trends as those seen in the whole placenta (very little differences in baseline $R_2$* and $\Delta R_2$* with the gas challenge at E17.5), whereas in the labyrinth zone, baseline $R_2$* and $\Delta R_2$* response to gas challenge show differences at both E14.5 and E17.5. Using our segmentation and layer determination protocol, the junctional zone makes up more than 50% of the placental volume, which explains the similarity of trends. $R_2$* measurements within the labyrinth zone at baseline and $\Delta R_2$* with the gas challenge show promise as a potential biomarker for placental function at both pre-term and term.

Historically, MRI in pregnancy has been used clinically to evaluate abnormal implantation[63], with more recent studies highlighting MRI's capability to assess placental function[29, 47, 64, 65]. Herein, we have used MRI to demonstrate differences in placental developmental between healthy and models of PE and IUGR with respect to placental volume. We have also shown that $R_2$* and $\Delta R_2$* responses to gas challenge can distinguish healthy placentas from PE and IUGR placentas and is a promising biomarker of placental function at near-term and term. Additional studies to confirm these results in human placentas are needed. Improved markers of placental development and function could aid in optimal timing of delivery in cases of placental dysfunction.

## 4.5 Acknowledgements

Research was supported, in part, by National Institute of Health grants: R01 HD086323, T32 EB014855, and the Small Animal Cancer Imaging Shared Resource of the Alvin J. Siteman Cancer Center (P30 CA091842). Valuable discussions with Professors Joseph JH Ackerman and Jeffrey J Neil are gratefully acknowledged. The studies presented in

this work were carried out, in part, using the Small Animal Magnetic Resonance Facility of the Washington University Mallinckrodt Institute of Radiology.

## 4.6 References

**[1]**. Crane JM, Van den Hof MC, Dodds L, Armson BA, Liston R. Maternal complications with placenta previa. *Am J Perinatol.* 2000;17(2):101-105.10.1055/s-2000-9269.

**[2]**. Alfirevic Z, Roberts D, Martlew V. How strong is the association between maternal thrombophilia and adverse pregnancy outcome? A systematic review. *Eur J Obstet Gynecol Reprod Biol.* 2002;101(1):6-14.10.1016/s0301-2115(01)00496-1.

**[3]**. Burton GJ, Fowden AL, Thornburg KL. Placental Origins of Chronic Disease. *Physiol Rev.* 2016;96(4):1509-1565.10.1152/physrev.00029.2015.

**[4]**. Thornburg KL, O'Tierney PF, Louey S. Review: The placenta is a programming agent for cardiovascular disease. *Placenta.* 2010;31 Suppl:S54-59.10.1016/j.placenta.2010.01.002.

**[5]**. Thornburg KL, Shannon J, Thuillier P, Turker MS. In utero life and epigenetic predisposition for disease. *Adv Genet.* 2010;71:57-78.10.1016/B978-0-12-380864-6.00003-1.

**[6]**. Maslen CL. Recent Advances in Placenta-Heart Interactions. *Front Physiol.* 2018;9:735.10.3389/fphys.2018.00735.

**[7]**. Duley L. The global impact of pre-eclampsia and eclampsia. *Semin Perinatol.* 2009;33(3):130-137.10.1053/j.semperi.2009.02.010.

**[8]**. Duley L. Pre-eclampsia, eclampsia, and hypertension. *BMJ Clin Evid.* 2011;2011

**[9]**. Jeyabalan A. Epidemiology of preeclampsia: impact of obesity. *Nutr Rev.* 2013;71 Suppl 1:S18-25.10.1111/nure.12055.

**[10]**. Romo A, Carceller R, Tobajas J. Intrauterine growth retardation (IUGR): epidemiology and etiology. *Pediatr Endocrinol Rev.* 2009;6 Suppl 3:332-336

**[11]**. Resnik R. Intrauterine growth restriction. *Obstet Gynecol.* 2002;99(3):490-496.10.1016/s0029-7844(01)01780-x.

**[12]**. Costa ML, de Moraes Nobrega G, Antolini-Tavares A. Key Infections in the Placenta. *Obstet Gynecol Clin North Am.* 2020;47(1):133-146.10.1016/j.ogc.2019.10.003.

**[13]**. Prada JA, Tsang RC. Biological mechanisms of environmentally induced causes of IUGR. *Eur J Clin Nutr.* 1998;52 Suppl 1:S21-27; discussion S27-28

**[14]**. Imakawa K, Nakagawa S. The Phylogeny of Placental Evolution Through Dynamic Integrations of Retrotransposons. *Prog Mol Biol Transl Sci.* 2017;145:89-109.10.1016/bs.pmbts.2016.12.004.

**[15]**. Georgiades P, Ferguson-Smith AC, Burton GJ. Comparative developmental anatomy of the murine and human definitive placentae. *Placenta.* 2002;23(1):3-19.10.1053/plac.2001.0738.

**[16]**. Rai A, Cross JC. Development of the hemochorial maternal vascular spaces in the placenta through endothelial and vasculogenic mimicry. *Dev Biol.* 2014;387(2):131-141.10.1016/j.ydbio.2014.01.015.

**[17]**. Murray SA, Morgan JL, Kane C, et al. Mouse gestation length is genetically determined. *PLoS One.* 2010;5(8):e12418.10.1371/journal.pone.0012418.

**[18]**. Vom Saal FS, Dhar MG. Blood flow in the uterine loop artery and loop vein is bidirectional in the mouse: implications for transport of steroids between fetuses. *Physiol Behav.* 1992;52(1):163-171.10.1016/0031-9384(92)90447-a.

**[19]**. Avni R, Raz T, Biton IE, Kalchenko V, Garbow JR, Neeman M. Unique in utero identification of fetuses in multifetal mouse pregnancies by placental bidirectional arterial spin labeling MRI. *Magn Reson Med.* 2012;68(2):560-570.10.1002/mrm.23246.

**[20]**. Chatterjee P, Chiasson VL, Kopriva SE, et al. Interleukin 10 deficiency exacerbates toll-like receptor 3-induced preeclampsia-like symptoms in mice. *Hypertension.* 2011;58(3):489-496.10.1161/HYPERTENSIONAHA.111.172114.

**[21]**. Chen X, Li P, Liu M, et al. Gut dysbiosis induces the development of pre-eclampsia through bacterial translocation. *Gut.* 2020;69(3):513-522.10.1136/gutjnl-2019-319101.

**[22]**. Coe BL, Kirkpatrick JR, Taylor JA, vom Saal FS. A new 'crowded uterine horn' mouse model for examining the relationship between foetal growth and adult obesity. *Basic Clin Pharmacol Toxicol.* 2008;102(2):162-167.10.1111/j.1742-7843.2007.00195.x.

**[23]**. Swanson AM, David AL. Animal models of fetal growth restriction: Considerations for translational medicine. *Placenta.* 2015;36(6):623-630.10.1016/j.placenta.2015.03.003.

**[24]**. Jang EA, Longo LD, Goyal R. Antenatal maternal hypoxia: criterion for fetal growth restriction in rodents. *Front Physiol.* 2015;6:176.10.3389/fphys.2015.00176.

**[25]**. Kuhn R, Lohler J, Rennick D, Rajewsky K, Muller W. Interleukin-10-deficient mice develop chronic enterocolitis. *Cell.* 1993;75(2):263-274.10.1016/0092-8674(93)80068-p.

**[26]**. Beeman SC, Shui YB, Perez-Torres CJ, Engelbach JA, Ackerman JJ, Garbow JR. O2 -sensitive MRI distinguishes brain tumor versus radiation necrosis in murine models. *Magn Reson Med.* 2016;75(6):2442-2447.10.1002/mrm.25821.

**[27]**. O'Connor JP, Naish JH, Parker GJ, et al. Preliminary study of oxygen-enhanced longitudinal relaxation in MRI: a potential novel biomarker of oxygenation changes in solid tumors. *Int J Radiat Oncol Biol Phys.* 2009;75(4):1209-1215.10.1016/j.ijrobp.2008.12.040.

**[28]**. Ding Y, Mason RP, McColl RW, et al. Simultaneous measurement of tissue oxygen level-dependent (TOLD) and blood oxygenation level-dependent (BOLD) effects in abdominal tissue oxygenation level studies. *J Magn Reson Imaging.* 2013;38(5):1230-1236.10.1002/jmri.24006.

**[29]**. Siauve N, Chalouhi GE, Deloison B, et al. Functional imaging of the human placenta with magnetic resonance. *Am J Obstet Gynecol.* 2015;213(4 Suppl):S103-114.10.1016/j.ajog.2015.06.045.

**[30]**. Ingram E, Hawkins L, Morris DM, et al. R1 changes in the human placenta at 3 T in response to a maternal oxygen challenge protocol. *Placenta.* 2016;39:151-153.10.1016/j.placenta.2016.01.016.
**[31]**. Ogawa S, Lee TM, Kay AR, Tank DW. Brain magnetic resonance imaging with contrast dependent on blood oxygenation. *Proc Natl Acad Sci U S A.* 1990;87(24):9868-9872.10.1073/pnas.87.24.9868.
**[32]**. Ogawa S, Lee TM, Nayak AS, Glynn P. Oxygenation-sensitive contrast in magnetic resonance image of rodent brain at high magnetic fields. *Magn Reson Med.* 1990;14(1):68-78.10.1002/mrm.1910140108.
**[33]**. Otsu N. Threshold Selection Method from Gray-Level Histograms. *Ieee T Syst Man Cyb.* 1979;9(1):62-66.Doi 10.1109/Tsmc.1979.4310076.
**[34]**. Fram EK, Herfkens RJ, Johnson GA, et al. Rapid calculation of T1 using variable flip angle gradient refocused imaging. *Magn Reson Imaging.* 1987;5(3):201-208.10.1016/0730-725x(87)90021-x.
**[35]**. Quirk JD, Bretthorst GL, Garbow JR, Ackerman JJH. Magnetic resonance data modeling: The Bayesian analysis toolbox. *Concept Magn Reson A.* 2018;47a(2).ARTN e21467. 10.1002/cmr.a.21467.
**[36]**. Kingdom JC, Kaufmann P. Oxygen and placental villous development: origins of fetal hypoxia. *Placenta.* 1997;18(8):613-621; discussion 623-616.10.1016/s0143-4004(97)90000-x.
**[37]**. Redline RW. The clinical implications of placental diagnoses. *Semin Perinatol.* 2015;39(1):2-8.10.1053/j.semperi.2014.10.002.
**[38]**. Coan PM, Ferguson-Smith AC, Burton GJ. Developmental dynamics of the definitive mouse placenta assessed by stereology. *Biol Reprod.* 2004;70(6):1806-1813.10.1095/biolreprod.103.024166.
**[39]**. Thame M, Osmond C, Bennett F, Wilks R, Forrester T. Fetal growth is directly related to maternal anthropometry and placental volume. *European Journal of Clinical Nutrition.* 2004;58(6):894-900.10.1038/sj.ejcn.1601909.
**[40]**. Isakov KMM, Emerson JW, Campbell KH, et al. Estimated Placental Volume and Gestational Age. *Am J Perinatol.* 2018;35(8):748-757.10.1055/s-0037-1615285.
**[41]**. Wolf H, Oosting H, Treffers PE. Second-trimester placental volume measurement by ultrasound: prediction of fetal outcome. *Am J Obstet Gynecol.* 1989;160(1):121-126.10.1016/0002-9378(89)90102-6.
**[42]**. Hata T, Tanaka H, Noguchi J, Hata K. Three-dimensional ultrasound evaluation of the placenta. *Placenta.* 2011;32(2):105-115.10.1016/j.placenta.2010.11.001.
**[43]**. Cheung WS, G. N.; de Melo Tavares Ferreira, A. G.; Alphonse, J.; Welsh, A. W. Feasibility of image registration and fusion for evaluation of structure and perfusion of the entire second trimester placenta by three-dimensional power Doppler ultrasound. *Placenta.* 2020;94(May 2020):13-19.https://doi.org/10.1016/j.placenta.2020.03.005.
**[44]**. Gowland P. Placental MRI. *Semin Fetal Neonatal Med.* 2005;10(5):485-490.10.1016/j.siny.2005.05.001.
**[45]**. Even MD, Laughlin MH, Krause GF, vom Saal FS. Differences in blood flow to uterine segments and placentae in relation to sex, intrauterine location and side in pregnant rats. *J Reprod Fertil.* 1994;102(1):245-252.10.1530/jrf.0.1020245.

**[46]**. Andescavage NY, W.; Jacobs, M.; Kapse, K.; Quistorff, J.; Bulas, D.; Ahmadzia, H.; Gimovsky, A.; Baschat, A.; Limperopoulos, C. Exploring in vivo placental microstructure in healthy and growth-restricted pregnancies through diffusion-weighted magnetic resonance imaging. *Placenta.* 2020;93(April 2020):113-118.https://doi.org/10.1016/j.placenta.2020.03.004.

**[47]**. Ingram E, Morris D, Naish J, Myers J, Johnstone E. MR Imaging Measurements of Altered Placental Oxygenation in Pregnancies Complicated by Fetal Growth Restriction. *Radiology.* 2017;285(3):953-960.10.1148/radiol.2017162385.

**[48]**. Duncan KR, Gowland P, Francis S, Moore R, Baker PN, Johnson IR. The investigation of placental relaxation and estimation of placental perfusion using echo-planar magnetic resonance imaging. *Placenta.* 1998;19(7):539-543.10.1016/s0143-4004(98)91048-7.

**[49]**. Bhagat L, Duraiswami S, Kumari GL. Role of Follicle-Stimulating-Hormone in the Induction of Hyperplasia during Compensatory Ovarian Hypertrophy. *J Bioscience.* 1993;18(1):59-72.Doi 10.1007/Bf02703038.

**[50]**. Acosta TJ, Bah MB, Korzekwa A, et al. Acute changes in circulating concentrations of progesterone and nitric oxide and partial pressure of oxygen during prostaglandin F2alpha-induced luteolysis in cattle. *J Reprod Dev.* 2009;55(2):149-155.10.1262/jrd.20133.

**[51]**. Adashi EY. Endocrinology of the ovary. *Hum Reprod.* 1994;9(5):815-827.10.1093/oxfordjournals.humrep.a138602.

**[52]**. Colvin CW, Abdullatif H. Anatomy of female puberty: The clinical relevance of developmental changes in the reproductive system. *Clin Anat.* 2013;26(1):115-129.10.1002/ca.22164.

**[53]**. Barco AI, Flores A, Chavira R, Damian-Matsumura P, Dominguez R, Cruz ME. Asymmetric effects of acute hemiovariectomy on steroid hormone secretion by the in situ ovary. *Endocrine.* 2003;21(3):209-215.10.1385/ENDO:21:3:209.

**[54]**. Flores A, Rodriguez JO, Palafox MT, et al. The acute asymmetric effects of hemiovariectomy on testosterone secretion vary along the estrous cycle. The participation of the cholinergic system. *Reprod Biol Endocrinol.* 2006;4:11.10.1186/1477-7827-4-11.

**[55]**. Costa MA. The endocrine function of human placenta: an overview. *Reprod Biomed Online.* 2016;32(1):14-43.10.1016/j.rbmo.2015.10.005.

**[56]**. Avni R, Golani O, Akselrod-Ballin A, et al. MR Imaging-derived Oxygen-Hemoglobin Dissociation Curves and Fetal-Placental Oxygen-Hemoglobin Affinities. *Radiology.* 2016;280(1):68-77.10.1148/radiol.2015150721.

**[57]**. Gowland PA, Freeman A, Issa B, et al. In vivo relaxation time measurements in the human placenta using echo planar imaging at 0.5 T. *Magn Reson Imaging.* 1998;16(3):241-247.10.1016/s0730-725x(97)00308-1.

**[58]**. Wright C, Morris DM, Baker PN, et al. Magnetic resonance imaging relaxation time measurements of the placenta at 1.5 T. *Placenta.* 2011;32(12):1010-1015.10.1016/j.placenta.2011.07.008.

**[59]**. Huen I, Morris DM, Wright C, et al. R1 and R2 * changes in the human placenta in response to maternal oxygen challenge. *Magn Reson Med.* 2013;70(5):1427-1433.10.1002/mrm.24581.

**[60]**. Derwig I, Barker GJ, Poon L, et al. Association of placental T2 relaxation times and uterine artery Doppler ultrasound measures of placental blood flow. *Placenta.* 2013;34(6):474-479.10.1016/j.placenta.2013.03.005.

**[61]**. Sinding M, Peters DA, Poulsen SS, et al. Placental baseline conditions modulate the hyperoxic BOLD-MRI response. *Placenta.* 2018;61:17-23.10.1016/j.placenta.2017.11.002.

**[62]**. Sorensen A, Peters D, Simonsen C, et al. Changes in human fetal oxygenation during maternal hyperoxia as estimated by BOLD MRI. *Prenat Diagn.* 2013;33(2):141-145.10.1002/pd.4025.

**[63]**. Zaghal AA, Hussain HK, Berjawi GA. MRI evaluation of the placenta from normal variants to abnormalities of implantation and malignancies. *J Magn Reson Imaging.* 2019;50(6):1702-1717.10.1002/jmri.26764.

**[64]**. Aughwane R, Ingram E, Johnstone ED, Salomon LJ, David AL, Melbourne A. Placental MRI and its application to fetal intervention. *Prenat Diagn.* 2020;40(1):38-48.10.1002/pd.5526.

**[65]**. Avni R, Neeman M, Garbow JR. Functional MRI of the placenta--From rodents to humans. *Placenta.* 2015;36(6):615-622.10.1016/j.placenta.2015.04.003.

# Chapter 5: Functional and Developmental Effects of Zika Virus Infection and Hydroxychloroquine Treatment in Murine Placenta

## 5.1 Introduction

Zika virus (ZIKV) is a mosquito-borne flavivirus which was first documented in monkeys in Uganda in 1947 and later in humans in other regions of sub-Saharan Africa. ZIKV is related to other human pathogens such as dengue, yellow fever, West Nile, Japanese encephalitis, and tick-borne encephalitis viruses[1]. Until recent outbreaks in Micronesia, French Polynesia, and South and Central America[2], ZIKV was a relatively obscure pathogen and was largely neglected due to the low numbers of infections in humans and fairly benign nature of infection. Symptoms of ZIKV infection, historically, range from no signs or symptoms to influenza-like symptoms which mimic that of dengue and chikungunya infections, including a characteristic rash[1]. More severe neurological symptoms have been reported, including Guillain-Barre syndrome[3] and meningoencephalitis[4]. In 2015, an epidemic of ZIKV infection and a concurrent drastic rise in pregnancy-associated microcephaly in Brazil were deemed to be causally linked. Evidence suggested that ZIKV infection in pregnant women caused congenital abnormalities, central nervous system abnormalities, fetal growth restriction, and fetal demise, despite mild symptoms for the mother[5-7].

Development of animals models of ZIKV infection during pregnancy enabled research into the causal relationship between maternal ZIKV infection and fetal pathology and routes of viral transmission[8-10]. One important role of the placenta is to provide an immunological barrier between mother and fetus and research suggested that a potential route of ZIKV infection was trans-placental vertical transmission (from mother to fetus)[8] for which two mouse models of ZIKV infection during pregnancy were established by the Diamond and Mysorekar labs[9]. Each model required disrupting the normal immune response. The first achieved this via transgenic female mice (Ifnar1$_{-/-}$) bred with wild type male mice to produce heterozygous offspring (Ifnar1$_{+/-}$) that have a mostly intact immune response. The second model utilized wild type females bred with wild type males, and the pregnant females received an injection of an anti-ifnar antibody (anti-Ifnar1 mAb) one day before exposure to ZIKV to make the dams transiently immunocompromised. Both models resulted in significant levels of ZIKV in the placentas and fetal heads at embryonic day 13.5 (E13.5), but the transgenic model also resulted in significant numbers of spontaneous fetal abortions and resorptions at E13.5[9].

Using these established mouse models of ZIKV infection, potential interventions to attenuate or prevent vertical transmission of ZIKV were investigated[11-13]. Inhibition of autophagy in human trophoblasts was shown to reduce ZIKV replication and in pregnant mice, similarly, inhibition of autophagy resulted in reduced placental viral titers[11]. Hydroxychloroquine (HCQ) is an FDA approved antimalarial drug regularly administered to pregnant women with chronic autoimmune disorders[14] and is a known autophagy inhibitor[15, 16]. The Mysorekar lab reported that when ZIKV infected pregnant dams were treated with HCQ, fetal sizes were increased, placental and fetal viral titer numbers were reduced, and ZIKV-induced damage to placental tissue was prevented at E14.5[11]. These results were quite promising; however, a typical gestational period for the chosen breed of mouse is 19 days[17] so further investigations focusing later in gestation were needed. Additionally, utilizing non-invasive imaging techniques in conjunction with post mortem tissue analysis would enable investigations into how ZIKV infection and HCQ treatment affect placental development and function during late gestation. Towards this goal, the “gentler” transiently immunocompromised model using anti-ifnar antibody injection was used to increase the likelihood of fetuses going to near term following ZIKV infection.

Magnetic resonance imaging (MRI) techniques are non-invasive and can probe the entirety of the body, providing sub-millimeter spatial resolution, such that placental development across late gestation can be monitored. The longitudinal relaxation rate constant ($R_1$) has been shown to be directly proportional to dissolved oxygen content within tissue[18] and the effective transverse relaxation rate constant ($R_2$*) has been shown to be proportional to the concentration of deoxyhemoglobin within the vasculature[19, 20]. By measuring these rate constants at baseline conditions, during which the mother is breathing air (20% $O_2$), and during a gas challenge, during which the mother is breathing carbogen (95% $O_2$/5% $CO_2$), the level of placental function and response to environmental changes can be inferred. Carbogen, with its increased $CO_2$ content, is believed to counteract the vasoconstrictive effect of increased $O_2$[21].

A discoid, hemochorial shape is common to both human and murine placentas; each displaying three main layers[22], as shown in figure 5.1. The layer most proximal to the fetus is known as the labyrinth zone in mice and as the ‘fetal placenta’ in humans. This layer contains both fetal and maternal blood supply and allows for physiologic exchange between the two[22]. The middle layer is referred to as the junctional zone in mice and the basal plate in humans. This region is characterized by maternal blood only, which flows into and out of the fetal placenta or labyrinth zone in humans and mice, respectively. The layer furthest from the fetus differs slightly in humans and mice. In murine placentas, trophoblast invasion extends throughout the decidua basalis, whereas in humans this invasion continues into the underlying myometrium. Therefore, the third layer of the placenta in mice is considered to be the decidua basalis and in humans the outermost region is referred to as the placental bed, encompassing both the decidua basalis and the myometrium[22]. For the purposes of this study, we focused our attention on the murine layers that are functionally analogous with the human anatomy and therefore strived to only segment the labyrinth and junctional zones in our MR images.

As mice have a typical litter size of about 8 fetoplacental units, a difficulty arises in linking fetoplacental units within a dam across gestation. MRI methods such as bidirectional arterial spin labeling can be used to non-invasively identify the order of fetoplacental units within a dam[23]. However, this technique is challenging and requires significant scan time. As the MRI protocol already included approximately one hour of scan time per animal per gestational age (GA), we decided to forgo such measures knowing that unique identification across gestation would not be possible. Furthermore, due to the design and vasculature of the murine uterus, each fetoplacental unit is exposed to a slightly different amount of blood flow and delivery of nutrients, respiratory gases, etc. which, are subject to change with gestation[24]. Thus small differences are expected across fetoplacental units within a litter. To counteract this, MRI results are reported as the average value per dam.

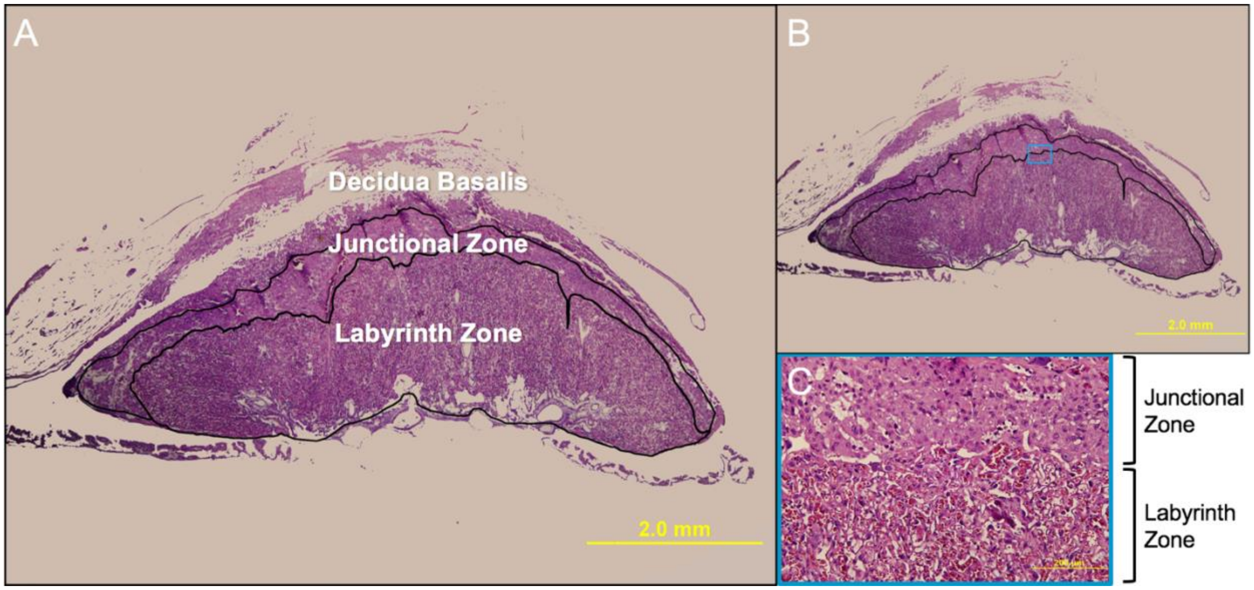

**Figure 5.1. A)** H&E stained histological image of murine placenta with each layer annotated and the junctional and labyrinth zones outlined in black. **B)** Same image without the labels, with a blue box which indicates the field of view shown in **C)** magnified 10x. **C)** Zoomed-in region showing: junctional and labyrinth zones.

The goals of this collaboration with the Mysorekar lab were twofold: investigate the effects of 1) ZIKV infection and 2) HCQ treatment during late gestation using established mouse models, non-invasive MRI techniques, and standard biological techniques. Unfortunately, the standard biological tests on post mortem tissue did not confirm previously published results and arrived too late to rescue the study.

## 5.2 Methods

All animal experiments were approved by the Washington University Institutional Animal Care and Use Committee and were completed in collaboration with the Mysorekar lab. All studies were conducted under biosafety level II containment. A pictorial representation of the protocol is seen in figure 5.2. With the exception of animal handling for the purposes of MRI, all pre- and post-mortem animal handling was performed by members of the Mysorekar lab. Pregnant, wild-type mice lacking an intact interferon response due to an injection of 2 mg anti-ifnar-blocking antibody (anti-Ifnar1 mAb) on E8.5 were infected subcutaneously in the footpad with $10_3$ focus-forming units (FFU) of ZIKV (n=17) or phosphate buffered saline (PBS) (n=13) at E9.5. Six animals from each cohort were treated with 40 mg/kg of HCQ while the remainder received placebo PBS intraperitoneally daily from E10.5 to E17.5.

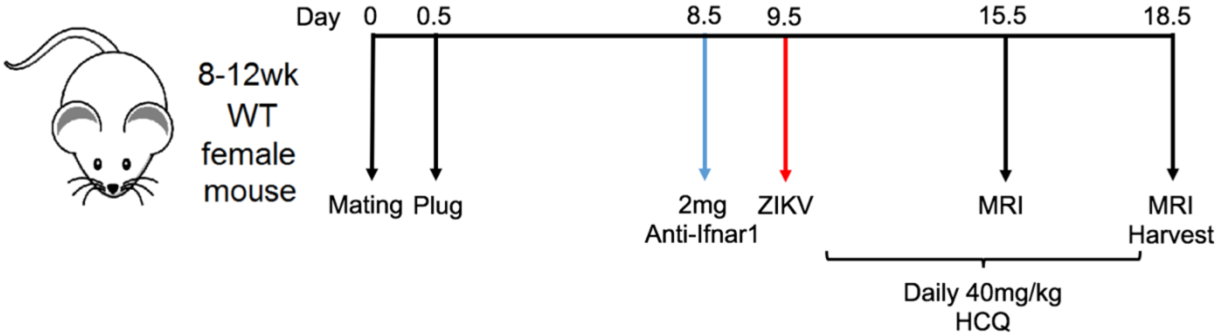

**Figure 5.2**. Schematic depiction of experimental design of infection, treatment, and imaging protocols for pregnant mice. All animals received an injection of anti-ifnar-blocking antibody at E8.5 to transiently disrupt the interferon response. At E9.5, all animals received either ZIKV or sham injection. Half of each group then received HCQ treatment daily from E10.5 to E17.5. All animals were imaged at E15.5 and E18.5 and animals were sacrificed and maternal and fetoplacental tissues harvested immediately following sacrifice.

To measure placental volume and function, MRI experiments were performed in a 4.7-T small-animal MRI system (Agilent Technologies, Santa Clara, CA, USA) using a 5 cm ID quadrature transmit/receive coil with a 9 cm resonator length (RAPID Biomedical GmbH, Rimpar, Germany) at gestational days E15.5 and E18.5. During the MRI scan, mice were anesthetized with isoflurane (3% for induction, 1-2% for maintenance) in oxygen (1 L/min), delivered through a nose cone. Once anesthetized, animals were placed in the supine position in a custom cradle and taped across the abdomen to restrict respiratory motion. Respiration rate and body temperature were monitored using an MR-compatible monitoring and gating system (SA Instruments, Inc., Stony Brook, NY, USA). Body temperature was maintained at 37°C via circulation of warm air and the respiration rate was maintained at ~50 breaths per minute through modulation of anesthesia.

The volume of all placentas (5-10/mouse) were calculated by manual segmentation of respiratory-gated, $T_2$-weighted, multi-slice fast-spin-echo (FSEMS) images. Figure 5.3 shows a representative example of a manually segmented placenta. The combined junctional and labyrinth zones were segmented by hand, and then this region was automatically divided into the two layers based on the relative intensities of each voxel using Otsu's method[25].

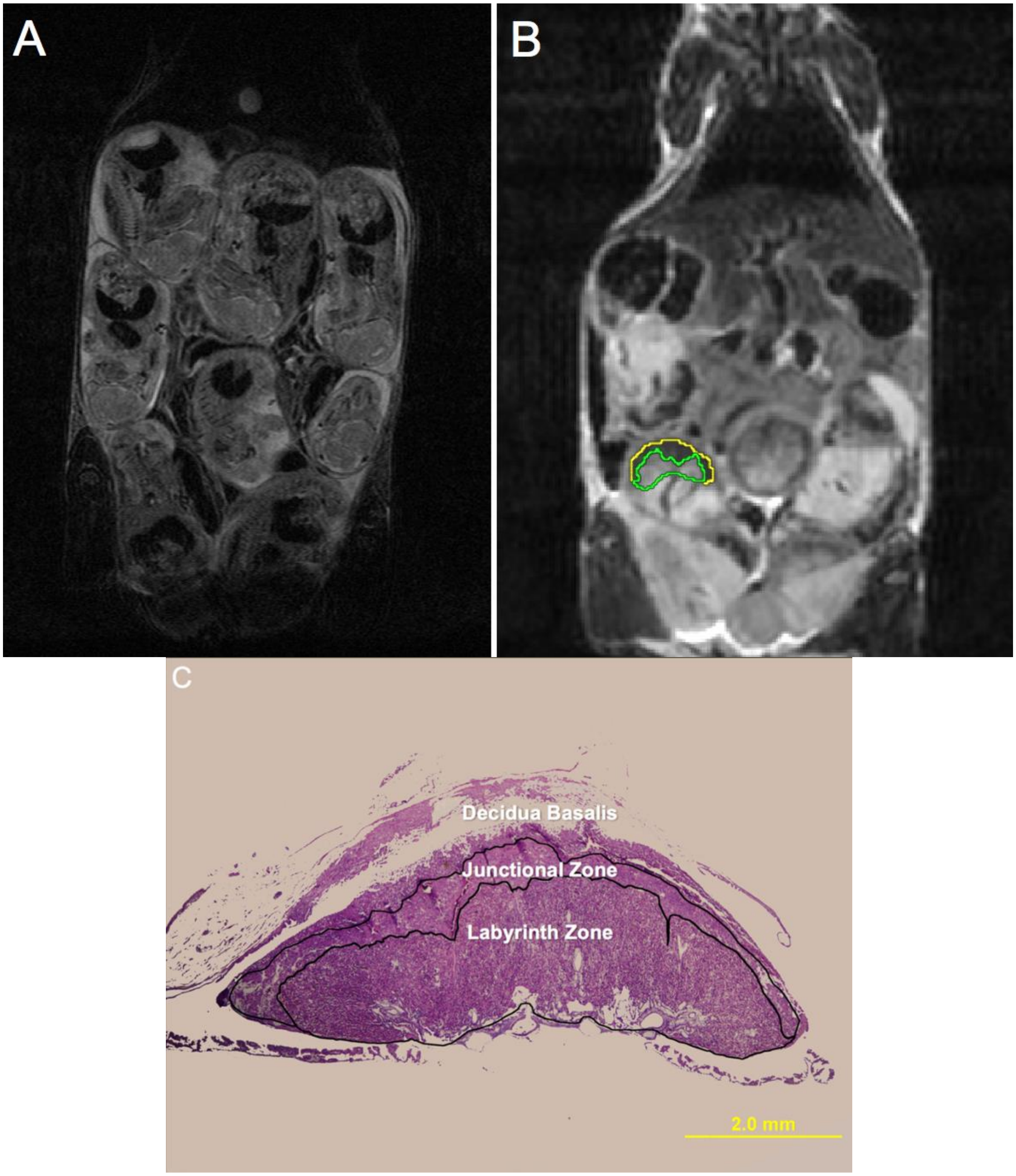

**Figure 5.3.** Representative murine abdominal MR images at 4.7T and H&E stained placenta. **A)** high resolution $T_2$-weighted FSEMS anatomic MR image (125 um x 125 um in plane resolution) at E18.5 and a **B)** $T_2$-weighted FSEMS anatomic MR image (250 um x 250 um in plane resolution) at E15.5 of a single slice within the abdomen of a different pregnant dam than in **A)**. A single placenta is outlined, with green outlining the labyrinth zone and yellow the junctional zone. **C)** H&E stained histological image of murine

placenta with each of the three layers annotated and the junctional and labyrinth zones outlined in black.

The FSEMS parameters were: time to repetition (TR) = 2000 ms; initial echo time (TE) = 12 ms; 4 refocused echoes; effective TE = 48 ms; field of view, 4.8 x 6.4 $cm^2$; matrix, 96 x 256, zero filled to 192 x 256 such that in-plane resolution was 0.25 mm; 0.5 mm slice thickness; 3 averages; scan time ~ 15 minutes. A series of 3D gradient-echo (3DGE) variable flip angle (VFA) images with TR/TE = 50 ms/1.74 ms, utilizing five flip angles (5, 10, 15, 30, and 50 degrees) was acquired for $R_1$ mapping[26]. The flip angles were optimized for characterizing the following signal intensity model[26]

$$SI_{VFA}(\theta) = \frac{\mathrm{M}_0 \sin(\theta)\,(1 - e^{-R_1 * TR})}{1 - \cos(\theta)\, e^{-R_1 * TR}}$$

in which $SI_{VFA}$ is the VFA signal as a function of flip angle, $\theta$, and $M_0$ incorporates the proton density. Using $R_1$ values from preliminary experiments and normalizing $M_0$ to one, the expected range of $SI_{VFA}$ curves is shown in Figure 5.4 A. Five flip angles were then chosen to accurately characterize the $SI_{VFA}$ curve and stratify curves for differing $R_1$ values within the expected range. The chosen flip angles overlaid upon the $SI_{VFA}$ curve for $R_1$ = 0.5 $s^{-1}$ are shown in Figure 5.4 B. The flip angle that is most sensitive to $R_1$ differences over the expected range was determined by calculating the derivative of the difference between the $SI_{VFA}$ curves for $R_1$ = 0.6 $s^{-1}$ and $R_1$ = 0.4 $s^{-1}$ and solving for $\theta$, which was approximately 0.4 radians or 22°. This calculated flip angle represents the optimum value for this expected $R_1$ range for a single flip angle. As we were using five flip angles, we selected a range of flip angles about the optimum flip angle. Furthermore, in Figure 5.5 we show that the $SI_{VFA}$ curves for the 15° and 30° flip angles have similar slopes, and therefore similar sensitivities, as that of the optimum flip angle over the expected range of $R_1$ values.

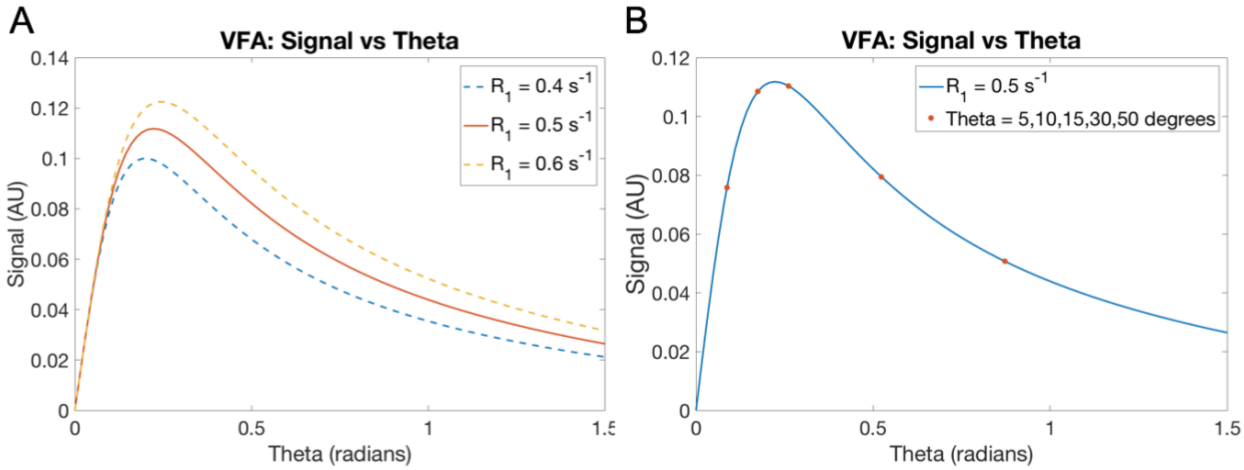

**Figure 5.4. A)** $SI_{VFA}$ curves as a function of θ (in radians) for the expected range of $R_1$ values: $R_1 = 0.4\ s_{-1}$ [dashed blue]; $R_1 = 0.5\ s_{-1}$ [solid orange]; and $R_1 = 0.6\ s_{-1}$ [dashed yellow]. **B)** The $SI_{VFA}$ curve for the expected $R_1 = 0.5\ s_{-1}$ [solid blue line] overlaid with the chosen flip angles [orange stars].

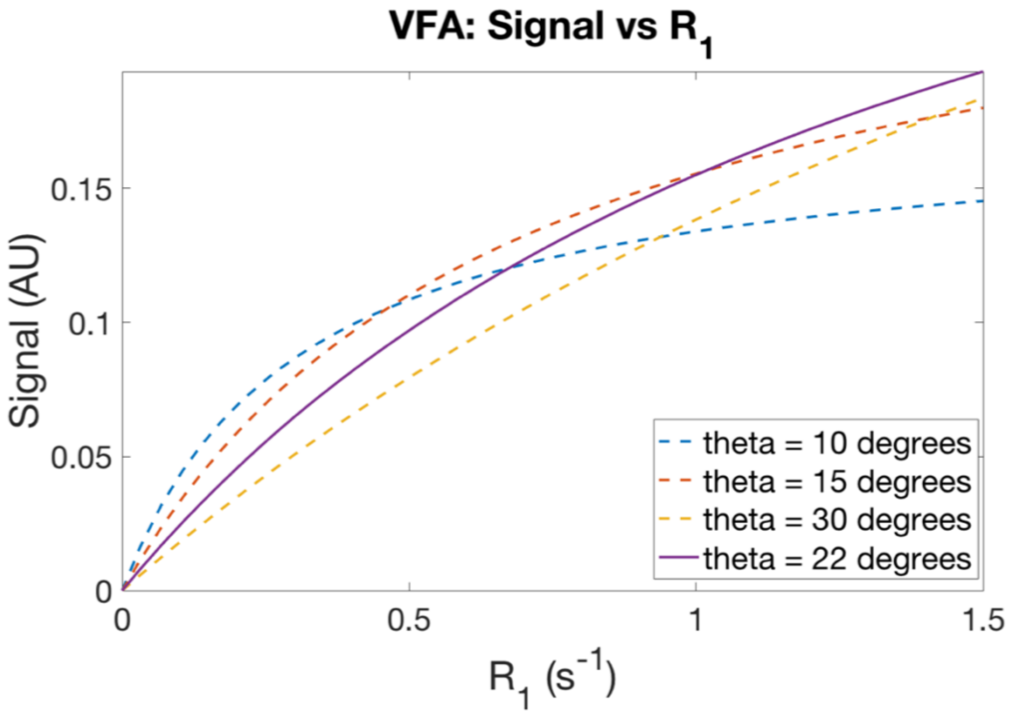

**Figure 5.5.** $SI_{VFA}$ curves as a function of $R_1$ showing the optimal flip angle (θ = 22°) [solid purple] and the middle three flip angles (θ = 10° [dashed blue], θ = 15° [dashed orange],

and $\theta = 30^\circ$ [dashed yellow]) from the chosen range of 5 flip angles for the range of $R_1$ = 0.4 $s^{-1}$ to 0.6 $s^{-1}$.

A 3D multi-echo, gradient-echo (3DMGE) image with TR = 50 ms, flip angle = 15 degrees, and six echoes starting at 1.74 ms with echo spacing of 4 ms was acquired for $R_2$* mapping. The echo times used were optimized for the following signal model:

$$SI_{TE}(t) = SI_0 e^{-t*R_2^*}$$

where $SI_{TE}$ is the signal intensity as a function of time, t, and $SI_0$ is the baseline signal intensity. Using $R_2$* values from preliminary experiments and normalizing $SI_0$ to one, the expected range of $SI_{TE}$ curves as a function of time are shown in figure 5.6 A. The echo time that is most sensitive to $R_2$* differences over the expected range was determined by calculating the derivative of the difference between the $SI_{TE}$ curves when $R_2$* = 130 $s^{-1}$ and $R_2$* = 70 $s^{-1}$ and solving for t to find the optimum TE, which was approximately 10.3 ms. The minimum TE of 1.7 ms was dictated by the scanner hardware and the echo spacing was chosen to be 4 ms such that the final array of 6 echoes was distributed about the optimum TE, as shown in figure 5.6 B.

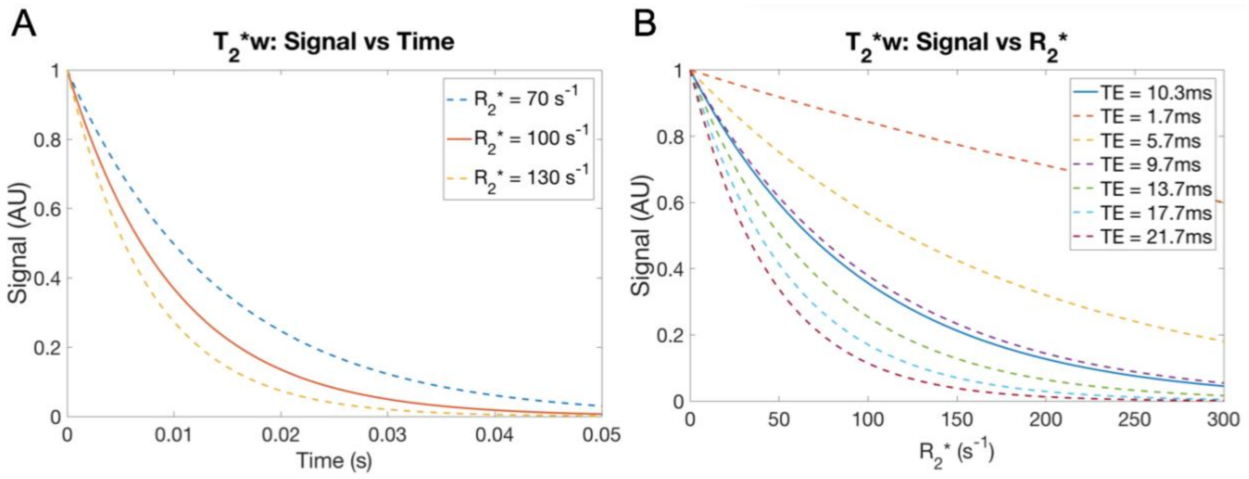

**Figure 5.6. A)** $SI_{TE}$ curves as a function of t in seconds for the expected range of $R_2$* values: $R_2$* = 70 $s^{-1}$ [dashed blue]; $R_2$* = 100 $s^{-1}$ [solid orange]; and $R_2$* = 130 $s^{-1}$ [dashed yellow]. **B)** The $SI_{TE}$ curves as a function of $R_2$* for the optimum TE = 10.3 ms [solid blue line] and the array of chosen TEs for the acquisition [dashed lines].

Both $R_1$ and $R_2$* mapping images were acquired while the mice were freely breathing medical air (20% $O_2$) followed by carbogen (95% $O_2$/5% $CO_2$) to modulate tissue and vasculature oxygenation. Both the 3DGE and 3DMGE sequences were acquired with a field of view of 4.8 x 6.4 x 1.8 $cm^3$; matrix 96 x 128 x 48 such that the resolution was 0.5 mm, isotropic; 1 average; scan time 3 minutes and 50 seconds, each. Optimal relaxation rate constants were determined for each voxel *via* Bayesian probability theory based software[27]. Following imaging on E18.5, members of the Mysorekar lab collected the animals for tissue harvesting and biological tests. The mice were euthanized, a subset of fetal sizes were measured, a subset of placentas were weighed, and the remaining placental and fetal tissues were harvested for ZIKV titering and histopathological analysis.

The Mysorekar lab also prepared additional animals which received the same infection and treatment protocol but were sacrificed at E15.5 (n=20) without undergoing any imaging. Following euthanasia, a subset of these fetal sizes were also measured and placental and fetal tissues were harvested for ZIKV titering and histopathological analysis.

Segmentation of MR images was performed on the FSEMS anatomic images and the regions of interest (ROIs) were then transferred onto the $R_1$ and $R_2$* maps using VOXA (VOXel based image Analysis toolset), a suite of custom image processing tools implemented in MATLAB[28] and co-developed by Pfizer, Inc. and the Mallinckrodt Institute of Radiology. The statistical significance of reported results was assessed via ANOVA and two sample t-tests using Origin[29] and the free and open source Jamovi Project software[30].

Herein, quantitative results are reported in the form of box and whisker plots to visualize the summary statistics, overlaid with the individual data points. The mean of each distribution is represented by an open square and the median is represented by the midline of the box. The top and bottom edges of the box represent the 75th and 25th percentiles, respectively, and the range which they cover is referred to as the interquartile range. The top and bottom whiskers represent the 95th and 5th percentiles, respectively and the dashes above the edge of the 95th percentile whisker and below the 5th percentile whisker denote the maximum and minimum values, respectively.

# 5.3 Results

## 5.3.1 MRI Results

### MRI-derived Placental Volume

The average MRI-derived placental volumes for each dam, shown in Figure 5.7, illustrate the developmental effects of both ZIKV infection and HCQ treatment. In ZIKV infected dams, the resulting placental volumes are significantly different ($p = 0.004$) by ANOVA. At E15.5, the median placental volume of the healthy control dams was 0.065 cm$^3$ whereas the median volume for ZIKV infected, untreated dams was 0.059 cm$^3$. Surprisingly, HCQ treatment had an even greater impact upon placental volume ($p < 0.001$) by ANOVA with uninfected, HCQ treated dams having a median placental volume of 0.056 cm$^3$ at E15.5. ZIKV infected, HCQ dams showed the smallest overall median placental volume which was 0.048 cm$^3$ at E15.5. Healthy control dams show a modest increase in placental volume with increased GA, with a median placental volume of 0.066 cm$^3$ at E18.5. ZIKV infected, untreated dams show no change in median placental volume and uninfected, HCQ treated dams show a modest decrease with increased GA, with a median placental volume of 0.054 cm$^3$ at E18.5. The ZIKV infected, HCQ treated cohort shows a large increase in placental volume with increasing GA such that the median placental volume is 0.057 cm$^3$ at E18.5.

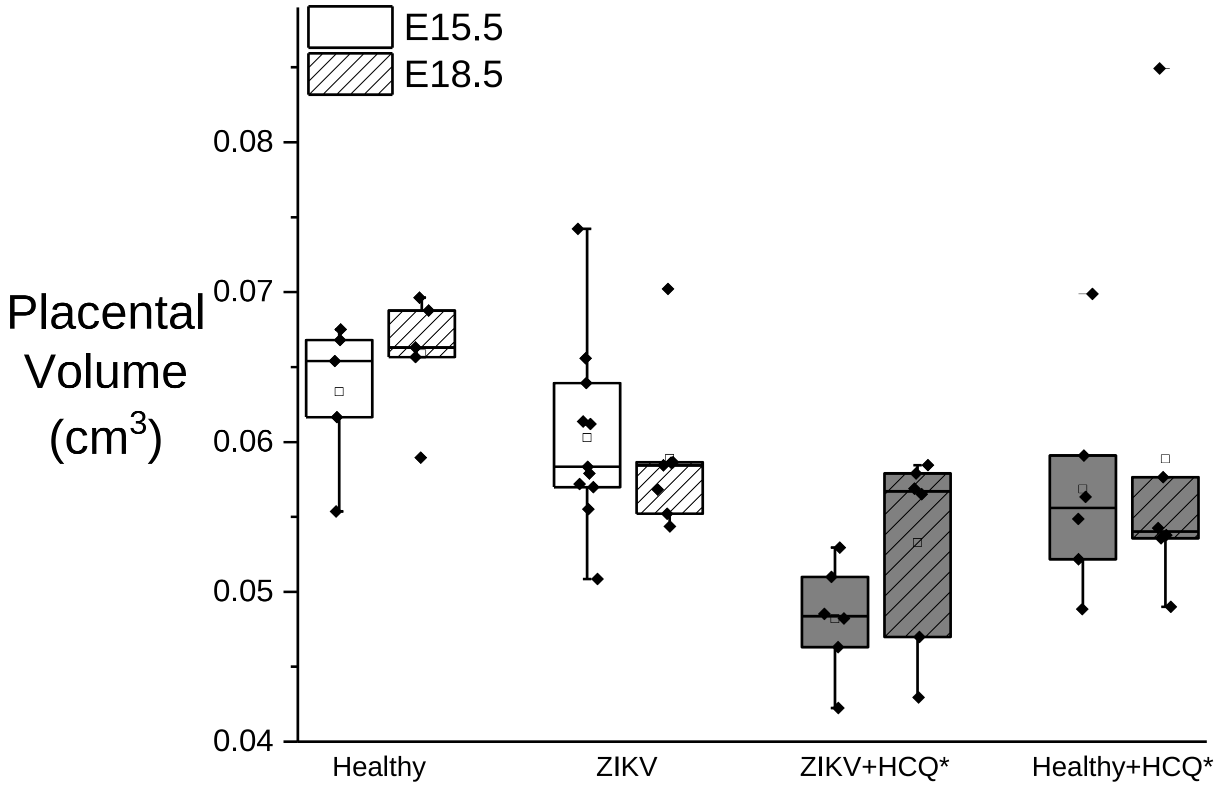

**Figure 5.7.** Average MRI-derived placental volumes per dam show reduction due to ZIKV infection and HCQ treatment. Open boxes represent GA E15.5 and diagonally lined boxes represent E18.5. White boxes represent untreated animals and gray boxes denote treated dams. Each filled point is the average placental volume of all fully segmented placentas within a single dam. Differences as a function of GA are not statistically significant, whereas ZIKV infection ($p = 0.004$) and HCQ treatment ($p < 0.001$) result in significantly smaller placental volumes by ANOVA.

### Placental $R_1$

Average placental $R_1$ per dam, shown in figure 5.8A, in insensitive to maternal gas challenge, with no statistically significant difference due to the gas challenge, presence of ZIKV infection, HCQ treatment, or with aging. Median average placental $R_1$ values for each cohort while breathing air and carbogen at both E15.5 and E18.5 are shown in Table 5.1.

**Table 5.1**

| **Placental $R_1$ ($s_{-1}$)** | | Healthy | ZIKV | ZIKV+HCQ* | Healthy+HCQ* |
|---|---|---|---|---|---|
| E15.5 | Air | 0.55 | 0.53 | 0.51 | 0.52 |
| | Carbogen | 0.58 | 0.54 | 0.52 | 0.52 |
| E18.5 | Air | 0.55 | 0.54 | 0.55 | 0.51 |
| | Carbogen | 0.53 | 0.51 | 0.55 | 0.53 |

The average change in placental $R_1$ upon switching from breathing air to carbogen, as shown in figure 5.8B, is nearly zero for all cohorts and there is no statistically significant difference due to the presence of ZIKV infection, HCQ treatment, or the GA of the fetoplacental units by ANOVA. All median changes in $R_1$ with gas challenge are less than 0.01 $s_{-1}$ with the exception of ZIKV infected, untreated dams only at E18.5 when the median change is 0.014 $s_{-1}$. Figure 5.8C shows a color map of $R_1$ values for each voxel within all placentas contained within a single slice from a representative dam.

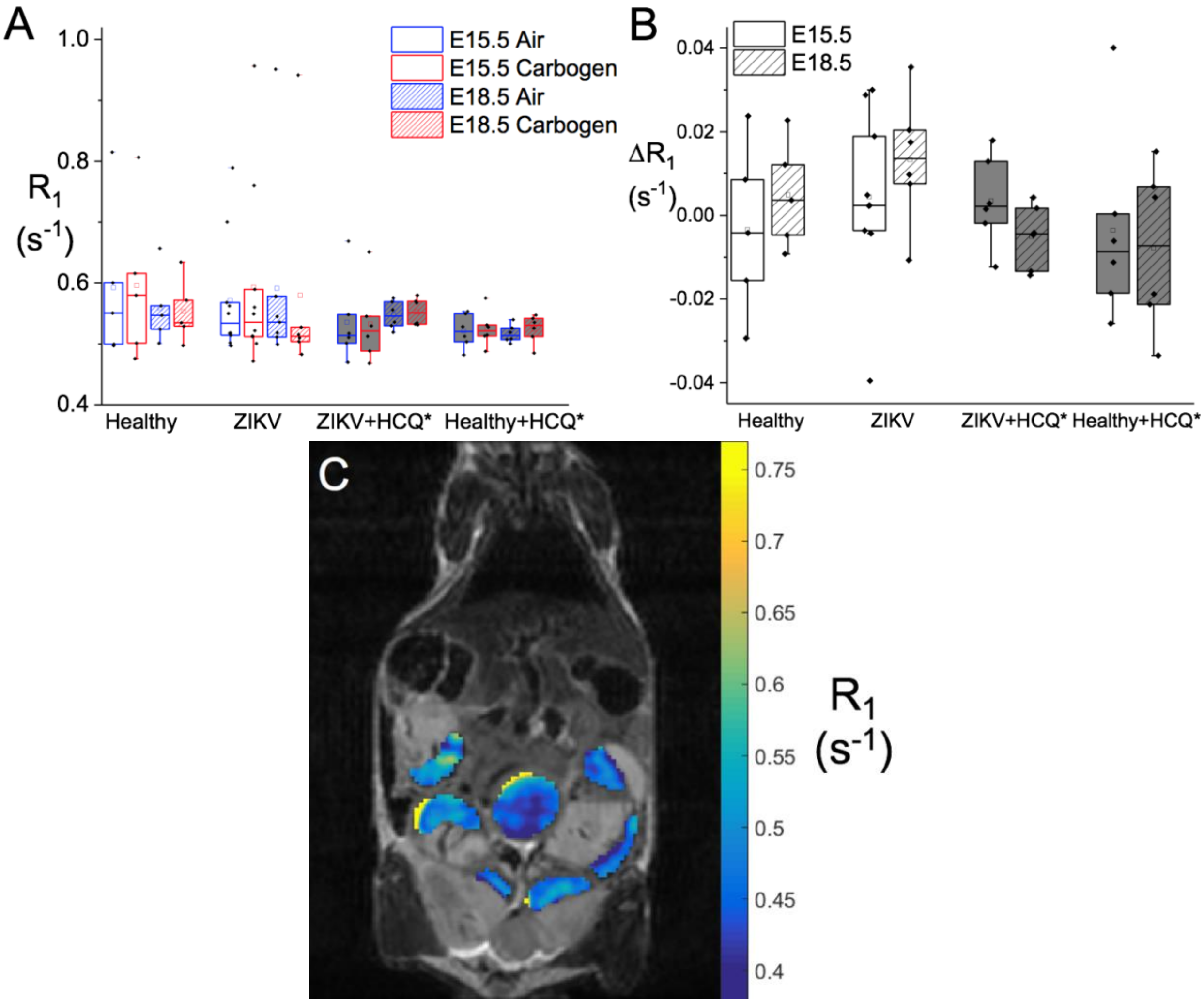

**Figure 5.8.** Placental $R_1$ show little response to gas challenge and no change with ZIKV infection, HCQ treatment, or aging. **A)** Average placental $R_1$ per dam for each cohort, at both GAs, and on both air and carbogen breathing gas conditions. There is no significant change in placental $R_1$ due to the presence of infection or treatment nor as a function of GA or the breathing gas challenge by ANOVA **B)** Average change in $R_1$ due to the gas challenge ($R_1$[air] – $R_1$[carbogen]) at both GAs. There is no significantly different change in $R_1$ in response to the gas challenge due to the presence of ZIKV infection, presence of HCQ treatment, or the GA of the fetoplacental units. Each point in **A)** and **B)** is the average $R_1$ value of all placentas within a single dam, excluding any fetoplacental units that showed signs of undergoing spontaneous abortion and resorption. **C)** Representative color map depicting the range of $R_1$ values on a voxel wise basis seen within and across placentas in a single imaging slice for a single dam. Inlaid color bar shows corresponding $R_1$ values.

### Placental $R_2$*

Average placental $R_2$* per dam, shown in figure 5.9A, is sensitive to GA ($p < 0.001$) and the gas challenge ($p < 0.001$), but there is no statistical significance of ZIKV infection or HCQ treatment by ANOVA. All cohorts show an increase in $R_2$* on air with increased GA and a decrease in $R_2$* when breathing carbogen at both GAs. Median average placental $R_2$* values for each cohort while breathing air and carbogen at both E15.5 and E18.5 are shown in Table 5.2.

**Table 5.2**

| **Placental $R_2$* ($s^{-1}$)** | | Healthy | ZIKV | ZIKV+HCQ* | Healthy+HCQ* |
|---|---|---|---|---|---|
| E15.5 | Air | 96 | 95 | 82 | 91 |
| | Carbogen | 64 | 67 | 63 | 80 |
| E18.5 | Air | 118 | 108 | 112 | 115 |
| | Carbogen | 99 | 90 | 99 | 87 |

The average change in placental $R_2$* upon switching from breathing air to breathing carbogen, shown in figure 5.9B, is statistically different at different GA ($p < 0.001$) and with HCQ treatment ($p < 0.001$), but not due to ZIKV infection by ANOVA. The median change in average placental $R_2$* for the healthy control dams was 25.0 $s^{-1}$ and 15.6 $s^{-1}$ at E15.5 and E18.5, respectively. ZIKV infected, untreated dams showed a median change in average placental $R_2$* of 18.9 $s^{-1}$ and 17.8 $s^{-1}$ at E15.5 and E18.5, respectively. For ZIKV infected, HCQ treated dams, the median change in $R_2$* was 10.7 $s^{-1}$ and 13.0 $s^{-1}$ at E15.5 and E18.5, respectively. And finally, uninfected, HCQ treated dams showed a median change in average placental $R_2$* of 8.8 $s^{-1}$ and 28.5 $s^{-1}$ at E15.5 and E18.5, respectively. Figure 5.9C shows a color map of $R_2$* values for each voxel within all placentas contained within a single slice from a representative dam.

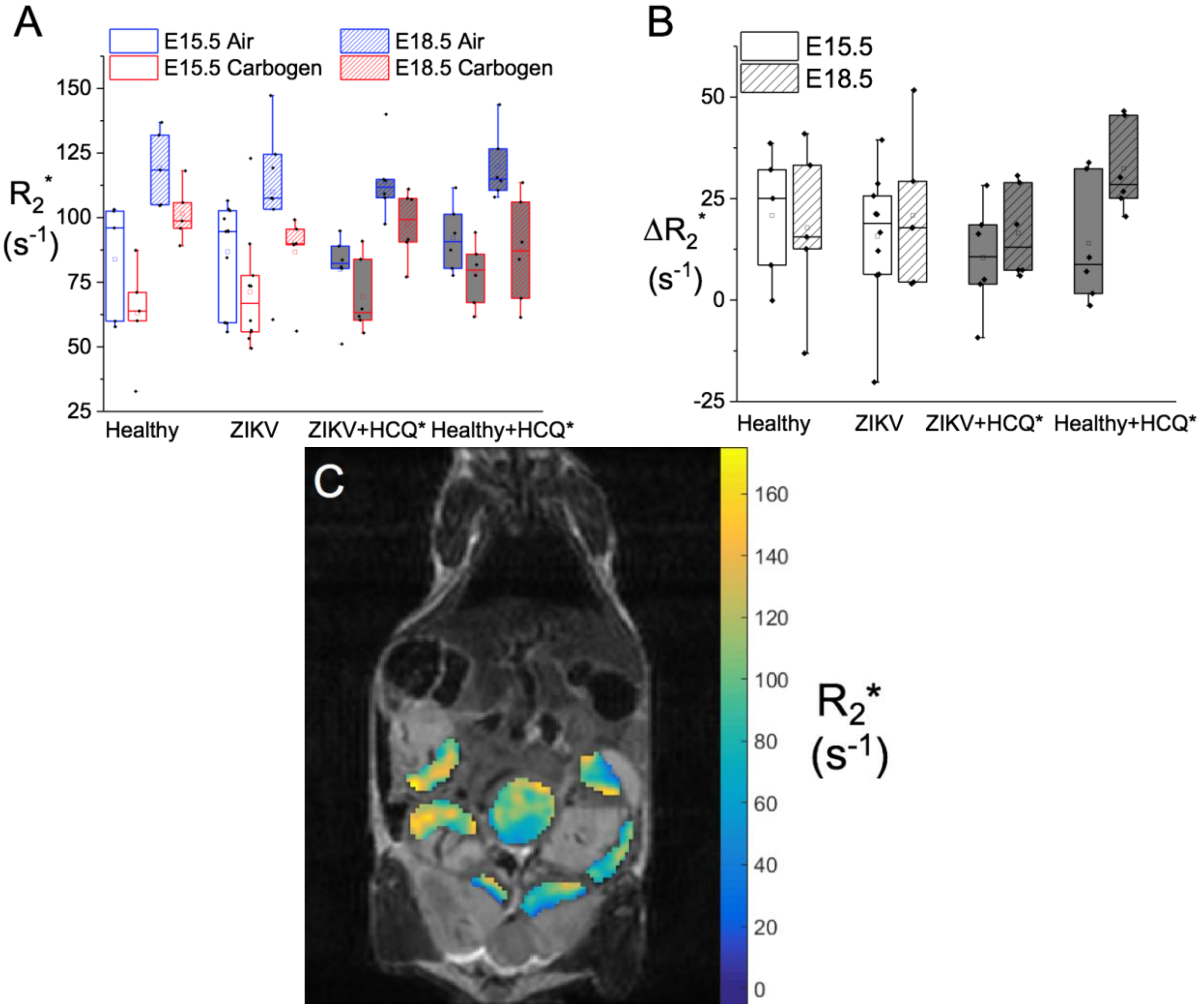

**Figure 5.9.** Placental $R_2$* responds to gas challenge differently due to HCQ treatment, but not ZIKV infection. **A)** Average placental $R_2$* per dam for each cohort, at both GAs, and under both air and carbogen breathing gas conditions. ZIKV infection and/or HCQ treatment do not induce a significant difference by ANOVA, whereas the increase with aging and the decrease with the breathing gas challenge were both significantly different by ANOVA, ($p < 0.001$, for both). **B)** Average change in $R_2$* due to the gas challenge ($R_2$*[air] – $R_2$*[carbogen]) at both GAs. There is no significant difference in the change in $R_2$* due to the breathing gas challenge due to the presence of ZIKV infection. However, changes resulting from HCQ treatment and as a function of GA are both statistically

significant ($p < 0.001$). Each point in **A)** and **B)** is the average $R_2$* value of all placentas within a single dam, excluding any fetoplacental units that showed signs of undergoing spontaneous abortion and resorption. **C)** Representative color map depicting the range of $R_2$* values on a voxel wise basis seen within and across placentas in a single imaging slice for a single dam. Inlaid color bar shows corresponding $R_2$* values.

## 5.3.2 Biological Results via Mysorekar Lab

### Placental Weights

Placental weights at E18.5, shown in Figure 5.10, were not significantly different due to ZIKV infection or HCQ treatment by ANOVA. The median placental weight at E18.5 for healthy control dams was 0.091 g. The median placental weight from ZIKV infected dams at E18.5 was 0.095 g. Both ZIKV infected and uninfected dams that received HCQ treatment had median placental weights of 0.096 g at E18.5.

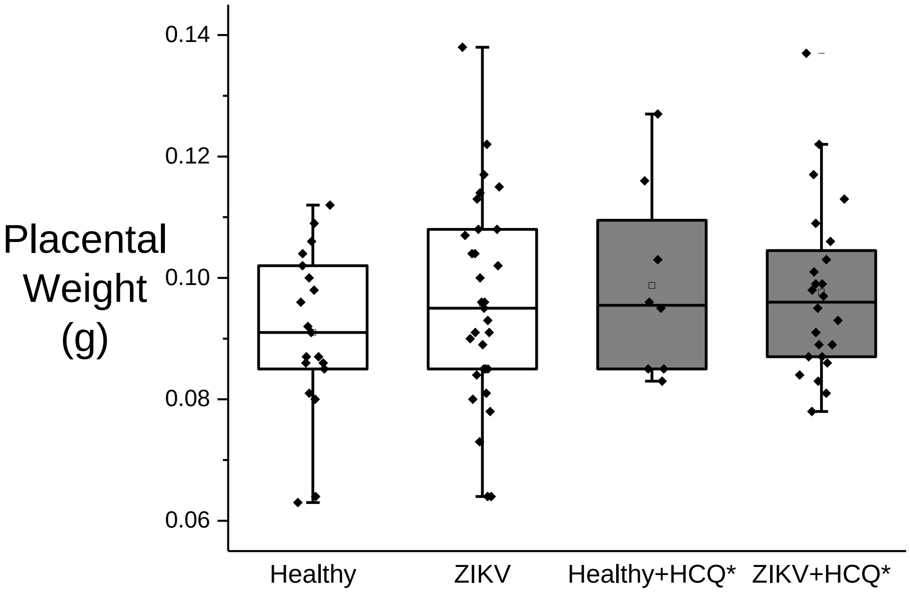

**Figure 5.10.** Individual placental weights at E18.5 for each cohort. Placental weights reported in grams. White boxes represent placentas from untreated animals and gray boxes represent placentas from HCQ treated animals. Neither ZIKV infection nor HCQ treatment resulted in significant differences in placental weights by ANOVA.

### Fetal Sizes

Figure 5.11A shows fetal sizes reported as the product of the crown to rump length (CRL) and the occipital lobe to frontal lobe diameter (OF) of the skull at both GAs. A loss of tissue samples due to contamination during storage resulted in no viable samples from the untreated healthy or ZIKV cohorts at E18.5. The only factor found to be statistically significant by ANOVA was GA ($p < 0.001$), while the presence of ZIKV infection and HCQ treatment did not result in significant differences. Figure 5.11B shows only those fetal size results from E15.5 and further ANOVA on just these results once again show no statistical significance of the presence of ZIKV infection or HCQ treatment. Healthy control fetuses were on average 89.7 mm$_2$ and ZIKV infected, untreated fetuses were on average 82.3 mm$_2$ at E15.5. Fetuses from ZIKV infected, HCQ treated dams were on average 89.3 mm$_2$ and 151.1 mm$_2$ at E15.5 and E18.5, respectively. Finally, fetuses from uninfected, HCQ treated dams were on average 88.8 mm$_2$ and 147.6 mm$_2$ at E15.5 and E18.5, respectively.

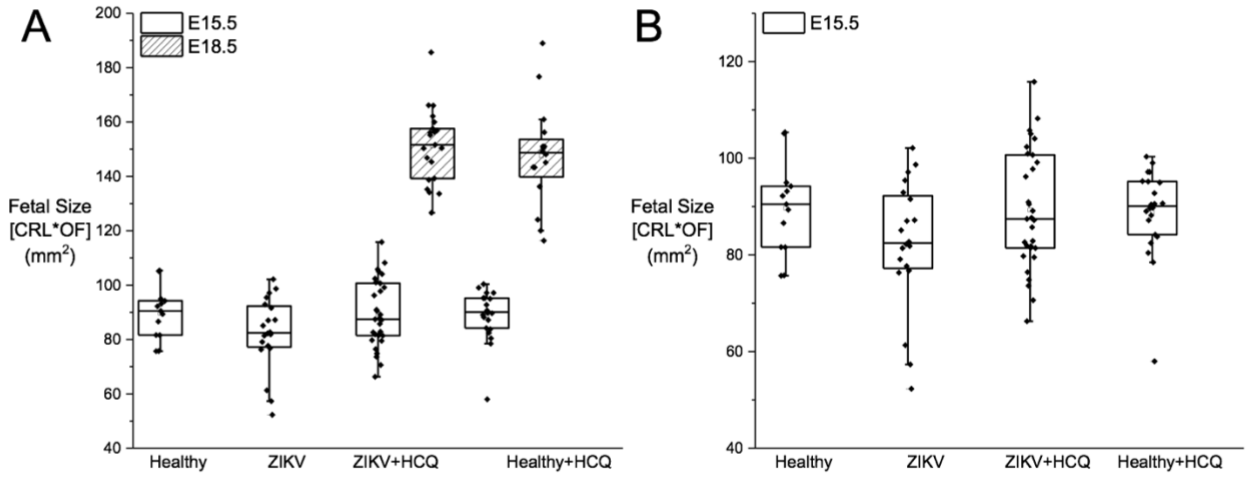

**Figure 5.11.** Fetal sizes measured as the product of the crown to rump length (CRL) and the occipital to frontal diameter (OF) of the skull. **A)** All fetal sizes measured following tissue harvest and fixation in formalin. Fetuses measured at E15.5 are from dams that were sacrificed at E15.5 and did not undergo any imaging. Fetal sizes at E18.5 were from dams that were imaged at both GAs. Loss of tissue samples due to contamination resulted in no viable samples from the untreated healthy or ZIKV cohorts at E18.5. The only statistically significant factor by ANOVA is GA; presence of infection and/or treatment do not result in statistically significant differences. **B)** The same results from E15.5 shown in **A)** without the E18.5 results, allowing for a reduced range of fetal sizes. The ZIKV infected, untreated fetal sizes appear to be trending downward, however neither the presence of infection nor treatment show statistically significant differences at E15.5.

### Fetal and Placental Viral Titers

Figure 5.12A shows viral titer results from fetal heads. Only tissue samples collected from ZIKV infected animals were used in viral titer analysis, as uninfected samples would all result in zero FFU. The mean value at E18.5 for ZIKV infected, untreated animals was 90.7 FFU equivalent per gram and ZIKV infected, HCQ treated animals was 59.4 FFU equivalent per gram. A two sample t-test found the two groups were not significantly different. Figure 5.12B shows viral titer results from placental tissue. The mean value at E18.5 for ZIKV infected, untreated animals was 1.35 x $10^7$ FFU equivalent per gram and the mean value for ZIKV infected, HCQ treated animals was 1.24 x $10^7$ FFU equivalent per gram. A two sample t-test found the two groups were not significantly different. Figure 5.12C shows the ratio of the fetal head to placental viral titer results. The mean value for the ZIKV infected, untreated animals was 1.15 x $10_{-5}$ and the mean value for the ZIKV infected, HCQ treated animals was 5.38 x $10_{-6}$. A two sample t-test found the two groups were not significantly different.

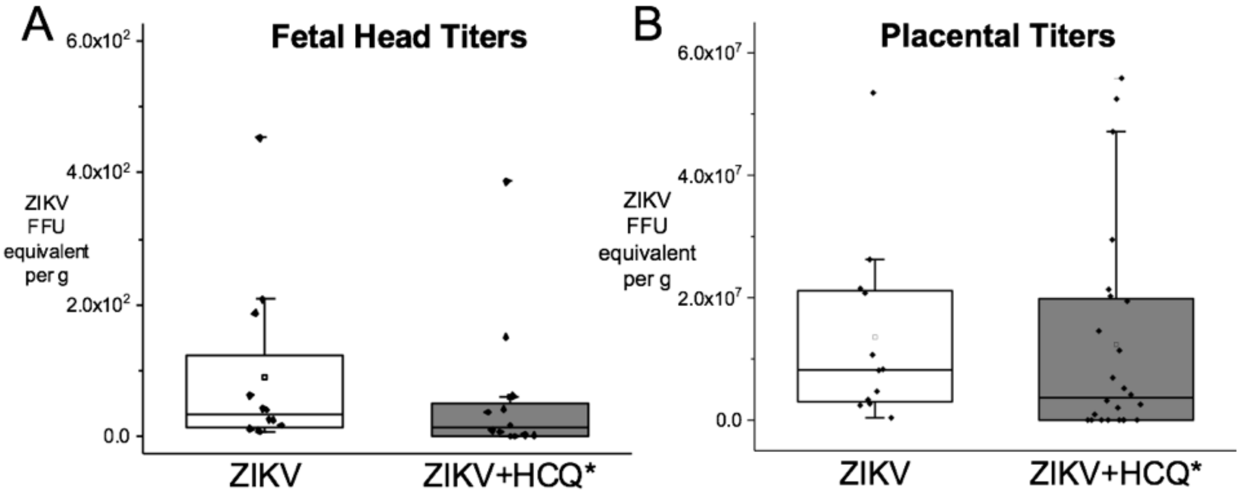

**Figure 5.12.** Fetal and Placental viral titer results show no difference with HCQ treatment. **A)** Fetal head and **B)** placental viral titer results at E18.5 from the ZIKV infected, untreated and ZIKV infected, HCQ treated cohorts. While ZIKV in some fetal heads and placentas was present at reduced levels, the inhomogeneous response to HCQ treatment results in no significant difference as determined by a two sample t-test in either the fetal head or the placental results.

# 5.4 Discussion

## 5.4.1 MRI Results

### MRI-derived Placental Volume

Decreased placental size with the presence of ZIKV infection suggest that the Zika virus interferes with proper development of murine placenta across gestation. Previous studies have shown that ZIKV invades trophoblast cells and induces apoptosis, increased nucleation of fetal erythrocytes, and abnormal fetal vasculature[9]. Surprisingly, placental volume was similarly smaller than those in healthy control dams when treated with HCQ and smaller still when both ZIKV infection and HCQ treatment were present. One potential explanation for this effect is that HCQ alters the delivery of oxygen. Chloroquine (CQ), the precursor to HCQ, has been shown in multiple cases to induce methemoglobinemia[31-33] wherein the relative amount of hemoglobin in an oxidized ferric form ($Fe^{3+}$) is increased. Methemoglobin has a very high affinity for oxygen such that virtually no oxygen is delivered to the tissue via these ferrihemoglobin carriers. Given the similarities of the two drugs, it is possible that HCQ could also induce an increase in methemoglobin concentrations and that the resulting smaller placentas are due to decreased oxygen transfer to the developing placenta. However, the effects of HCQ on the placental are not well understood, with very few studies having been conducted thus far[34]. One such study found that HCQ had no negative effects upon cell turnover, nutrient transport, or cytokine release but increased anti-inflammatory protection and promoted regeneration or syncytiotrophoblasts in human placental explants[34]. The anti-inflammatory protection may explain why the ZIKV infected, HCQ treated placentas increased significantly in size later in gestation. Whereas the ZIKV infected, untreated placentas did not show any increase in size from E15.5 to E18.5, placentas from ZIKV infected, HCQ treated dams greatly increased in size. The end result is much smaller than that of the healthy controls, but the increase in placental volume seems to suggest a positive influence of the HCQ treatment.

### Placental $R_1$

The lack of differences in $R_1$ across cohorts or with GAs suggests no major differences in the amount of dissolved oxygen within the tissue. Due to the slight paramagnetic nature of molecular oxygen ($O_2$), $R_1$ is linearly proportional to the concentration of dissolved $O_2$ in tissue. It acts, in effect, as a weak, endogenous contrast agent. The use of a gas challenge to induce higher tissue oxygenation was intended to elucidate any differential responses to altered metabolic states. However, the lack of apparent $R_1$ response to ZIKV infection, HCQ treatment, GA, or the gas challenge is not entirely surprising or indicative, as the $pO_2$ effect upon $R_1$ in tissue is known to be quite small[18, 35, 36]. Furthermore, the inhomogeneity of $R_1$ values within the placenta complicates the situation further and could be masking any response to the gas challenge or the infection and treatment protocol. It is possible that changes are occurring within the placenta to which we are not sensitive using this particular MRI protocol and that these changes are being further diluted by first averaging across all voxels within each placenta and then averaging across all placentas within each dam. While Avni, et al. showed a difference in placental $R_1$ of about 0.15 $s^{-1}$ between 100% $O_2$ and 20% $O_2$ maternal breathing gas[37], studies in human placentas show that $R_1$ response to gas challenge decreases with gestation and is nearly zero at term equivalent of E14.5[38]. Therefore, it is also possible that we do not see a response to the gas challenge because our study focused only on late gestation.

### Placental $R_2^*$

Contrast in $R_2^*$ is the basis of BOLD MRI, or fMRI, wherein changes in the magnetic susceptibility of blood due to variations in the ratio of oxyhemoglobin to deoxyhemoglobin lead to changes in $R_2^*$. Oxyhemoglobin is diamagnetic whereas deoxyhemoglobin is paramagnetic and an increase in the oxyhemoglobin to deoxyhemoglobin ratio decreases the magnetic susceptibility differences between the intravascular and extravascular spaces. This increased homogeneity in the local magnetic field results in a decrease in $R_2$*. Therefore, when the dams breathe carbogen, the increased oxygen content within the breathing gas drives an increase in the proportion of oxyhemoglobin and $R_2$* should decrease. This expected result is seen for all four cohorts at both gestational days. Furthermore, the baseline $R_2$* (or $R_2$* on air) is shown to increase for all cohorts with an increase in GA. This can be explained by the fetal demand for oxygen increasing as the fetus continues to grow and develop across gestation.

Given the differences in placental volumes, the lack of a difference in $R_2$* with ZIKV infection was unexpected and suggests that the volume difference is not due to altered vasculature. However, studies in ZIKV infected pregnant rhesus macaques have shown extensive damage to the maternal-fetal interface wherein oxygen transport from mother to fetus was significantly impeded[39]. HCQ treatment does not appear to greatly affect the baseline $R_2$*, as a slight, but not statistically significant, decrease in the median $R_2$* is seen by ANOVA. However, the change in $R_2$* due to the gas challenge is significantly affected by HCQ treatment. Delta $R_2$* is generally smaller with the presence of HCQ, which could be due to the presence of increased levels of methemoglobin reducing the amount of deoxyhemoglobin in the blood supply before the gas challenge and therefore the response to the gas challenge. The exception to this trend is that of the uninfected, HCQ treated dams at E18.5, which show increased change in $R_2$* due to the gas challenge. This result is quite puzzling and a better understanding of the effect of HCQ on healthy tissue is required to determine the cause.

### 5.4.2 Biological Results via Mysorekar Lab

#### Placental Weight & Fetal Size

As noted previously, differences in placental volume across cohorts were found via MRI methods. However, the wet weights of individual placentas were found to not be significantly different due to ZIKV infection or HCQ treatment. This suggests that the placentas of ZIKV infected and/or HCQ treated dams are denser than those of healthy control dams. ZIKV infection could potentially disrupt normal development of placental structures, resulting in a denser placenta. HCQ is used to treat inflammatory conditions such as rheumatoid arthritis and lupus as it inhibits receptors involved in inflammatory pathways[34]. Many developmental processes are a finely tuned balance between anabolic and catabolic factors and the decrease in inflammation resulting from HCQ treatment could disturb this balance, resulting in denser tissue.

HCQ is known to cross the human placenta, as studies have shown similar concentrations in maternal and umbilical cord blood samples concomitantly collected at the time of delivery[40]. However, multiple studies focusing on the safety and efficacy of HCQ treatment for autoimmune diseases, such as lupus or rheumatoid arthritis, have shown that HCQ exposure during pregnancy does not appear to increase the risk of adverse outcomes or congenital defects[14, 41-43]. A minority of published works reference instances of treatment with HCQ and other malarial drugs in the event of malaria outbreak, prescribed either prophylactically or therapeutically, and stressed cautious use of the drug in the case of pregnancy due to increased rates of stillbirths, spontaneous abortions, and congenital birth defects[44]. However, the lack of an effect upon placental weight or fetal size herein supports the argument that HCQ in pregnancy does not pose a threat to normal fetal development.

Potentially the most surprising and concerning result from this study is the lack of a difference in fetal size due to the presence of ZIKV infection. Previously published results, in part by our collaborators, using similar infection protocols resulted in significantly decreased fetal size at GA E13.5[9]. While it is possible that this difference is due to the fact that our results herein were collected at GA E15.5, that seems highly improbable. In fact, it was hypothesized that the difference between ZIKV infected and healthy control fetal sizes would be more pronounced later in gestation as the growth of the ZIKV infected fetuses would have continued to be retarded. Furthermore, using nearly the exact same infection and treatment protocol, our collaborators saw a significant increase in fetal size in ZIKV infected, HCQ treated animals in comparison to ZIKV infected, untreated animals at E14.5[11] whereas we saw no difference at E15.5. Once again, it is possible, but improbable, that this loss of differentiation between the groups is due to the increase in GA by one day. This inability to reproduce previous findings is quite concerning and raises questions regarding the viability of this study. Unfortunately, fetal size data were among the last to be collected and analyzed and were not available until after the remainder of the study was completed. Further experiments would need to be done to understand where the biology of our animals deviated from that of previously published results. Unfortunately, this is impossible as most of the tissue samples collected were lost to contamination.

### Viral Titers

No significant effect is seen in terms of viral titer results assessed within either the placenta or the fetal head. It is true that both the fetal head and placental viral titer results show downward trends with HCQ treatment, however this effect is too small to be statistically significant. Both of these results deviate from previously published results determined at E14.5[11, 15]. From the viral titer results, we observed a wide range of ZIKV infection in the placentas and fetuses within a single dam. It is possible that the HCQ treatment, which was administered via an IP injection, may not homogeneously disperse to all placentas. Perhaps a more likely explanation is that the daily injections were not all identically administered, which caused deviations in the response to HCQ treatments.

The failure to reproduce the biological measures from previous ZIKV studies diminishes the significance of the MR findings. It is certainly possible that the decision to study ZIKV infection and HCQ treatment later in gestation led to our investigating only healthier fetoplacental units, as mice are able to undergo spontaneous abortion and resorption of unhealthy fetoplacental units. However, the lack of tissue sample precludes further investigation of these differences. Finally, we did see significant differences in placental volume across gestation with ZIKV infection and HCQ treatment and $R_2$* differences with HCQ treatment via MRI which are reasonable and warrant further investigation once the biological model is further refined.

## 5.5 Acknowledgements

This project was supported in part by Mallinckrodt Institute of Radiology Pilot Fund 18-016 (WUSM), the Howard Hughes Medical Institute, and National Institutes of Health grants R01 HD086323, 5T32 EB014855, and R01 HD091218. Valuable discussions with Professors Joseph JH Ackerman and Jeffrey J Neil are gratefully acknowledged. The studies presented in this work were carried out, in part, using the Small Animal Magnetic Resonance Facility of the Washington University Mallinckrodt Institute of Radiology.

## 5.6 References

**[1]**. Lazear HM, Diamond MS. Zika Virus: New Clinical Syndromes and Its Emergence in the Western Hemisphere. *J Virol.* 2016;90(10):4864-4875.10.1128/JVI.00252-16.

**[2]**. Gatherer D, Kohl A. Zika virus: a previously slow pandemic spreads rapidly through the Americas. *J Gen Virol.* 2016;97(2):269-273.10.1099/jgv.0.000381.

**[3]**. Oehler E, Watrin L, Larre P, et al. Zika virus infection complicated by Guillain-Barre syndrome--case report, French Polynesia, December 2013. *Euro Surveill.* 2014;19(9).10.2807/1560-7917.es2014.19.9.20720.

**[4]**. Carteaux G, Maquart M, Bedet A, et al. Zika Virus Associated with Meningoencephalitis. *N Engl J Med.* 2016;374(16):1595-1596.10.1056/NEJMc1602964.

**[5]**. Brasil P, Pereira JP, Jr., Moreira ME, et al. Zika Virus Infection in Pregnant Women in Rio de Janeiro. *N Engl J Med.* 2016;375(24):2321-2334.10.1056/NEJMoa1602412.

**[6]**. Sarno M, Sacramento GA, Khouri R, et al. Zika Virus Infection and Stillbirths: A Case of Hydrops Fetalis, Hydranencephaly and Fetal Demise. *PLoS Negl Trop Dis.* 2016;10(2):e0004517.10.1371/journal.pntd.0004517.

**[7]**. Ventura CV, Maia M, Bravo-Filho V, Gois AL, Belfort R, Jr. Zika virus in Brazil and macular atrophy in a child with microcephaly. *Lancet.* 2016;387(10015):228.10.1016/S0140-6736(16)00006-4.

**[8]**. Mysorekar IU, Diamond MS. Modeling Zika Virus Infection in Pregnancy. *N Engl J Med.* 2016;375(5):481-484.10.1056/NEJMcibr1605445.

**[9]**. Miner JJ, Cao B, Govero J, et al. Zika Virus Infection during Pregnancy in Mice Causes Placental Damage and Fetal Demise. *Cell.* 2016;165(5):1081-1091.10.1016/j.cell.2016.05.008.

**[10]**. Cao B, Diamond MS, Mysorekar IU. Maternal-Fetal Transmission of Zika Virus: Routes and Signals for Infection. *J Interferon Cytokine Res.* 2017;37(7):287-294.10.1089/jir.2017.0011.

**[11]**. Cao B, Parnell LA, Diamond MS, Mysorekar IU. Inhibition of autophagy limits vertical transmission of Zika virus in pregnant mice. *J Exp Med.* 2017;214(8):2303-2313.10.1084/jem.20170957.

**[12]**. Wang S, Hong S, Deng YQ, et al. Transfer of convalescent serum to pregnant mice prevents Zika virus infection and microcephaly in offspring. *Cell Res.* 2017;27(1):158-160.10.1038/cr.2016.144.

**[13]**. Sapparapu G, Fernandez E, Kose N, et al. Neutralizing human antibodies prevent Zika virus replication and fetal disease in mice. *Nature.* 2016;540(7633):443-447.10.1038/nature20564.

**[14]**. Kaplan YC, Ozsarfati J, Nickel C, Koren G. Reproductive outcomes following hydroxychloroquine use for autoimmune diseases: a systematic review and meta-analysis. *Br J Clin Pharmacol.* 2016;81(5):835-848.10.1111/bcp.12872.

**[15]**. Cao B, Sheth MN, Mysorekar IU. To Zika and destroy: an antimalarial drug protects fetuses from Zika infection. *Future Microbiol.* 2018;13:137-139.10.2217/fmb-2017-0213.

**[16]**. Rosenfeldt MT, O'Prey J, Morton JP, et al. p53 status determines the role of autophagy in pancreatic tumour development. *Nature.* 2013;504(7479):296-300.10.1038/nature12865.

**[17]**. Murray SA, Morgan JL, Kane C, et al. Mouse gestation length is genetically determined. *PLoS One.* 2010;5(8):e12418.10.1371/journal.pone.0012418.

**[18]**. Beeman SC, Shui YB, Perez-Torres CJ, Engelbach JA, Ackerman JJ, Garbow JR. O2 -sensitive MRI distinguishes brain tumor versus radiation necrosis in murine models. *Magn Reson Med.* 2016;75(6):2442-2447.10.1002/mrm.25821.

**[19]**. Ogawa S, Lee TM, Nayak AS, Glynn P. Oxygenation-sensitive contrast in magnetic resonance image of rodent brain at high magnetic fields. *Magn Reson Med.* 1990;14(1):68-78.10.1002/mrm.1910140108.

**[20]**. Ogawa S, Lee TM, Kay AR, Tank DW. Brain magnetic resonance imaging with contrast dependent on blood oxygenation. *Proc Natl Acad Sci U S A.* 1990;87(24):9868-9872.10.1073/pnas.87.24.9868.

**[21]**. Rojas A. Radiosensitization with normobaric oxygen and carbogen. *Radiother Oncol.* 1991;20 Suppl 1:65-70.10.1016/0167-8140(91)90190-r.

**[22]**. Georgiades P, Ferguson-Smith AC, Burton GJ. Comparative developmental anatomy of the murine and human definitive placentae. *Placenta.* 2002;23(1):3-19.10.1053/plac.2001.0738.

**[23]**. Avni R, Raz T, Biton IE, Kalchenko V, Garbow JR, Neeman M. Unique in utero identification of fetuses in multifetal mouse pregnancies by placental bidirectional arterial spin labeling MRI. *Magn Reson Med.* 2012;68(2):560-570.10.1002/mrm.23246.

**[24]**. Coe BL, Kirkpatrick JR, Taylor JA, vom Saal FS. A new 'crowded uterine horn' mouse model for examining the relationship between foetal growth and adult obesity. *Basic Clin Pharmacol Toxicol.* 2008;102(2):162-167.10.1111/j.1742-7843.2007.00195.x.

**[25]**. Otsu N. Threshold Selection Method from Gray-Level Histograms. *Ieee T Syst Man Cyb.* 1979;9(1):62-66.Doi 10.1109/Tsmc.1979.4310076.

**[26]**. Fram EK, Herfkens RJ, Johnson GA, et al. Rapid calculation of T1 using variable flip angle gradient refocused imaging. *Magn Reson Imaging.* 1987;5(3):201-208.10.1016/0730-725x(87)90021-x.

**[27]**. Quirk JD, Bretthorst GL, Garbow JR, Ackerman JJH. Magnetic resonance data modeling: The Bayesian analysis toolbox. *Concept Magn Reson A.* 2018;47a(2).ARTN e21467. 10.1002/cmr.a.21467.

**[28]**. MATLAB (2015). (Version 8.5.0.197613) [Computer Software]. Natick, MA, USA: Mathworks; Retrieved from https://www.mathworks.com/

**[29]**. Origin (2017). (Version b9.4.0.220 (Academic)) [Computer Software]. Northampton, MA, USA: OriginLab Corporation; Retrieved from www.originlab.com

**[30]**. The jamovi project (2019). *jamovi* (Version 0.9) [Computer Software]. Retrieved from https://www.jamovi.org/

**[31]**. Rizvi I, Zaman S, Zaidi N, Asif MS, Abdali N. Acute life-threatening methaemoglobinaemia following ingestion of chloroquine. *BMJ Case Rep.* 2012;2012.10.1136/bcr.12.2011.5383.

**[32]**. Sankar J, Gupta A, Pathak S, Dubey NK. Death in an adolescent girl with methemoglobinemia and malaria. *J Trop Pediatr.* 2012;58(2):154-156.10.1093/tropej/fmr042.

**[33]**. Cohen RJ, Sachs JR, Wicker DJ, Conrad ME. Methemoglobinemia provoked by malarial chemoprophylaxis in Vietnam. *N Engl J Med.* 1968;279(21):1127-1131.10.1056/NEJM196811212792102.

**[34]**. Scott RE, Greenwood SL, Hayes DJL, Baker BC, Jones RL, Heazell AEP. Effects of hydroxychloroquine on the human placenta-Findings from in vitro experimental data and a systematic review. *Reproductive Toxicology.* 2019;87:50-59.10.1016/j.reprotox.2019.05.056.

**[35]**. d'Othee BJ, Rachmuth G, Munasinghe J, Lang EV. The effect of hyperoxygenation on T1 relaxation time in vitro. *Academic Radiology.* 2003;10(8):854-860.10.1016/S1076-6332(03)00004-7.

**[36]**. Berkowitz BA, McDonald C, Ito Y, Tofts PS, Latif Z, Gross J. Measuring the human retinal oxygenation response to a hyperoxic challenge using MRI: eliminating blinking artifacts and demonstrating proof of concept. *Magn Reson Med.* 2001;46(2):412-416.10.1002/mrm.1206.

**[37]**. Avni R, Golani O, Akselrod-Ballin A, et al. MR Imaging-derived Oxygen-Hemoglobin Dissociation Curves and Fetal-Placental Oxygen-Hemoglobin Affinities. *Radiology.* 2016;280(1):68-77.10.1148/radiol.2015150721.

**[38]**. Huen I, Morris DM, Wright C, et al. R1 and R2 * changes in the human placenta in response to maternal oxygen challenge. *Magn Reson Med.* 2013;70(5):1427-1433.10.1002/mrm.24581.

**[39]**. Hirsch AJ, Roberts VHJ, Grigsby PL, et al. Zika virus infection in pregnant rhesus macaques causes placental dysfunction and immunopathology. *Nat Commun.* 2018;9(1):263.10.1038/s41467-017-02499-9.

**[40]**. Costedoat-Chalumeau N, Amoura Z, Aymard G, et al. Evidence of transplacental passage of hydroxychloroquine in humans. *Arthritis Rheum.* 2002;46(4):1123-1124.10.1002/art.10150.

**[41]**. Costedoat-Chalumeau N, Amoura Z, Duhaut P, et al. Safety of hydroxychloroquine in pregnant patients with connective tissue diseases: a study of one hundred thirty-three cases compared with a control group. *Arthritis Rheum.* 2003;48(11):3207-3211.10.1002/art.11304.

**[42]**. Abarientos C, Sperber K, Shapiro DL, Aronow WS, Chao CP, Ash JY. Hydroxychloroquine in systemic lupus erythematosus and rheumatoid arthritis and its safety in pregnancy. *Expert Opin Drug Saf.* 2011;10(5):705-714.10.1517/14740338.2011.566555.

**[43]**. Parke A. Antimalarial drugs and pregnancy. *Am J Med.* 1988;85(4A):30-33.10.1016/0002-9343(88)90359-2.

**[44]**. Roubenoff R, Hoyt J, Petri M, Hochberg MC, Hellmann DB. Effects of antiinflammatory and immunosuppressive drugs on pregnancy and fertility. *Semin Arthritis Rheum.* 1988;18(2):88-110.10.1016/0049-0172(88)90002-9.

# Chapter 6: Conclusion

## 6.1 Summary

Knowledge of tissue oxygenation and oxygen transport could provide improved diagnosis and treatment planning for a multitude of pathologies. In this dissertation, we have investigated MR techniques to non-invasively quantify tissue $pO_2$. In Chapter 2, a Bayesian probability theory-based, data-driven approach to model selection resulted in the biexponential signal model providing the most probable of five signal models compared for both *in vivo* and crosslinked bovine serum albumin (xBSA) longitudinal relaxation data. However, when the data are sparse or the SNR is lower, simpler models, which utilize fewer free parameters, are favored. Furthermore, xBSA displays similar longitudinal relaxation characteristics as *in vivo* tissue, and can be used as a tissue surrogate for further investigations of endogenous modifiers of $R_1$ measurements in tissue.

In Chapter 3, xBSA was employed to explore select endogenous confounds to $R_1$ measurements – temperature, pH, and protein concentration – and to quantify the direct relationship between measured $R_{1,slow}$ and tissue $pO_2$. Variations in temperature, pH, and protein concentration exert a relatively larger effect upon $R_{1,slow}$ than the paramagnetic relaxation induced by dissolved $O_2$ and must, therefore, be considered when applying $R_{1,slow}$-based methods of $pO_2$ quantification. Additionally, significant challenges in modifying the xBSA sample $pO_2$ and apparent variations in the relationship between $R_{1,slow}$ and $pO_2$ across xBSA samples, the latter due to likely cross-sample microstructural/microenvironmental variability (i.e., variable sample preparations), limit the feasibility of using xBSA as an $R_{1,slow}$ *vs.* $pO_2$ reference material.

In this dissertation, we have also investigated MRI methods for monitoring tissue oxygenation and exchange of oxygen in the placenta. The placenta is vital in maintaining the health of both mother and fetus, with facilitation of oxygen exchange prominent among its various roles. MRI biomarkers of placental function would aid in determining the optimal timing of early delivery in cases of infection or placental insufficiency, wherein knowledge of whether sub-optimal placenta performance can support continued fetal development or not is needed.

In Chapter 4, we employed mouse models of common pregnancy pathologies, including pre-eclampsia (PE) and intrauterine growth restriction (IUGR), which are proposed to be caused by abnormalities in placental vasculature. It was shown that placental volume and $R_2^*$ measures at baseline and with a gas challenge can stratify healthy placentas from those characterized by PE or IUGR. In particular, $R_2^*$ changes due to the gas challenge in the labyrinth zone show promise as a biomarker of placental function at both near-term and term, and warrant further investigation.

In Chapter 5, in a collaboration with Indira Mysorekar's lab, we investigated Zika virus (ZIKV) infection and hydroxychloroquine (HCQ) treatment effects upon placental development and function using MRI and biological methods. Volume differences were found across gestation with ZIKV infection and HCQ treatment and $R_2^*$ differences with HCQ treatment were found that warrant further investigation. However, the biological methods failed to reproduce results from previous ZIKV studies, diminishing the significance of our MR findings.

## 6.2 Future Research

### 6.2.1 Viable Application of $R_{1,slow}$-based $pO_2$ Quantification Method

Donor tissues for transplantation are in short supply worldwide, with techniques such as tissue engineering or *in vitro* organogenesis providing potential solutions[1, 2]. Lab grown tissues or organs are not yet widely available due to a lack of tissue scaffolds that can adequately provide the appropriate oxygen supply for tissue growth. Our $R_{1,slow}$-based method for $pO_2$ quantification could provide a valuable tool for non-invasively monitoring tissue development in various media to determine the optimal method of delivery of oxygen to facilitate proper tissue growth and development.

### 6.2.2 ZIKV Infection and HCQ Treatment Effects Upon Placental Development and Function

Investigation into the differences seen in biological results of our cohort of mice from those published previously would be required to interpret our MRI results. However, unanticipated loss of tissue samples from the current study precludes such investigation. It has been shown in non-human primates that ZIKV infection causes severe placental damage and abnormal oxygen transport[3]. HCQ reduces transmission or ZIKV across the placenta early in gestation and could be a viable treatment during pregnancy[4]. Repeating this study following refinement of the biological model would enhance our understanding of the placental effects of both ZIKV infection and HCQ treatment. Furthermore, dose-response studies of HCQ treatment in cases of ZIKV infection for preventing transmission of the virus without retarding fetal development could guide future clinical studies.

### 6.2.3 $R_2$* and $\Delta R_2$* as Biomarkers of Placental Function

Further investigation into the efficacy of $R_2$* and $\Delta R_2$* as biomarkers of placental function, specifically within the region of the placenta most proximal to the fetus, are warranted. Studies of healthy human placenta have shown that changes in placental $R_2$* ($\Delta R_2$*) in response to a gas challenge decrease with gestation[5], as we observed for murine placenta. Additionally, our measurements of $\Delta R_2$* with gas challenge within the labyrinth zone stratified healthy placentas from those of PE or IUGR, at both near term and term. This could be further investigated pre-clinically, wherein more severe placental dysfunction can be induced via i) increased dosage of Poly(I:C) in the PE dams; ii) ligation or occlusion of the ovarian or uterine artery to restrict blood flow into the uterine horn; iii) maternal nutrient restriction; or iv) housing under hypoxic conditions. Furthermore, measurements of $\Delta R_2$* could be investigated clinically in mothers to determine if similar trends are seen within the fetal placenta in healthy term pregnancies and those characterized by placental dysfunction.

## 6.3 References

**[1]**. Farris AL, Rindone AN, Grayson WL. Oxygen Delivering Biomaterials for Tissue Engineering. *J Mater Chem B.* 2016;4(20):3422-3432.10.1039/C5TB02635K.

**[2]**. Griffith LG, Wu B, Cima MJ, Powers MJ, Chaignaud B, Vacanti JP. In vitro organogenesis of liver tissue. *Ann N Y Acad Sci.* 1997;831:382-397.10.1111/j.1749-6632.1997.tb52212.x.

**[3]**. Hirsch AJ, Roberts VHJ, Grigsby PL, et al. Zika virus infection in pregnant rhesus macaques causes placental dysfunction and immunopathology. *Nat Commun.* 2018;9(1):263.10.1038/s41467-017-02499-9.

**[4]**. Cao B, Parnell LA, Diamond MS, Mysorekar IU. Inhibition of autophagy limits vertical transmission of Zika virus in pregnant mice. *J Exp Med.* 2017;214(8):2303-2313.10.1084/jem.20170957.

**[5]**. Huen I, Morris DM, Wright C, et al. R1 and R2 * changes in the human placenta in response to maternal oxygen challenge. *Magn Reson Med.* 2013;70(5):1427-1433.10.1002/mrm.24581.